Microfluidic Chips for Characterization of Enzyme-catalyzed Reactions and Evaluation of Dose Responses for Drug Discovery

by

Sachin Ranappa Jambovane

A dissertation submitted to the Graduate Faculty of
Auburn University
in partial fulfillment of the
requirements for the Degree of
Doctor of Philosophy

Auburn, Alabama
August 4, 2012

Keywords: Lab-on-a-chip, Droplet Microfluidics Enzyme kinetics, Drug Dose response, Drug discovery, Concentration gradient,

Approved by

Jong Wook Hong, Chair, Associate Professor, Department of Mechanical Engineering
Jeffery W. Fergus, Professor, Department of Mechanical Engineering
Barton C. Prorok, Professor, Department of Mechanical Engineering
Evert C. Duin, Associate Professor, Department of Chemistry and Biochemistry

Abstract

In last century, the discovery of semiconductors, the invention of transistors and the creation of the integrated circuit brought a revolution in the field of computation, which marked the foundation of computers and information technology. In 21st century, miniaturization of size, integration of functions, and digitization of data is a global trend in every branch of technology. The chemical and biological laboratory technology is also witnessing booming trend towards miniaturization, integration, and digitization of laboratory experiments. The advantages of this trend include ultra-low reagent consumption, wide scope for parallelization and integration, increased reaction speed, and possibility of extreme portability. The ultimate goal of miniaturization, integration and digitization in chemical and biological laboratory technology is to automate all the reaction steps—reagent metering, concentration gradient generation, mixing, incubation and detection—with sub microliter-scale chip, which are popularly termed as lab-on-a-chip or μTAS (micro total analysis system). To address this ultimate goal, novel miniaturized, integrated and digitized chips are required in almost every field of biology, chemistry and biotechnology including cell biology, molecular biology, genomics, proteomics, enzyme kinetics, tissue engineering, stem cell engineering, and neurobiology.

In this dissertation, we present invention and application of miniaturized integrated chips and technology for conducting enzyme-catalyzed assays. These chips rely on a novel microchannel and droplet based technology for the generation of concentration gradients with nano- and picoliter-scale sample volumes. The chips has

inbuilt integration of sample metering, mixing, and detection steps involved in many biological and chemical experiments. This integration facilitates kinetic characterization and evaluation of dose response with single experiment. These chips could achieve simultaneous, parallel and independent reactions with nano- and picoliter-scale sample volumes, unlike its conventional tube and pipette-based and robotics-based methods. The present chips and technology is highly suitable for applications where the reagents or samples are highly expensive or limited in availability.

With heavy heart, dedicated to my late father,
Ranappa Jambovane (1943-2011)
—an amazing soul, painter and sculptor—
who instilled in me the value of honesty,
pursuing higher education, and always aspiring for excellence.

Acknowledgments

"A human being is a part of the whole, called by us the 'Universe', a part limited in time and space. He experiences himself, his thoughts and feelings, as something separate from the rest—a kind of optical delusion of his consciousness. This delusion is a kind of prison for us, restricting us to our personal desires and to affection for a few persons nearest to us. Our task must be to free ourselves from this prison by widening our circle of compassion to embrace all living creatures and the whole of nature in its beauty. Nobody is able to achieve this completely, but the striving for such achievement is in itself a part of the liberation and a foundation for inner security."
—Albert Einstein, New York Post, 28 November 1972

To lord Ganesha, ||वक्रतुण्ड महाकाय सुर्यकोटि समप्रभ निर्विघ्नं कुरु मे देव सर्वकार्येषु सर्वदा||. To Goddess Saraswati, ||सरस्वति नमस्तुभ्यं वरदे कामरूपिणि||. To my spiritual guru Pujya Gurudev Swami Chinmayananda for bringing me closer to Lord Krishna and teaching me how to become a better human being through the teachings of the Bhagavad Gita, the Upanishads, and the science of Vedānta.

I am sincerely thankful to my advisor Dr. Jong Wook Hong for steering me away from conventional research area and into an amazing world of microfluidics. I am grateful for the guidance, the always-open door and the opportunity to undertake work on a new and exciting field of research with a real physical application. The author would like to extend a special thanks to Dr. Hong for his immense help, devotion and mentorship throughout all phases of this research.

The author is also thankful to Dr. Jeffrey W. Fergus and Dr. Barton C. Prorok for agreeing to be on his dissertation committee and providing many valuable suggestions during his study at Auburn. The author is sincerely thankful to Dr. Evert C. Duin for the valuable time and guidance in explaining critical issues about experimental and theoretical enzyme kinetics. Thanks also to Dr. Duin for sharing his enzyme kinetics

expertise for the publication of our research papers. Special thanks to Dr. Maria L. Auad for agreeing to be an external reader with a big smile. The author also sincerely thanks Dr. Joe Olechno, Labcyte Inc., for explaining the criticalities of drug screening matrix and dose response analysis.

The author would also like to acknowledge the company of his past and current research group members. The author would also like to mention the names of Dr. Jae Young Yun, Dr. Woon Seob Lee, Hoon Suk Rho, Dr. Duckjong Kim, and Dr. Morgan Hamon for help and valuable inputs. Thanks to Austin Adamson, Kirn Cramer, Jing Dai, and Tina Chen for timely help.

I am deeply indebted to my great friends and relatives whose help, stimulating suggestions and encouragement helped all throughout. Most importantly, I would like to thank my following friends and relatives: Uday Sorte, Naveen Singh, Ramesh Nipanal, Ashok Nipanal, Sagar Kamble, Laxmanrao Kamble, Gautham Jeppu, Shantanu Mulay, Anjeli Singh, Anjani Kumar, Pradeep Rao, Kalpesh Shatye, Amol Thote, Kailash Jajam, Prasanthi Pallapu, Vishal Srivastava, Nitilaksha Hiremath, Prateek Hejmady, Maulik Lukkad, and Vivek Patil.

Finally, I thank those that are dearest to me, who have loved me unconditionally, and stood by me during times of confusion and frustration. My parents, Ranappa Jambovane and Kasturi Jambovane, who sacrificed a life of material comfort to put me through the best education in India. Their unconditional love, unwavering trust, and constant support have materialized into who I am today. My caring siblings Madhavi, Megha and Omkar have always believed in my dreams, loved and supported me unconditionally. My loving wife, Seema, has helped me to come out of many difficult

emotional situations. I cannot thank her enough for her support, unconditional love, sacrifice, patience and understanding.

This research was partially supported by a grant from Marine Bioprocess Research Center of the Marine Bio 21 Project funded by the Ministry of Land, Transport and Maritime, Republic of Korea. We also acknowledge partial support from the National Institutes of Health (NIH R01 008392).

Table of Contents

List of Tables

List of Figures

List of Abbreviations

ASV	Surface area to volume ratio
DNA	Deoxyribonucleic acid
FAM	Fluorescein
FDA	U. S. Food and Drug Administration
HPLC	High-performance liquid chromatography
MMP-2	Matrix metalloproteinase-2
MMP-9	Matrix metalloproteinase-9
PDMS	Polydimethylsiloxane

Chapter 1

INTRODUCTION

1.1 Introduction

This chapter reviews the fundamentals of microfluidics alongwith the basic components required in the fabrication and working of microfluidics devices for determining enzyme kinetic parameters and conducting drug dose response analysis. Later in this chapter, basics of enzyme and enzyme kinetics are included. The enzyme-catalyzed reactions are mathematically described in addition to the derivation of key kinetic parameters. Finally, an outline of the dissertation is presented.

1.2 Background and Motivation

1.2.1 Microfluidics

Microfluidics is a multidisciplinary area, encompassing physics, chemistry, engineering and biotechnology, which study the behavior of fluids at volumes thousands of times smaller than a common droplet. More precisely, It is the science and technology of systems that process or manipulate small (10^{-9} to 10^{-18} litres) amounts of fluids, using channels with dimensions of tens to hundreds of micrometres. {Nguyen, 2002 #1;Whitesides, 2006 #4}. Typical advantages of microfluidics includes: lower consumption of sample volumes and hence less wastage, reduction in the cost of sample usage, faster reaction due to improvement in diffusion, heating and cooling, better process control leading to better results, integration of numerous steps on a single

chip{Gravesen, 1993 #2;Tabeling, 2005 #3}. Integration is key part of microfluidic device and integrated microfluidic device is basically a miniaturized device that handles tiny amount of sample in micro/nanometer scale channels; which also automates and integrates many biological or chemical processing{Whitesides, 2006 #4}. However, the field of microfluidics is still under development and hence to fully exploit the above mentioned advantages it will require some time{Whitesides, 2006 #4}.

The development of microfluidics started around three decades before with the development of gas chromatography and Inkjet printer{Gravesen, 1993 #2}. Since then it flourished significantly with the application for chromatography, electrophoretic separation system, electro-osmotic pumping system, diffusive separation system, micromixers, DNA amplification, cytometers, chemical microreactors nearly in a chronological order{Tabeling, 2005 #3}. In recent time, microfluidic systems have also attracted diverse and well-known potential applications including flow cytometry{Fu, 2002 #5}, protein crystallization{Hansen, 2002 #6} , DNA extraction{Hong, 2004 #7}, digital PCR amplification{Warren, 2006 #8}, stem cell culture{Gomez-Sjoberg, 2007 #9}, for synthetic ecosystem consisting of *Escherichia coli* populations{Balagadde, 2008 #10}, determination of enzyme kinetic parameters{Jambovane, 2009 #11}, catalytic competence analysis{Jambovane, 2011 #175}, single-cell genomics{Kalisky, 2011 #299} RT-qPCR of single cells{White, 2011 #300}, single hematopoietic stem cell proliferation{Lecault, 2011 #302}, megapixel digital PCR{Heyries, 2011 #301}, and dose response analysis{Yun, 2011 #315;Miller, 2012 #212}.

1.2.2 Key Concepts in Microfluidics

Laminar flow

Laminar flow is a well-streamlined flow where particles move parallel to the direction of flow path. The flow inside the microfluidic devices is characteristically laminar. The presence of laminar flow inside the microchannel is confirmed by calculating the value of Reynolds number and by ensuring the parabolic velocity profile (**Figure 1.1a**). In simple terms, the Reynolds number is the ratio of inertial force to viscous force. For laminar flow, the value of Reynolds number is always less than 2100{Nguyen, 2002 #1;Tabeling, 2005 #3}.The small dimensions of channel inside the microfluidic devices decrease the inertial forces and dominate the viscous forces leading to laminar flows. The laminar flow allows two different fluids to flow through the same channel side by side with negligible mixing. Hence, the presence of laminar flow makes the mixing process challenging {Stroock, 2002 #14;Whitesides, 2006 #4;Squires, 2005 #296} as mixing always requires some kind of turbulence.

Surface area to volume ratio

Surface area to volume ratio (SAV) is another important aspect to be considered in microfluidic devices. SAV is defined as the ratio of surface area to the volume of fluid under consideration. In microfluidics, the SAV increases many orders of magnitude with decrease in channel dimensions. The higher SAV ensures elevated rate of reaction and heat transfer. During flow of particles through microchannel, the higher value of SAV creates adsorption of macromolecules to the channel surface. Higher SAV of liquid in microchannel make it suitable for efficient capillary electrophoreses. Biological cell also have higher SAV, hence, they can be better handled in microfluidic devices.

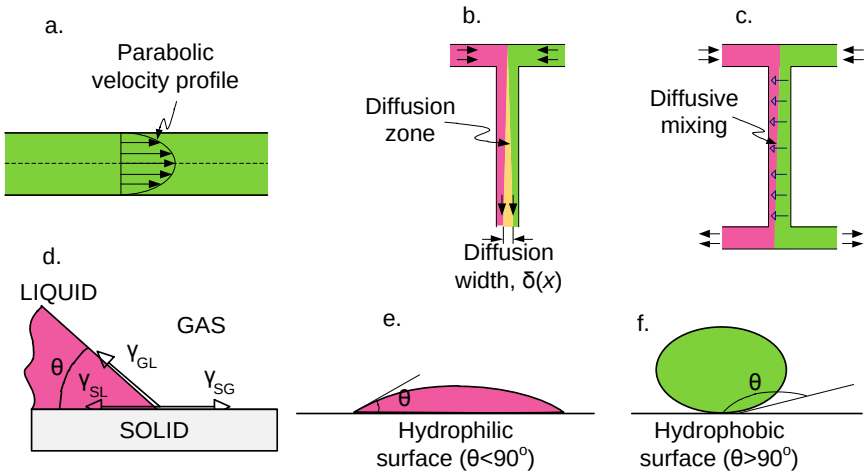

Figure 1.1 | Physical basis of microfluidic devices. (a) laminar flow in microchannel. (b) diffusion between two coflowing fluids. (c) diffusive mixing between two co-flowing laminar flows. (d) wetting interfaces and angles. (e) droplet on hydrophilic surface. (f) droplet on hydrophobic surface. {McGowan, 2011 #176}

Diffusion

Diffusion is one of the most fundamental molecular processes observed in fluid mechanics. Diffusion occurs when two different fluids, with concentration gradients, interact with each other (**Figure 1.1b**). In microfluidic devices, mixing at microscale happens solely by the process of diffusion—due to the absence of turbulence. The diffusion coefficient can be efficiently measured by generating concentration gradient inside the microfluidic channel. This method of measurement of diffusion coefficient has several advantages including saving in reagent, faster response time etc.

Mixing

Rapid mixing of fluids flowing through microchannel is one of the key challenges. In the laminar flow regime, mixing of fluids progresses mainly by diffusion; hence, it happens very slowly (**Figure 1.1c**). To solve this problem, various micromixers,

such as chaotic flow micro-mixers, electrokinetic micro-mixers, peristaltic micro-mixers, etc., have been developed{Chou, 2001 #15;Nguyen, 2005 #16;Stroock, 2002 #14;Oddy, 2001 #17;Chou, 2001 #18;Chou, 2001 #18;Oddy, 2001 #17;Tai, 2006 #19}. In the last decades, various mixing approaches have been proposed and demonstrated to exploit the potential of the microfluidic systems{Haeberle, 2007 #20}.

Wetting

Wetting is an interfacial phenomenon due to the balance of surface energies at gas-liquid-solid surface interfaces{Nguyen, 2002 #1;Squires, 2005 #296}. At microscale, the higher surface to volume ratio makes the process of wetting very important. Fundamentally, wetting occurs at three interfaces: solid-liquid, gas-liquid, and solid-gas (**Figure 1.1d**). The surface energies corresponding to these interfaces are represented by $\gamma_{SL,}$ $\gamma_{SG,}$ and γ_{GL} respectively. The value of contact angle (θ) determines the hydrophilicity and hydrophobicity of surfaces. The nature of wetting phenomenon on the hydrophilic and hydrophobic surfaces is respectively shown in **Figures 1.1e** and **1.1f**. The principle of wetting is exhaustively used in digital (droplet-based) microfluidic devices.

1.2.3 Microfluidic device fabrication

The method of microfluidic device fabrication was picked from the revolution in microfabrication industry used for the fabrication of integrated circuits{Whitesides, 2006 #4}.

Soft lithography

An alternative microfabrication technique based on replication molding that is quite popular in many areas of microfluidics for device development. This technique is

commonly known as soft lithography, due to the use of soft polymer base material. Soft lithography was pioneered by Whiteside's group in Harvard University {Xia, 1998 #27;Xia, 1998 #25;Whitesides, 2006 #174}. Its advantages include the possibility for rapid prototyping, ease of fabrication without expensive equipment, and flexible process parameters. Soft lithography is a basis of many advanced fabrication methods such as multilayer soft lithography. Soft lithography is essentially the curing of polymer on top of a negative mold structure. The process can be divided into two steps: negative mold fabrication and replica casting. The negative mold fabrication methods include the micromachining of silicon{Madou, 1998 #28}, LIGA{Hruby, 2001 #29}, and the photolithographic patterning of photoresist{McDonald, 2000 #24}. Alternatively, inexpensive, quickly produced molds are ideal for most research and prototyping. In addition, as polymer curing times are typically on the order of hours, soft lithography allows for very rapid device fabrication from the stage of design in CAD softwares.

Multilayer soft lithography

Quake's group has developed an advanced form of soft lithography known as multilayer soft lithography, which can fabricate multiple patterned layers of elastomer together by varying the relative composition of a two-component silicone rubber between them{Unger, 2000 #26}. The simplicity of producing multilayers makes it suitable for the fabrication of multi-layered microfluidic device, a difficult task with conventional silicon based microfabrication. The test structures of up to seven patterned layers, each of ~40 μm in thickness, can be created{Unger, 2000 #26}. Because the layered test structure is monolithic—same material for all of the layers—interlayer adhesion failures and thermal stress problems could be avoided.

1.2.4 Microfluidic flow control

Microfluidics holds the promise of integrating all the necessary functions onto a single chip. Flow control is one of the key issues for the successful integration of these functions. Recently various groups working in the research field of microfluidic devices have discovered various flow control strategies. However, electrokinetic, electro-wetting and pneumatic valve based strategies are widely used in the fabrication of highly integrated devices.

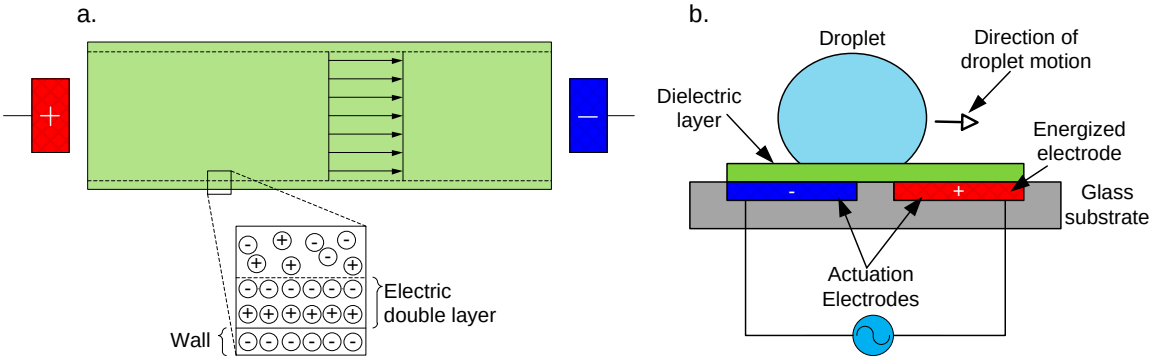

Figure 1.2 | Flow control mechanisms. (a) electro-osmotic flow control. (b) droplet control with electro-wetting. {McGowan, 2011 #176}

Electrokinetic flow control consists of two strategies – electrophoresis and electroosmosis. In electrophoresis, charged particles in the fluid are moved by applying electrical field (**Figure 1.2a**). In sedimentation potential, opposite of electrophoresis, charged particles move without electrical field rather they create electrical field. In electroosmosis, the liquid is moved due to the combined effect charged walls and applied electrical field. In streaming potential, opposite of electroosmosis, liquid is moved, in the absence of electrical field, due to source such as pressure and due to the movement of liquid electrical field is created {Li, 2004 #30;Li, 2008 #31}.

In digital microfluidics, droplets are manipulated on dielectrically coated surface electrodes by applying electric field between the electrodes or between electrode and liquid (**Figure 1.2b**). The dielectric surface is usually coated with hydrophobic material, such as Teflon, to ensure partial wetting with very small contact angle. When electric potential is applied between the electrodes, charges are created and the subsequent force field moves the droplets. In principle, digital microfluidics involves movement of droplets by combined effect of electrostatic and dielectrophoretic forces{Pollack, 2000 #32;Abdelgawad, 2009 #33}.

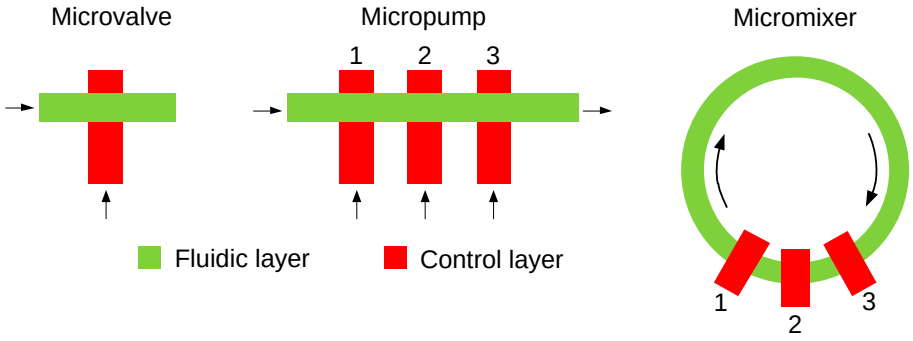

Figure 1.3 | Pneumatic valve-based flow control elements. {McGowan, 2011 #176;Unger, 2000 #26;Chou, 2001 #18}.

Pneumatic valve based flow control allows microfluidic devices to be densely packed, as the area of each valve is very small (100 µm × 100 µm). In the microfluidic device, multiple pneumatic valves could spatially arranged to make various control elements such as micropump and micromixer (**Figure 1.3**). In last few years, exhaustive characterization and the performance improvement of an elastomeric microvalves has been conducted by many researchers{Unger, 2000 #26;Studer, 2004 #34;Jambovane, 2009 #304;Jambovane, 2010 #305}. The shape of microchannel plays very important role in successful working of the valve. It has been observed that rectangular and

trapezoidal-shaped channels have problem with complete closure. However, the round shaped cross section with parabolic profile can close completely when pneumatic pressure is applied **(Figure 1.4)**.

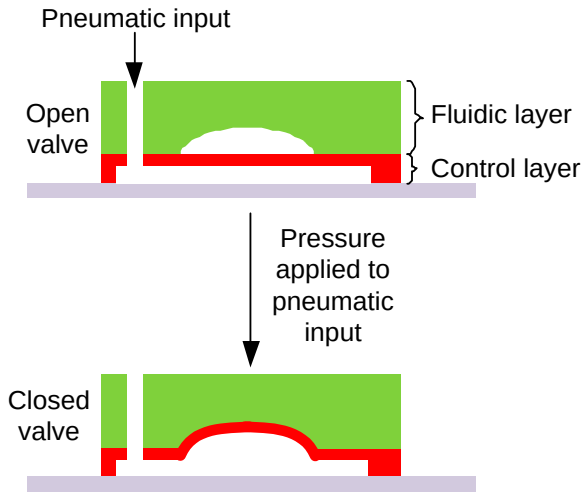

Figure 1.4 | Working mechanism of pneumatic valve. {Unger, 2000 #26}.

1.2.5 Enzymes

The living cell cannot survive without proper function of enzymes{Copeland, 2000 #35;Palmer, 2007 #271}. The living cell involves significant biochemical activity known as metabolism. The metabolism includes chemical and physical change taking part in tissue formation, tissue replacement, food to energy conversion, excretion, reproduction; hence, enzymes are involved in all the activities that are characteristic of life{Worthington Corp, 1972 #273}. These enzymes have three amazing characteristics because of which the working of an enzyme is unique among all biomolecules. First, enzyme increases the rate of a reaction. In many cellular reactions, this rate is million times faster than in the absence of an enzyme{Fersht, 1999 #295}. Second, most enzymes are very specific to react with certain types of substrates to produce products.

This makes enzymes preferred choice for medical diagnostics. Third, most enzymes cover a wide range of activity.

Specifically, enzymes are type of proteins that acts as biocatalyst in the cellular reaction{Palmer, 2007 #271}. As a biocatalyst, the typical enzyme accelerates the

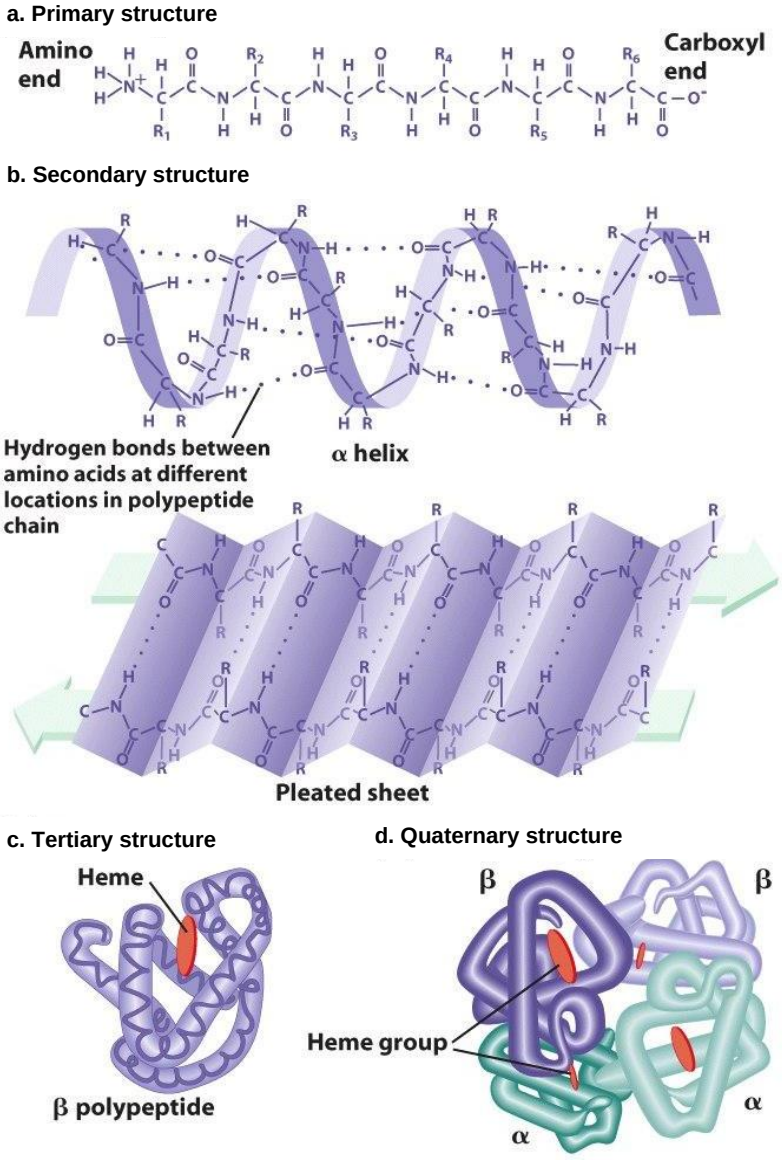

Figure 1.5 | Enzyme structures (a) primary structure. (b) secondary structure. (c) tertiary structure, and (d) quaternary structure. {flashcards, 2012 #310}

rate of cellular reaction by staggering amounts, upto 10^{20} times compared to the catalyzed reaction{Ringe, 2008 #242}. The shape and structure of an enzyme is important for understanding working of an enzyme, which subsequently helps in deciphering that cellular reaction. Until the discovery of James summer in 1926, scientists use to think that enzyme does carry any ordered structure{Ringe, 2008 #242}. The typical three-dimensional structure of enzyme was first given to the world by James Summer through his crystalized structure of urease from jack bean{Sumner, 1926 #269;Palmer, 2007 #271}. Like all proteins, an enzyme consists of long chain of small molecules, called amino acids (**Figure 1.5**). In humans, about twenty kinds of amino acids take part in cellular reactions. For example amino acids glutamine, lysine, and aspartic acid are found in food supplements. The long chain of amino acids in enzyme determines unique three-dimensional shape with features such as helices, barrels, sheets, loops, pockets, clefts, and cages{Langan, 2006 #243}.

For last century, majority of work in enzymology was conducted at ensemble level because enzymes inside cell interact with neighboring protein molecules. However, with these ensemble measurements knowing the working of individual enzyme molecule is not possible. Recently, single molecule enzymology has picked up to show very interesting results. One such result shows that enzymes functions in work and sleep mode, with 30ms of burst activity and 970ms of inactive state{Lu, 1998 #272}. The interesting result could be imagined as where enzyme sleeps for 97% of the time and is awake and works for 3% of time in a day{Engelkamp, 2006 #268}.

1.2.6 Enzyme Kinetics

Enzyme kinetics is a branch of science that deals with study of chemical and physical factors that affect the rate of an enzyme-catalyzed reaction{Sauro, 2011 #294}. The most important factors affecting enzyme-catalyzed reaction include the enzyme, substrate and product concentrations, and any the value of modifiers such as the concentration of inhibitor, pH, temperature and ionic strength. The study of action of these factors could be used for determining the kinetic mechanism and parameters of the enzyme-catalyzed reaction. Most importantly, the events of binding or unbinding of substrates, products, and inhibitors control the reaction rate. To work as biocatalyst, enzyme reacts with substrate, the reactant molecule that binds to the enzyme, to form product. In this enzyme-substrate reaction, enzyme does not undergo permanent chemical change. This basic enzymatic reaction could be expressed as:

$$E + S \underset{k_{-1}}{\overset{k_1}{\rightleftharpoons}} E \cdot S \underset{k_{-2}}{\overset{k_2}{\rightleftharpoons}} E + P \qquad (1.1)$$

where, S is substrate, P is product, E is the free enzyme; $E{\cdot}S$ is the enzyme-substrate complex; k_1, $k_{-1,}$ k_2 $k_{-2,}$ k_3 and k_{-3} are rate constants. The working of an enzyme- catalyzed reaction could be studied by using the reaction shown in equation (1.1), however the rate constants involved in the binding and unbinding of enzyme and substrate are mostly unknown or difficult to determine. In such cases, assumptions are made about the reaction mechanism to reduce the number of constants required for the characterization of an enzyme. This leads to a simplified equilibrium model known as Michaelis-Menten kinetics model, which is given as

$$E + S \underset{k_{-1}}{\overset{k_1}{\rightleftharpoons}} E \cdot S \xrightarrow{k_{cat}} E + P \qquad (1.2)$$

In equilibrium model of Michaelis and Menten, it is assumed that the product has a negligible concentration and so the reverse rate constant k_{-2} in equation could be considered as zero. Therefore, the binding between substrate and enzyme is reversible but product formation is not. Hence, this model is mostly applied for evaluating *in-vitro* kinetic reactions{Fersht, 1999 #295}.

Equilibrium model{Fersht, 1999 #295;Stein, 2011 #232;Segel, 1993 #138}

In the equilibrium model of Michaelis and Menten, the substrate-binding step is assumed to be fast relative to the rate of breakdown of the $E \cdot S$ complex. Therefore, the substrate binding reaction is assumed to be at equilibrium. The equilibrium dissociation constant for the $E \cdot S$ complex (K_S) is a measure of the affinity of enzyme for substrate and corresponds to substrate concentration at $\frac{1}{2}V_{\max}$:

$$K_s = \frac{[E][S]}{[E \cdot S]} \tag{1.3}$$

Thus, the lower the value of K_S, the higher the affinity of enzyme for substrate. The velocity of the enzyme-catalyzed reaction is limited by the rate of breakdown of the $E \cdot S$ complex and can therefore be expressed as

$$v = k_{cat}[E \cdot S] \tag{1.4}$$

where k_{cat} corresponds to the effective first-order rate constant for the breakdown of $E \cdot S$ complex to product and free enzyme. The rate equation is usually normalized by total enzyme concentration, $[E_T] = [E] + [E \cdot S]$:

$$\frac{v}{[E_T]} = \frac{k_{cat}[E \cdot S]}{[E] + [E \cdot S]} \tag{1.5}$$

where $[E]$ and $[E \cdot S]$ correspond, to the concentrations of free enzyme and enzyme–substrate complex, respectively. Substituting equation 1.3 for $[E \cdot S]$ in equation 1.5 yields

$$\frac{v}{[E_T]} = \frac{k_{cat}\left(\frac{[E][S]}{K_S}\right)}{[E]+\left(\frac{[E][S]}{K_S}\right)} \tag{1.6}$$

Manipulation and rearrangement of equation 1.6 yields the velocity of an enzyme-catalyzed reaction:

$$v = \frac{k_{cat}[E_T][S]}{K_S + [S]} \tag{1.7}$$

By defining V_{max} as the maximum reaction velocity, $V_{max} = k_{cat}[E_T]$, equation (1.7) can be expressed as

$$v = \frac{V_{max}[S]}{K_S + [S]} \tag{1.8}$$

The assumptions of the Michaelis–Menten model are:

a) The event of substrate binding and formation of the $E \cdot S$ complex is fast compared to the breakdown of $E \cdot S$ complex. Therefore it could be assumed that the substrate binding reaction occurs at equilibrium.

b) The concentration of substrate remains essentially constant during the time course of the reaction $\left([S_0] \approx [S_t]\right)$. This is partly due to the fact that initial velocities are used and that $[S_0] \gg [E_T]$.

c) The conversion of product back to substrate is negligible, since very little product has had time to accumulate during the small time of the reaction.

These assumptions are based on the following conditions:

- The enzyme is stable during the time course of the measurements used to determine the reaction velocities.
- Initial rates are used as reaction velocities.
- The reaction velocity is directly proportional to the total enzyme concentration.

Steady state model{Fersht, 1999 #295;Stein, 2011 #232;Segel, 1993 #138}

For the derivation of an enzyme catalysis model, the above-mentioned equilibrium assumption and condition is not very typical of an enzyme-catalyzed reaction. Alternatively, a steady-state assumption can be used to obtain the rate equation for an enzyme-catalyzed reaction. The main assumption made in the steady-state approximation is that the concentration of enzyme–substrate complex remains constant with respect to time (i.e., $\frac{d[E \cdot S]}{dt} = 0$). Thus, the differential equation that describes changes in the concentration of the $E \cdot S$ complex in time equals zero:

$$\frac{d[E \cdot S]}{dt} = k_1[E][S] - k_{-1}[E \cdot S] - k_2[E \cdot S] = 0 \tag{1.9}$$

Rearrangement yields an expression for the Michaelis constant, K_M:

$$K_M = \frac{[E \cdot S][S]}{[E \cdot S]} = \frac{k_{-1} + k_2}{k_{-1}} \tag{1.10}$$

This K_M will be equivalent to the dissociation constant of the $E \cdot S$ complex (K_S) only for the case where $k_{-1} \gg k_2$, and therefore $K_M = \frac{k_{-1}}{k_1}$. The Michaelis constant K_M corresponds to substrate concentration at $\frac{1}{2}V_{\max}$. As stated before, the rate-limiting step

of an enzyme-catalyzed reaction is the breakdown of the $E \cdot S$ complex. The velocity of an enzyme catalyzed reaction can thus be expressed as

$$v = k_{cat}\left[E \cdot S\right] \tag{1.11}$$

Substitution of $\frac{[E][S]}{K_M}$ term for $\left[E \cdot S\right]$ and normalization equation 1.11 by total enzyme concentration, $\left[E_T\right] = \left[E + E \cdot S\right]$ yields

$$\frac{v}{\left[E_T\right]} = \frac{k_{cat}\left(\frac{[E][S]}{K_M}\right)}{[E] + \left(\frac{[E][S]}{K_M}\right)} \tag{1.12}$$

Dividing both the numerator and denominator by $[E]$, multiplying the numerator and denominator by K_M, substituting $V_{\max}$ for $k_{cat}[E]$, and rearranging yields the familiar expression for the velocity of an enzyme catalyzed reaction:

$$v = \frac{V_{\max}[S]}{K_M + [S]} \tag{1.13}$$

For the steady-state case, K_S has been replaced by K_M. In most cases, though, substrate binding occurs faster than the breakdown of the ES complex, and thus $K_S \approx K_M$. This makes the models equivalent.

Experimental model{Fersht, 1999 #295;Stein, 2011 #232;Segel, 1993 #138}

Experimentally, the kinetics of enzyme-catalyzed reaction could be studied by tracking the time-based consumption of substrate or formation of product (**Figure 1.6**). For the determination of kinetic parameters, the full reaction progress curve, till all the substrate is consumed, is required. In practice, this is lengthy process and not essential;

and so researcher restrict the attention to the initial part of the reaction till 5 to 10% substrate is consumed{Stein, 2011 #232}. Here, the product formation is directly proportional to the time progress of the reaction and the slope of this linear part is called as initial velocity (v_o).

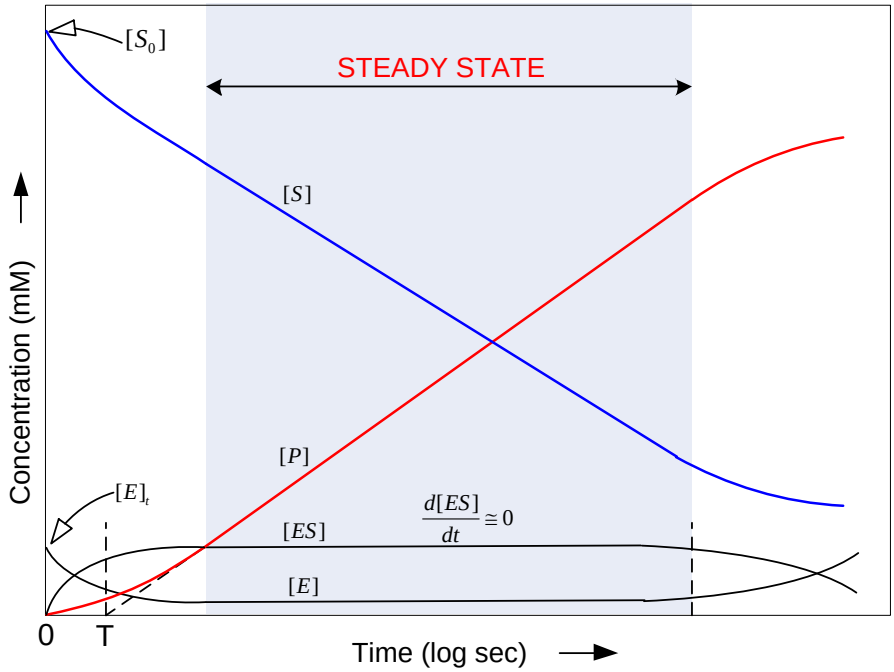

Figure 1.6 | Simulated progress curve for enzyme catalyzed reaction in which E and ES complex do not attain equilibrium. {Segel, 1993 #138}

In the enzyme catalyzed reaction, the study of initial velocity is complex process as it simultaneously depends on various reaction parameters including substrate, enzyme and inhibitor concentrations. However, to simplify the analysis of the enzyme catalyzed reaction only substrate concentration is varied, by keeping the inhibitor and enzyme concentrations constant. The progress curve of enzyme catalyzed reaction with substrate concentration was given by Ludwig Wilhelmy in 1850{Arnaut, 2006 #281} and it follows first order rate law as shown below

$$[S] = [S_0]\exp(-kt) \tag{1.14}$$

Where $[S]$ and $[S_0]$ represent substrate concentration remaining at time *t* and starting substrate concentration, respectively; *k* is the pseudo first-order rate constant. Therefore, the velocity of enzyme kinetics could be given as

$$v = -\frac{d[S]}{dt} = \frac{d[P]}{dt} = k[S_0]\exp(-kt) \tag{1.15}$$

and initial velocity could be written as

$$v_0 = -\frac{\Delta[S]}{\Delta t} = \frac{\Delta[P]}{\Delta t} \tag{1.16}$$

The full progress plot of initial velocity and substrate could be divided into two parts: low substrate concentration and high substrate concentration.

At low substrate concentration $\left([S] \ll K_M\right)$, the initial rate varies linearly with substrate concentration which is a first-order reaction, and equation 1.13 is simplified to:

$$v_0 = \frac{V_{\max}[\mathrm{S}]}{K_{\mathrm{M}}} = \frac{k_{\mathrm{cat}}[E_T][\mathrm{S}]}{K_{\mathrm{M}}} \tag{1.17}$$

where k_{cat} and $[E_T]$ represent the turnover number and the total concentration of the enzyme. However, at high substrate concentrations $\left([S] \gg K_M\right)$, the rate of the reaction is independent of substrate concentration, i.e. zero-order kinetics and equation 1.17 is modified to:

$$v_0 = V_{\max} = k_{\mathrm{cat}}[E_T] \tag{1.18}$$

1.2.7 Enzyme Kinetic Parameters

K_M and k_{cat} for kinetic characterization

The value of K_M is a complex kinetic parameter. It is not equilibrium constant and is represented by following relationship:

$$K_{\mathrm{M}} = \frac{[E][S]}{[E \cdot S]} \tag{1.19}$$

It gives the balance of free enzyme and substrate vs. $E \cdot S$ complex under the conditions of the steady state. But there are circumstances in which K_M approximately equals the dissociation constant for the substrate, K_D. When k_{cat} is very small compared to the rate constant for dissociation of the substrate from the enzyme without any reaction, k_{-1}, we obtain from equation 1.10:

$$K_{\mathrm{M}} = \frac{k_{-1} + k_{cat}}{k_1} \approx \frac{k_{-1}}{k_1} = K_D \tag{1.20}$$

Note that this is an approximation and K_{M} should not be interpreted as equilibrium constant. But commonly k_{cat} is smaller than k_{-1} and equation 1.20 is usually true.

Graphically, there is another interpretation of K_{M}, which is similar to the graphical interpretation of K_{D}. K_{M} is the substrate concentration that gives a velocity equal to one-half of $V_{\max}$:

$$v = \frac{V_{\max}}{2} \tag{1.21}$$

and when $[S] = K_M$, the velocity becomes

$$v = \frac{k_{cat}[E_T][S]}{K_M + [S]} = \frac{1}{2} k_{cat}[E_T] \tag{1.22}$$

This means that the graph in **Figure 1.7** can be used to estimate K_M .

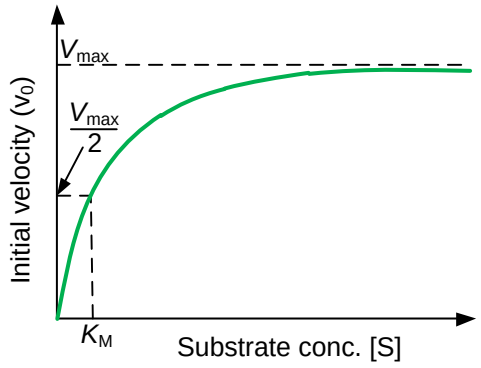

Figure 1.7 | Michelis-Menten kinetic plot showing relationship between substrate concentration and initial reaction of enzyme catalyzed reaction.

Inside the cell, a well-optimized enzyme found to have a K_M value for its substrate that closely matches with the concentration of substrate {Fersht, 1999 #295}. If K_M values are smaller than the concentration of substrate, then the enzyme would be saturated under all conditions. Similarly, if K_M is much higher than the cellular substrate concentration, most of the enzyme is in its free state. Both of these conditions would be inefficient. In comparing K_M values for enzymes with substrate concentrations [*S*], Fersht has been able to show an approximate relationship{Fersht, 1999 #295} (**Table 1.1**). Researchers often are tempted to use K_M as a measure of how tightly a substrate binds to an enzyme active site. This is an approximation that holds good only when k_{cat} is much less than k_{-1}.

Table 1.1 | Metabolite substrate concentration and K_M's for some glycolytic enzymes. {Fersht, 1999 #295}

Enzyme	Source	Substrate	$[S]$ (μM)	K_M (μM)	$\frac{K_M}{[S]}$
Glucose 6-phosphate isomerase	Brain	Glucose 6-phophate (G6P)	130	210	1.6
	Muscle		450	700	1.6
Aldolase	Brain	Fructose 1,6-diphophate (FDP)	200	12	0.06
	Muscle		32	100	3.1
Glyceraldehyde 3-phosphate dehydrogenase	Brain	Glyceraldehyde 3-phophate (G3P)	3	44	15
	Muscle		3	70	23
Phosphoglycerate kinase	Brain	(ADP)	1500	70	0.05
	Muscle	3-Phosphoglycerate (3PG)	60	1200	200
Phosphoglycerate mutase	Brain	3-Phosphoglycerate (3PG)	40	240	6
	Muscle		60	5000	83
Enolase	Brain	2-Phosphoglycerate (2PG)	4.5	33	7
	Muscle		7	70	10
Lactate dehydrogenase	Brain	Pyruvate (Pyr)	116	140	1.2

The value of k_{cat} is known as catalytic rate constant or turnover number for the enzyme and can be calculated as shown in equation 1.22 and its units are 1/seconds.

$$k_{cat} = \frac{V_{max}}{[E_T]} \tag{1.23}$$

The catalytic rate constant is a first order rate constant that represents the frequency of decomposition of the $E \cdot S$ complex to form product. Sometimes k_{cat} is also called as the turnover number because it could be considered as the frequency of turnover of substrate to product by an enzyme per active site per unit time, operating at saturation

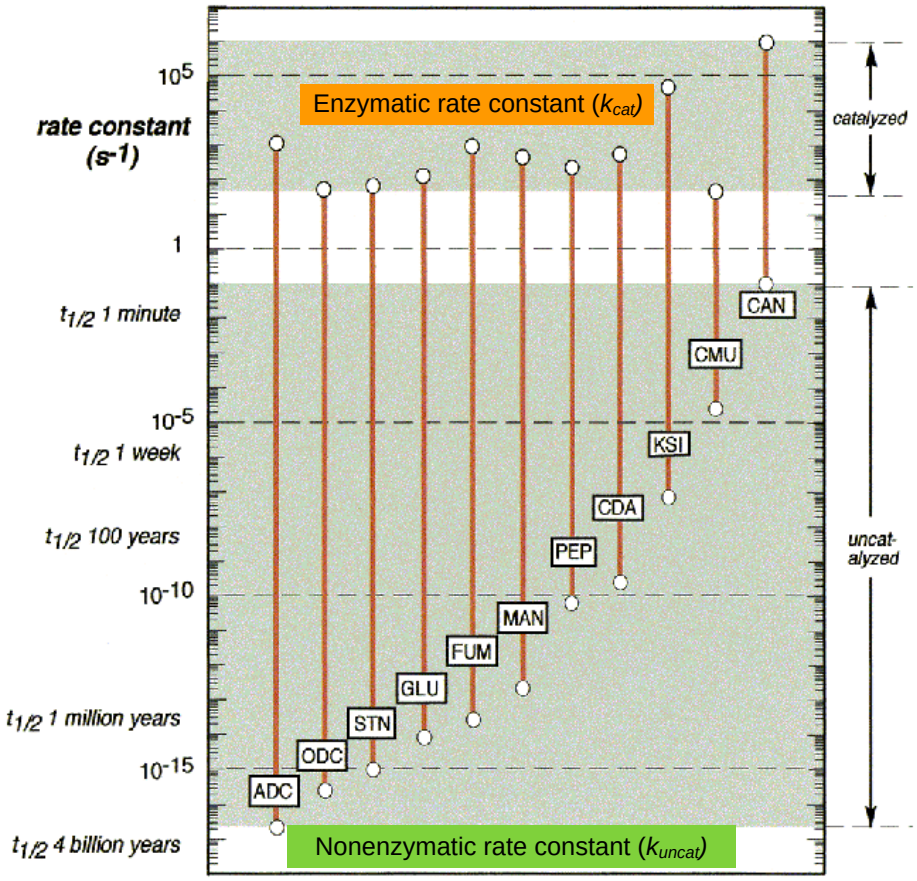

Figure 1.8 | Logarithmic scale of k_{cat} and k_{uncat} values for some representative reactions at 25 °C. The length of each vertical bar represents the rate enhancement by ADC = arginine decarboxylase; ODC = orotidine 5‘-phosphate decarboxylase; STN = staphylococcal nuclease; GLU = sweet potato β-amylase; FUM = fumarase; MAN = mandelate racemase; PEP = carboxypeptidase B; CDA = E. coli cytidine deaminase; KSI = ketosteroid isomerase; CMU = chorismate mutase; CAN = carbonic anhydrase. {Wolfenden, 2001 #275}

conditions{Fersht, 1999 #295}. The turnover number (k_{cat}) is usually very high and some representative values are given in **Figure 1.8** along with the turnover number in the absence of an enzyme (k_{uncat}).

The comparison of k_{cat} with k_{uncat} is a common in enzyme kinetics, as both of these are first order rate constants. The explicit comparison is as follows (the corresponding energy diagram is shown in **Figure 1.9**):

$$S \xrightarrow{k_{uncat}} P \tag{1.24}$$

$$E + S \underset{k_{-1}}{\overset{k_1}{\rightleftharpoons}} E \cdot S \underset{k_{-2}}{\overset{k_2}{\rightleftharpoons}} E \cdot S \xrightarrow{k_{cat}} E + P$$

This comparison provides a useful measure of how much the enzyme is capable of decreasing $\Delta G^{\dagger}$ for a given reaction, by allowing the substrate to product reaction to occur at the enzyme active site. The active site on an enzyme is usually a pocket on the surface of the enzyme into which the substrate can bind.

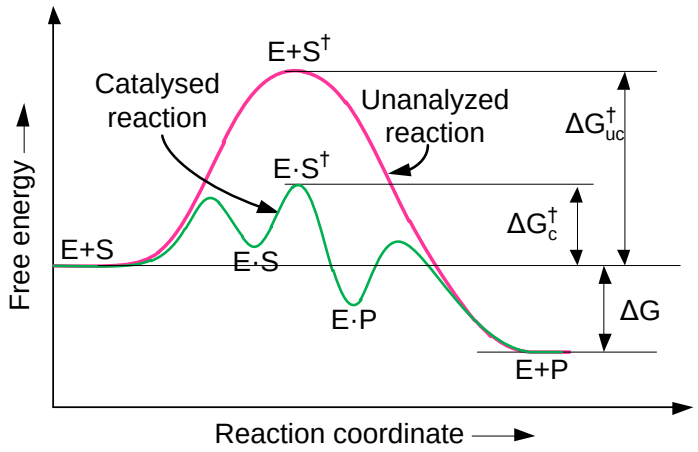

Figure 1.9 | Energy diagram of enzyme-catalyzed and uncatalyzed reaction.

From a comparison of k_{cat} with k_{uncat}, one can obtain a difference in the free energy of activation:

$$\Delta\Delta G^{\dagger} = -RT \ln\left(\frac{k_{cat}}{k_{uncat}}\right) \tag{1.25}$$

where the change in the magnitude of $\Delta G^{\dagger}$ is determined relative to the uncatalyzed rate constant, k_{uncat}.

In real sense, however, it is important to note that consideration of k_{cat} alone is a poor way to describe the catalytic power of an enzyme. It assumes that the reaction starts with the $E \cdot S$ complex, and completely neglects the impact of substrate binding. A more complete analysis must include the other rate constants: k_1, k_{-1}, k_2 and k_{-2}.

IC_{50} for dose response analysis

According to the Food and Drug Administration (FDA), IC_{50} represents the concentration of a drug that is required for 50% replication of viral inhibition *in vitro* {FDA, 2012 #306}. The IC_{50} provides the effectiveness of a drug. It indicates how much of a particular drug or other substance is required to inhibit 50% performance of given biological process—such as enzyme catalysis and bacterial, viral or cell growth. For long time, the values of IC_{50} are widely adopted in laboratories and pharmaceutical industries

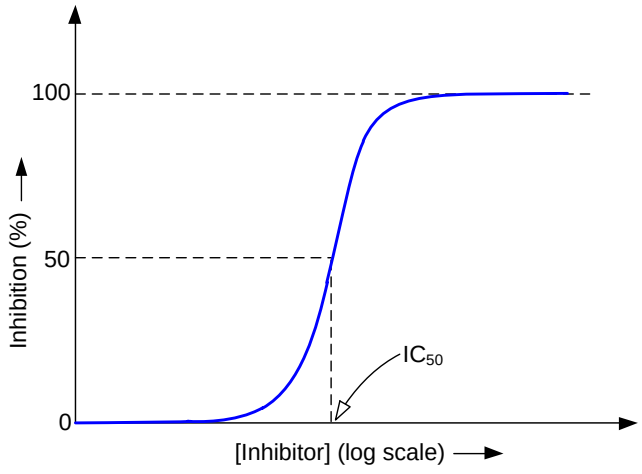

Figure 1.10 | Dose response plot.

in the development of new drugs. Dose-response analysis is used to determine IC_{50}, the kinetic parameter, of inhibitor or drug (**Figure 1.10**).

For IC_{50} value, four parameter nonlinear-logistic-regression model is commonly curve-fitted to the inhibition data. The four parameter model{Motulsky, 2004 #43} is of the form as shown below.

$$\%I = \%I_{\min} + \frac{\%I_{\max} - \%I_{\min}}{1 + 10^{\left(Log\left(IC_{50}\right) - [I]\right) \cdot h}} \tag{1.26}$$

where, IC_{50} refers to median point of the concentration-response plot; [I] represents the concentration of inhibitor; h is the Hill coefficient or Hill slope, which means the steepness of dose-response plot; %I designates percentage inhibiting potency, including minimum and maximum.

k_{cat}/K_M and E_f for catalytic competence evaluation

To compare the affinity of two enzymes to the same substrate, the second order rate constant known as catalytic efficiency is commonly used and is given by{Suckling, 1990 #38;Eisenthal, 2007 #40;Fersht, 1999 #295}

$$\text{Catalytic efficiency} = \frac{k_{\text{cat}}}{K_{\text{M}}} \tag{1.27}$$

However, the exclusive use of the ratio k_{cat}/K_M suffers from many pitfalls{Ceccarelli, 2008 #39;Eisenthal, 2007 #40}. Hence, the parameter called efficiency function (E_f)—also known as practical catalytic efficiency—is widely used in order to explore the performance of the enzyme further{Albery, 1976 #41}. The efficiency function is given by the following equation{Albery, 1976 #41;Ceccarelli, 2008 #39}

$$E_f = \frac{k_{cat}}{k_{dif}\left(K_M + [S]\right)} \tag{1.28}$$

where k_{dif} is the rate for diffusion-controlled process between the interaction of enzyme and the substrate. In water, the value of k_{dif} is calculated as 10^9 M^{-1} sec^{-1}.{Garrett, 2005 #42;Bisswanger, 2002 #307} The efficiency function is defined as the ratio of rate of the catalyzed reaction to the maximum theoretical rate{Albery, 1976 #41;Ceccarelli, 2008 #39}. Hence, the value of E_f is a good indicator of effectiveness of enzyme as a catalyst. For enzyme to be a perfect catalyst, the value of E_f should be 1. In equation 1.28 the substrate concentration plays a major role in estimating the catalytic competence of enzymes. To determine the effect of substrate concentration on E_f, the following equation could be of guidance,

$$\lim_{[S]\to 0} E_f = \frac{k_{cat}}{k_{dif}\left(K_M\right)} \tag{1.29}$$

Based on equation 1.28 and 1.29, we can observe that the catalytic efficiency (k_{cat}/K_M) is an indicator of enzyme efficiency only at [S] = 0. Hence, the exclusive use of k_{cat}/K_M become unrealistic and not adequate to compare the catalytic competence of two enzymes—catalyzed by the same substrate. Hence, to evaluate the catalytic competence further the use of efficiency function, E_f is most appropriate{Eisenthal, 2007 #40}.

1.2.8 Importance of enzyme kinetic parameters

Biocatalyst

Enzymes-catalyzed reaction does not occur in isolation. Typically, the enzymes take part in large biochemical pathways, mostly metabolic. In metabolic pathways, each

enzyme converts substrates into one or more products through multiple enzyme-catalyzed reactions and hence the typical path of enzyme-catalyzed reactions is very difficult to track (**Figure 1.11**).

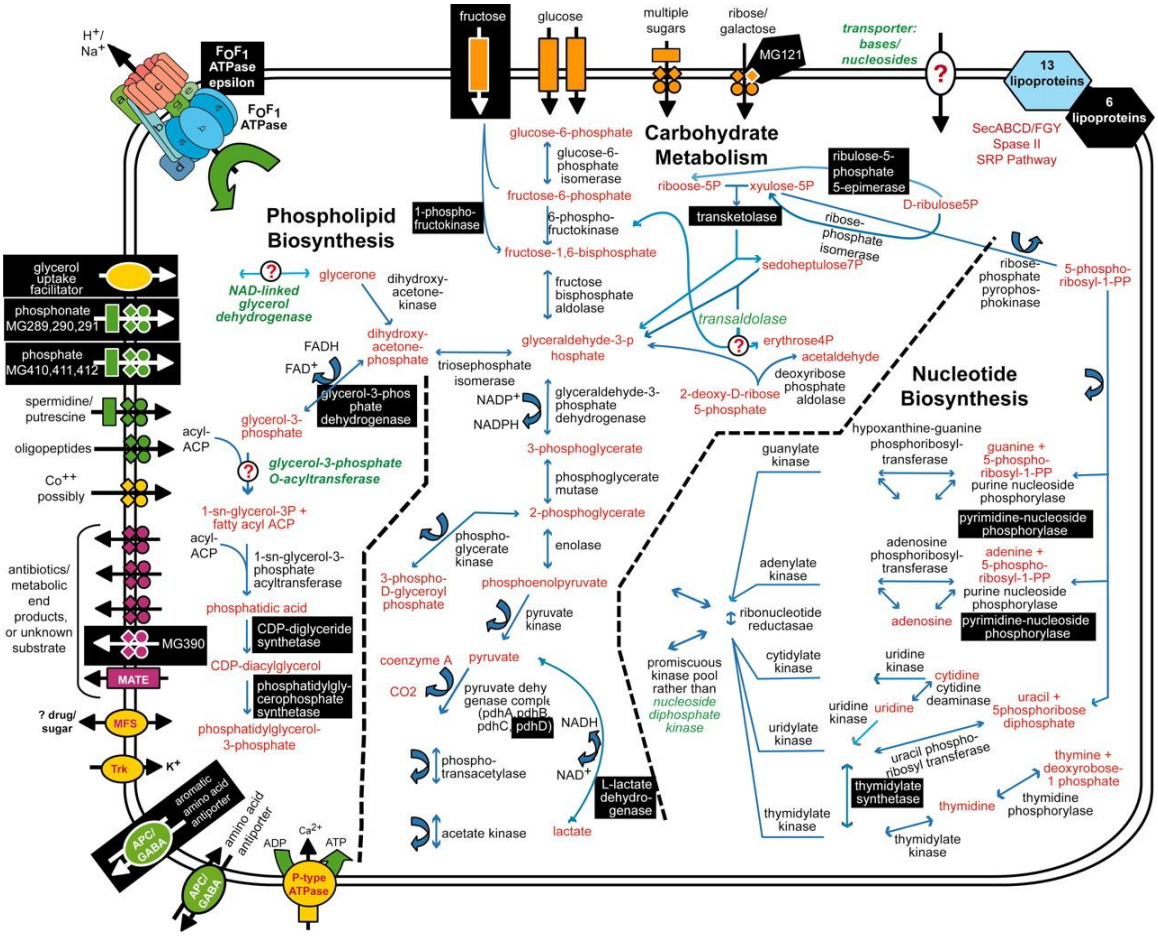

Figure 1.11 | Metabolic pathways and substrate transport mechanisms encoded by *Mycoplasma genitalium* bacterium. {Glass, 2006 #288}

Drug discovery

Developing a new drug is a complex, time-consuming and an expensive process (**Figure. 1.12**). Typically, around 10–16 years are required for the development of single new drug, from starting a project to the launch of a drug in the market{Adams, 2006 #308}. The cost for the development of single drug has estimated to be around $500

million to more than $2,000 million{Adams, 2006 #308;Honig, 2010 #309}. In addition, many expensive, long-term research projects could fail to deliver a drug to the market. In this process of drug development cycle, evaluation of different drug candidates based on kinetic parameters, such as IC_{50}, at early drug discovery stages is very crucial for saving the development cost and early launch of the drug.

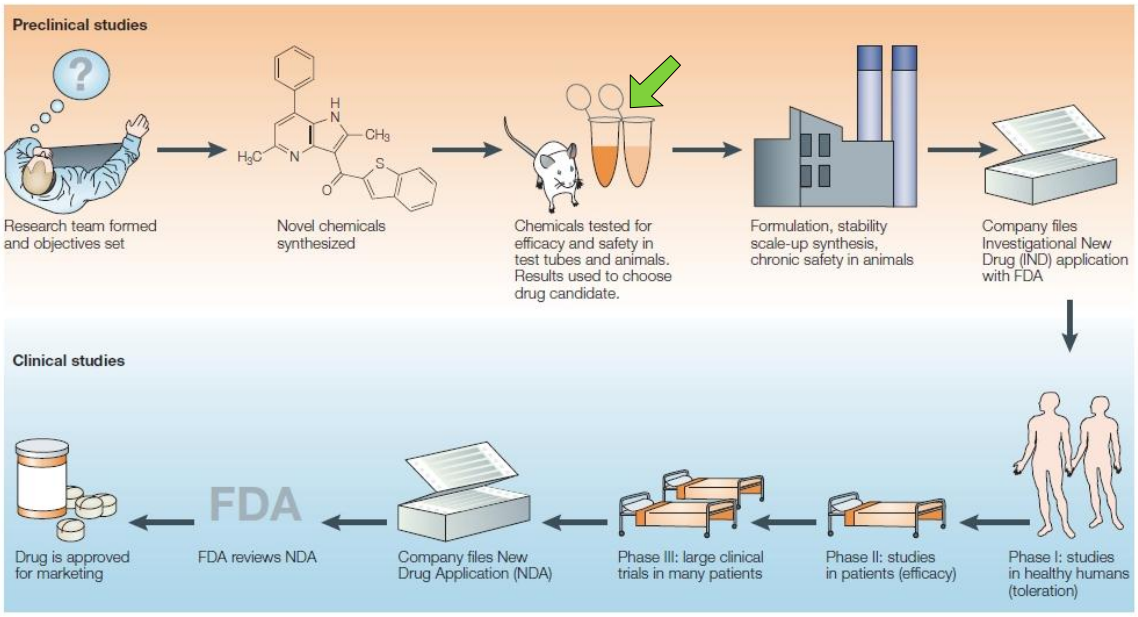

Figure 1.12 | Stages in the drug discovery process.{Lombardino, 2004 #290}

Directed evolution of enzymes

Directed evolution is a process of creation of new class of enzymes, to improve enzyme activity, enzyme selectivity, substrate specificity, solvent tolerance, thermo-stability, and substrate or product inhibition{Turner, 2009 #255;Tracewell, 2009 #260}. The process adopted in directed evolution is depicted in **Figure 1.13.** In the directed evolution process, the kinetic parameters play a key role in the screening of evolved enzymes for higher catalytic efficiencies.

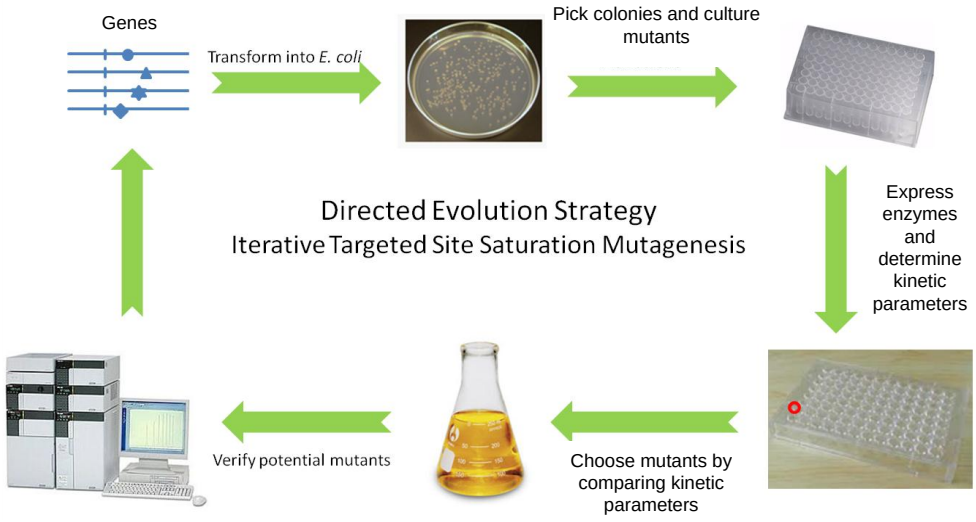

Figure 1.13 | The process of directed evolution of enzymes. {lab, 2012 #289}

1.3 Research Objective and Methodology

1.2.1 Dilution and its types

In chemistry and biological experimentation, for a given protocol, the reagent is frequently diluted to a desired level. Hence, dilution of reagents is one of the most fundamental steps in any biological and chemical assays. The successes of these assays are partly determined by the type of dilution used and the accuracy of dilution process. The accuracy of dilution is strongly controlled by the efficiency of reagent handling used to achieve the required dilution ratio. Two types of dilution methods are commonly used for chemical and biological assays: serial and direct dilutions.

1.3.1.1 Serial dilution

It is the stepwise dilution of a reagent in a buffer solution to create highly diluted solutions. Usually the dilution factor at each step is kept constant; therefore, the resulting concentration could be achieved in geometric progression i.e. in logarithmic scale.

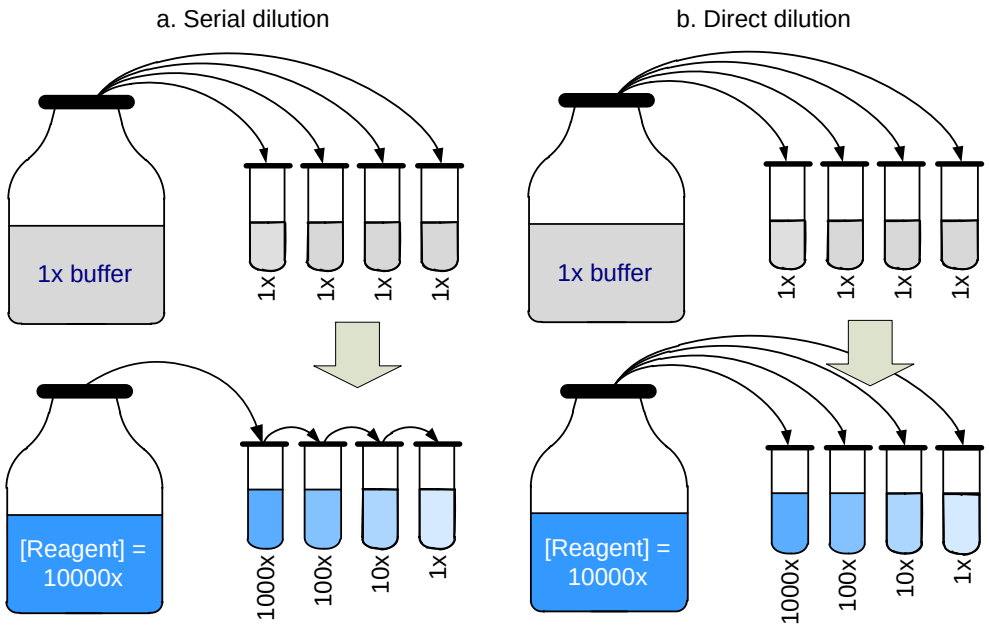

Figure 1.14 | The process of serial and direct dilution methods commonly used in chemical and biological experimentation.

A tenfold dilution for each step is called a logarithmic dilution or log-dilution and a 3.16-fold (100.5-fold) dilution is called a half-logarithmic dilution or half-log dilution.

Serial dilutions are regularly used when the difference between initial stock solution concentration and desired lowest concentration is too large. However, it has two disadvantages:

- The error in the dilution is compounded when the dilution steps becomes more.
- The scale of concentration achieved may not be very flexible.

It involves a sequential series of dilutions performed as shown in **Figure 1.14a**.

1.3.1.2 Direct dilution

Direct dilution is the single step dilution of a reagent in buffer solution, where the dilution factor could be highly flexible, resulting in final concentration in linear as well nonlinear scale. Direct dilutions is not regularly used in conventional chemical and

biological assays because this method of dilution is very difficult to implement at higher dilution ratios where very small amount of reagent, below μL scale, needs to be accurately mixed in large volume of buffer solution, above mL scale. However, the recent availability of robotic and microfluidic systems has solved this problem by precise dispensing of nL and pL scale reagents in buffer. It has two advantages:

- It allows for rapid achievement of a very high dilution ratio.
- It requires a relatively small volume of reagents during dilution.

It involves single step of dilutions performed as shown in **Figure 1.14b**.

1.3.2 Need of concentration gradients based on direct dilution

Conventionally, in the determination of enzyme catalyzed kinetic parameters, serial dilutions—with test tubes, vials and microwell-plates and many microfluidic devices—are routinely used for the generation of a concentration gradient{Seefeldt, 1995 #72}. However, it is well known that the serial dilution method introduces ample errors through pipetting that directly affect the precision of each dilution ratio. To determine kinetic parameters, considering the required multiple steps of dilution for the realization of wide concentration ranges of substrate or inhibitor concentrations, the error in each step of serial dilution could lead to compounding of errors after several steps of serial dilution. This could affect the evaluation of kinetic parameters of enzymes, drug candidates and their realistic comparisons.

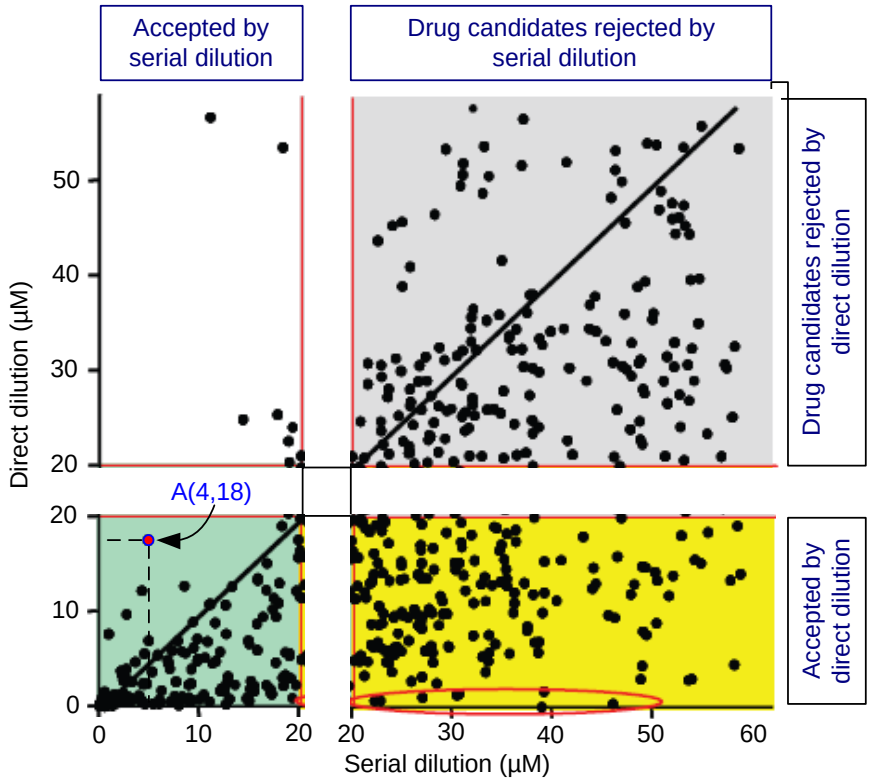

Figure 1.15 | Drug screening matrix showing efficiency of dilution methods in the drug candidate selection in the drug discovery process. Modified from {Harris, 2010 #88;Olechno, 2006 #87}

To demonstrate the extent of errors involved in the serial dilution process, one remarkable study was conducted by Brystal-Myers Squibb—a leading pharmaceutical company. In this study, IC_{50} values of around 1000 drug candidates were independently determined by using serial dilution and direct dilution methods both. The results of this study were summarized in plot shown in **Figure 1.15**. In this plot, each data point designate results of single drug candidate. The x and y-values of each data point indicates the IC_{50} values obtained by serial and direct dilution methods, respectively. For example the drug candidate A(4,13) designate $IC_{50}(X)$= 4 µM by serial dilution and $IC_{50}(Y)$= 13 µM by direct dilution methods. In the drug screening process, the acceptance criteria for the selection of the drug candidates was set at IC_{50}= 20 µM; that means the drug

candidates with IC_{50} values greater than 20 µM were considered less potent and ineffective—i.e. the drug candidate require more quantity of drug for the same effect—and hence rejected in the drug screening.

Therefore, as shown in **Figure 1.15**, the drug candidates in green box, around 59% in number, were accepted by both the dilution methods while the candidates in grey box, ~ 30% in number, were rejected by both the methods. The candidates in the yellow box showed surprising result, where the candidates were accepted by direct dilution but rejected by serial dilution. In other words, more than 110 candidates (~10%) were falsely rejected by serial dilution method. This false rejection of candidates could be attributed to the dilution errors encountered during serial dilution. It is assumed that the serial dilution errors could be because of compounds adsorbing to the plates and pipette tips during the transfer of reagents from pipettes to the plates or tubes{Harris, 2010 #88;Comley, 2007 #247}. In the case of hydrophobic solvent and drug samples, the adsorption of samples and corresponding dilution errors are more prominent. The errors in serial dilution also severely affects the realistic comparison of drug candidates based on IC_{50} values {Hüser, 2006 #73}. Hence, for the accurate determination of kinetic parameters, generation of concentration gradients from direct dilution is of paramount importance.

1.3.3 Microfluidic-based concentration gradients

In last decade, concentration gradient is generated using various microfluidic devices based on different dilution strategies. In our devices, used for the determination of kinetic parameters and dose response analysis, we used two different strategies: microchannel-based processors and droplet-based processors.

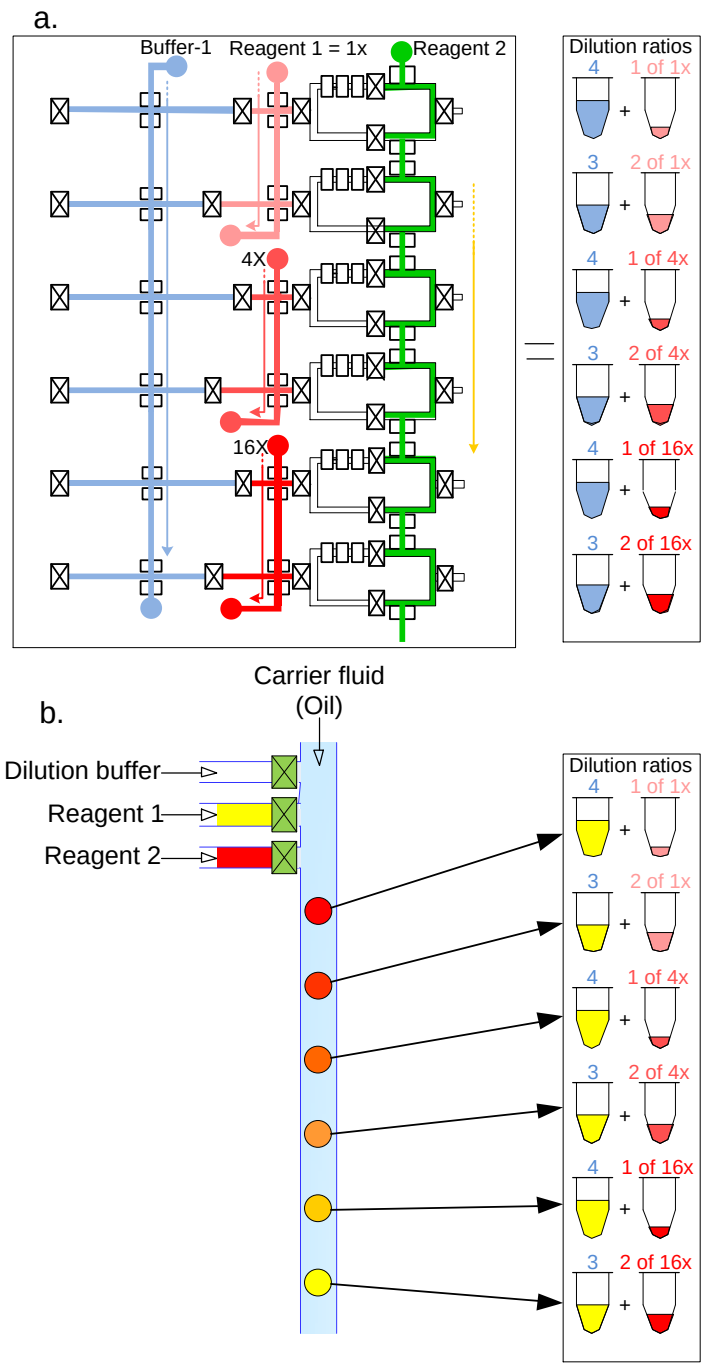

Figure 1.16 | Strategy for concentration gradient generation. (a) microchannel-based processors. (b) droplet-based processors.

Microchannel-based processors

Microchannel-based processors are used to achieve direct dilution of reagents and the subsequent generation of concentration gradients. In this strategy, the reagents are

contained inside the part of microchannel using pneumatic valves (**Figure 1.16a**). The detailed working of these processors is explained in Chapter 3 and 4.

Droplet-based processors

Here, flexible droplet-based processors are generated and used for achieving direct dilution of reagents and for the subsequent creation of concentration gradients. In this strategy, the enzyme-catalyzed reactions are conducted inside compartmentalized droplets, generated by using valve-based mechanism (**Figure 1.16b**). The detailed working of these droplet processors is explained in Chapter 5 and 6.

1.4 Organization of Dissertation

The dissertation is organized into six chapters. The details of each chapter are provided below.

Chapter 1 introduces the fundamentals of microfluidics, enzyme, enzyme kinetics and kinetic parameters. This chapter also discusses the need of direct dilution methods and the strategies adopted for the generation of concentration gradients using direct dilution method.

Chapter 2 presents literature survey of microfluidic devices published in the area of enzyme kinetics, especially for the determination of kinetic parameters and analysis of dose response plots. The literature survey is divided on the basis of working of microfluidic devices used for the determination of kinetic parameters. The devices and methods could be divided into two parts: microchannel and droplet-based methods/devices.

Chapter 3 provides comprehensive development process of microchannel-based platform fabricated which generates a linear gradient of reagent concentrations in eleven

parallel processors. Using β-galactosidase as model enzyme, the determination the key kinetic parameters, K_M and k_{cat}, of enzyme reaction was exhibited with single experiments.

Chapter 4 demonstrates the generation of log-scale concentration gradients of inhibitors on a microfluidic device with a semi-direct dilution capability of reagents for the determination of the IC_{50} values. The device provides a unique tool for hosting a wide-range of concentration gradient for studies that require an equal distribution of measuring points on a logarithmic scale. Using Matrix metalloproteinase IX enzyme and three of its inhibitors, marimastat, batimastat, and CP471474, the IC50 of each inhibitor with a single experiment was evaluated.

Chapter 5 describes the method and modeling of step-by-step microdroplet generation process by using a mechanical valve. Fluidic circuit-based theoretical model has been presented alongwith parametric study of droplet formation in a microchannel with variations of the channel height, the working pressure to drive the liquids in the microchannels, and the viscosity of the dispensed phase. Three steps in the process of droplet generation have been depicted.

Chapter 6 presents a new device for generating a stepwise concentration gradient in a series of microdroplets by using pneumatic micro valves that act as “faucets”. A distinct concentration gradient of a substrate was generated for the determination of the kinetic parameters of two different enzymes using only 10 picoliter-scale droplets. With a single experiment on a chip, K_M and k_{cat} values of matrix metalloproteinase 2 (MMP-2) and matrix metalloproteinase 9 (MMP-9) were obtained, and the catalytic competence of the two enzymes was compared.

Chapter 7 concludes the dissertation with short summary of the key contributions, and provides perspectives including potential applications for future.

Chapter 2

LITERATURE SURVEY

2.1 Introduction

This chapter provides brief literature survey of remarkable methods and devices already established for the determination of kinetic parameters and for dose response analysis. The working, advantages and disadvantages of these methods and devices for the determination of kinetic parameters and dose response analysis are discussed.

2.2 Conventional-based methods and devices

For the first time, the effect of concentration of chemical on the biological function was made by Paracelsus ca. in 1534 and this effect was quantified by A. V. Hill in 1910{Inglese, 2006 #293}. Conventionally, in the determination of kinetic parameters, serial dilutions—with test tubes, and vials—are routinely used for the preparation of a concentration gradient (**Figure 2.1a**). However, it is well known that the serial dilution method introduces ample errors through pipetting that directly affect the precision of each dilution ratio. Considering the needed, multiple steps of dilution for the realization of wide concentration ranges, especially to obtain dose response data, the error in each step of serial dilution could lead to compounding of errors after several steps of serial dilution.

In addition, high-throughput screening (HTS) of chemical compounds is widely used in drug development due to the requirement of high volume screening of drug candidates. In HTS, microplates and liquid handling robots are commonly used for creating concentration gradients and subsequent drug candidate screening (**Figure 2.1b**).

However, screening with HTS has witnessed frequent false negatives and needs comprehensive validation testing {Inglese, 2006 #293;Comley, 2007 #247}.

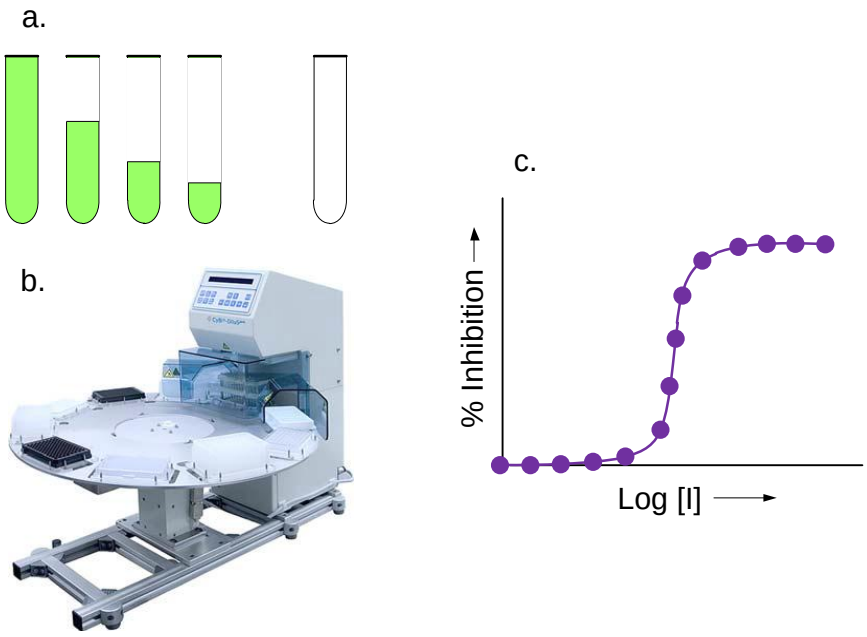

Figure 2.1 | Conventional methods used for dilution. (a) test tube and pipette. (b) automated pipetting machine (c) concentration response curve generated by methods shown in a. and b.

2.3 Microchannel-based devices

During the last two decades, several microreactors have been developed for the determination of K_M and k_{cat} on a chip{Hadd, 1997 #46;Kerby, 2001 #47;Song, 2003 #48;Duffy, 1999 #49;Miller, 2008 #50;Kang, 2005 #51}. **Figure 2.2** illustrates first remarkable experiment of enzyme kinetic study conducted by Hadd et al. with a microfabricated channel network by using an electrokinetic flow control{Hadd, 1997 #46}. The system showed the possibility of determining kinetic parameters using microfluidic channels driven by electrokinetic phenomenon. However, the chip was designed to test just one reaction

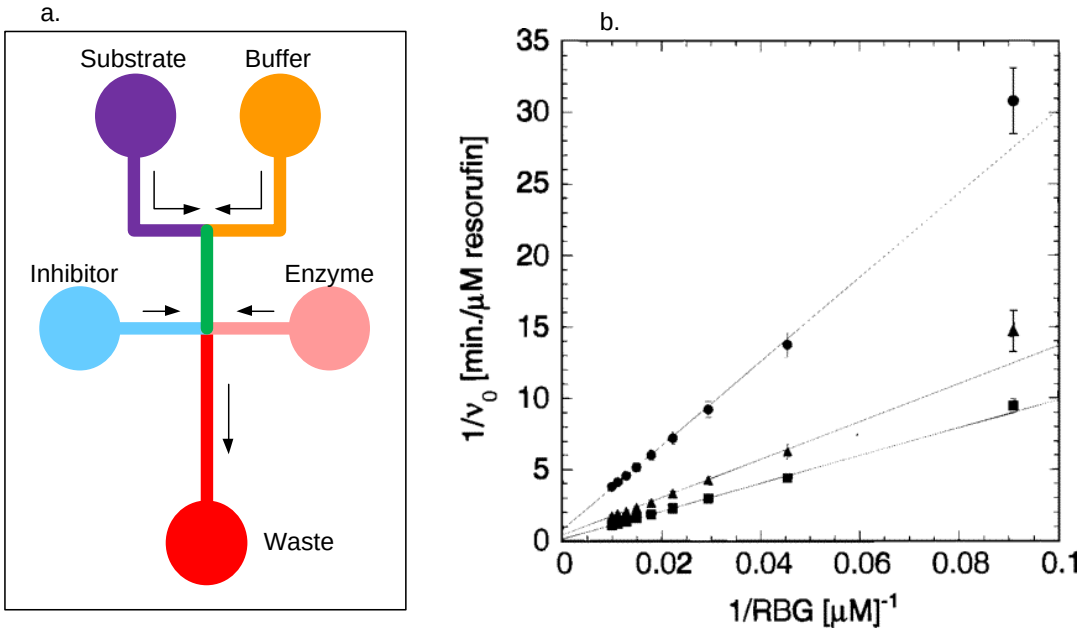

Figure 2.2 | (a) Schematic of the electrokinetic-driven enzyme kinetics chip used by Hadd et al. (b) Lineweaver-Burk plot containing three concentrations of β-galactosidase enzyme and substrate, resorufin β-d-galactopyranoside (RBG). {Hadd, 1997 #3}

condition at a given time; so multiple experiments one after the other were required to conduct full range of substrate concentrations. The reagents—buffer, substrate, enzyme, inhibitor—were mixed by diffusion only, so the mixing was relatively slow, and it was difficult to get an initial reaction rate for higher substrate concentration. In addition, electrokinetic transport and reproducibility and long-term stability have been a major problem{Van Orman, 1990 #52;Lucy, 1996 #53}.

For multiple parallel experiments on a chip, a centrifugal microfluidic system was proposed by Duffy et al. (**Figure 2.3**) with forty-eight independent microfluidic networks was devised{Duffy, 1999 #49}. However, with this system 48 parallel experiments with single concentration of substrate were possible and so become a limitation. The limitation of the unique system was due to lack of internal metering; and this led to the need for

many off-chip experiments to achieve variations of the reaction conditions including substrate concentrations.

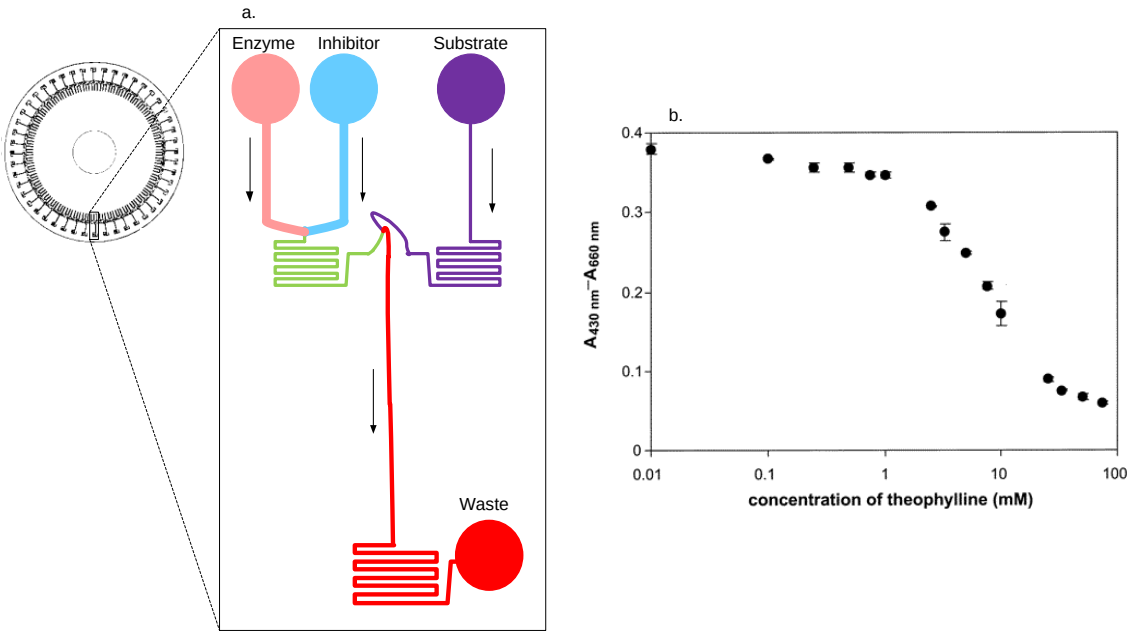

Figure 2.3 | (a) Schematic of the enzyme kinetics chip, controlled by electrokinetic force, with 48 reactors along the circle by Duffy et al. (b) Concentration-absorbance plot shows 15 concentrations of theophylline, ranging from 0.01 to 75 mM, in triplicate (45 assays). {Duffy, 1999 #49}

2.4 Droplet-based devices

Recently, a droplet-based microfluidic system was used to obtain kinetic parameters and demonstrate dose response of inhibitors. By generating and monitoring droplets that have different substrate concentrations, the droplet-based microfluidic system can perform highly flexible and parallel experiments without changing the geometric configuration of the microfluidic network with a highly elaborate flow controller.

Several commercial platforms have been reported by Ellson, Masse and Niles for dose response of drugs using microtiter plates and special ejector, acoustic droplet ejector {Massé, 2005 #79;Ellson, 2003 #80} or piezo dispenser {Niles, 2005 #77;Quintero, 2007 #78} (**Figure 2.4**).

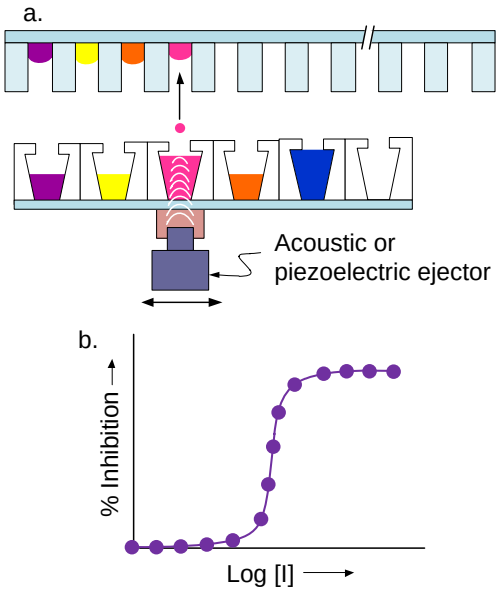

Figure 2.4 | (a) acoustic droplet ejector (ADE) technology based on direct dilution method. (b) representative dose response curve generated by ADE technology. {Harris, 2010 #88;Olechno, 2006 #87}

However, since the microtiter plate is operated in an open environment, the evaporation of reagents and subsequent volumetric errors are of significant concerns at nano or pico-liter scales{Dunn, 2000 #81}. At a given time, the special ejector can be directed to a single micro well for dispensing reagents. Hence, the simultaneous steps of sample delivery, metering, gradient formation, mixing and the detection in all the micro wells are challenging, especially when the reactions are expected in parallel. Based on author's limited knowledge, no dedicated microfluidic system for dose response analysis was published without using microtiter plate and robotic system.

As shown in **Figure 2.5a**, the flow control droplet generation method, also known as T junction method, is one of the widely used methods{Song, 2003 #126;Song, 2003 #121;Song, 2006 #125;Bringer, 2004 #127;Srisa-Art, 2008 #128;Thorsen, 2001 #129;Teh, 2008 #124;Huebner, 2008 #104}.

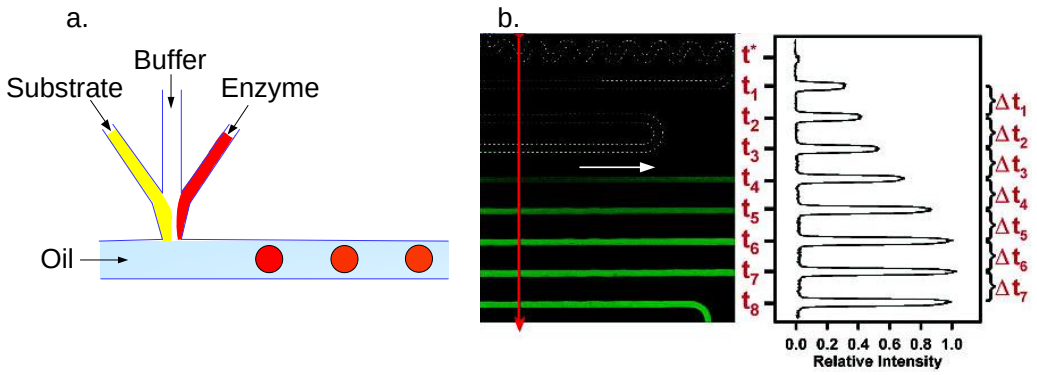

Figure 2.5 | (a) Flow control droplet generation method. (b) The fluorescence intensity was measured along the flow channel to determine kinetic parameters. {Song, 2003 #4;Song, 2006 #125}

In the flow control method, two fluidic channels intersect perpendicular to each other. Usually, a continuous phase flows through the horizontal channel while immiscible dispersed phase flows through the vertical channel or vice versa. When the dispersed phase comes inside the continuous phase channel, it starts forming droplet due to competition between surface tension and shear forces{Thorsen, 2001 #129}. Here as the droplets are formed due to shearing of the dispersed phase by the continuous phase, the sizes of the droplets can be controlled by regulating the flow speeds and the channel widths or by changing the viscosity of each phase{Thorsen, 2001 #129;Song, 2006 #131;Teh, 2008 #124}. The prime advantages of flow control method are uniform droplet size, shape and monodispersity{Teh, 2008 #124}. Flow-control method, however, pose critical disadvantages of lacking the volume control of individual droplets and frequency

of droplet formation{Joanicot, 2005 #132}. Consequently, flexible control of the composition in each droplet reactor is challenging{Song, 2003 #121}. For the determination of kinetic parameters on a chip, a droplet-based microfluidic system was developed by Song et al. (**Figure 2.5a and b**) with T-junction flow droplet method. However, with this system in one experiment, single concentration of substrate could be possible and so multiple experiments were required to cover the range of substrate concentrations so limiting the scope for determining kinetic parameters with single experiment. The limitation of this droplet system was due to lack of controlling individual droplet's concentrations. Recently, examples of controlling individual droplets' sizes by using a mechanical valve have been reported by different groups including a trial to merge the generated droplets{Zeng, 2009 #134} by implementing a passive flow speed control . However, the capability of controlling individual droplet's composition remains unexplored.

Recently Miller et al. {Miller, 2012 #212} have presented another droplet system used for dose response analysis uses a high-performance liquid chromatography (HPLC) phenomenon that produces pulses of inhibitor reagent from microplate into a buffer flow inside capillary tube (**Figure 2.6a**). Each pulse of inhibitor inside capillary tube is subjected to Taylor–Aris dispersion that spreads the pulse from rectangular concentration profile into a Gaussian profile. Therefore, the concentration gradient is created inside a capillary because of smoothed out pulses. The smoothed out pulses are mixed with enzyme and a fluorescent substrate inside the droplet generation chip. With this chip, each droplet produces one data point in dose response plot (**Figure 2.6b)**. The total number of droplets required for producing this dose response plot is around 11,113.

Consequently, the use of this large number of droplets could be considered as unnecessary and very inefficient for producing dose response plot.

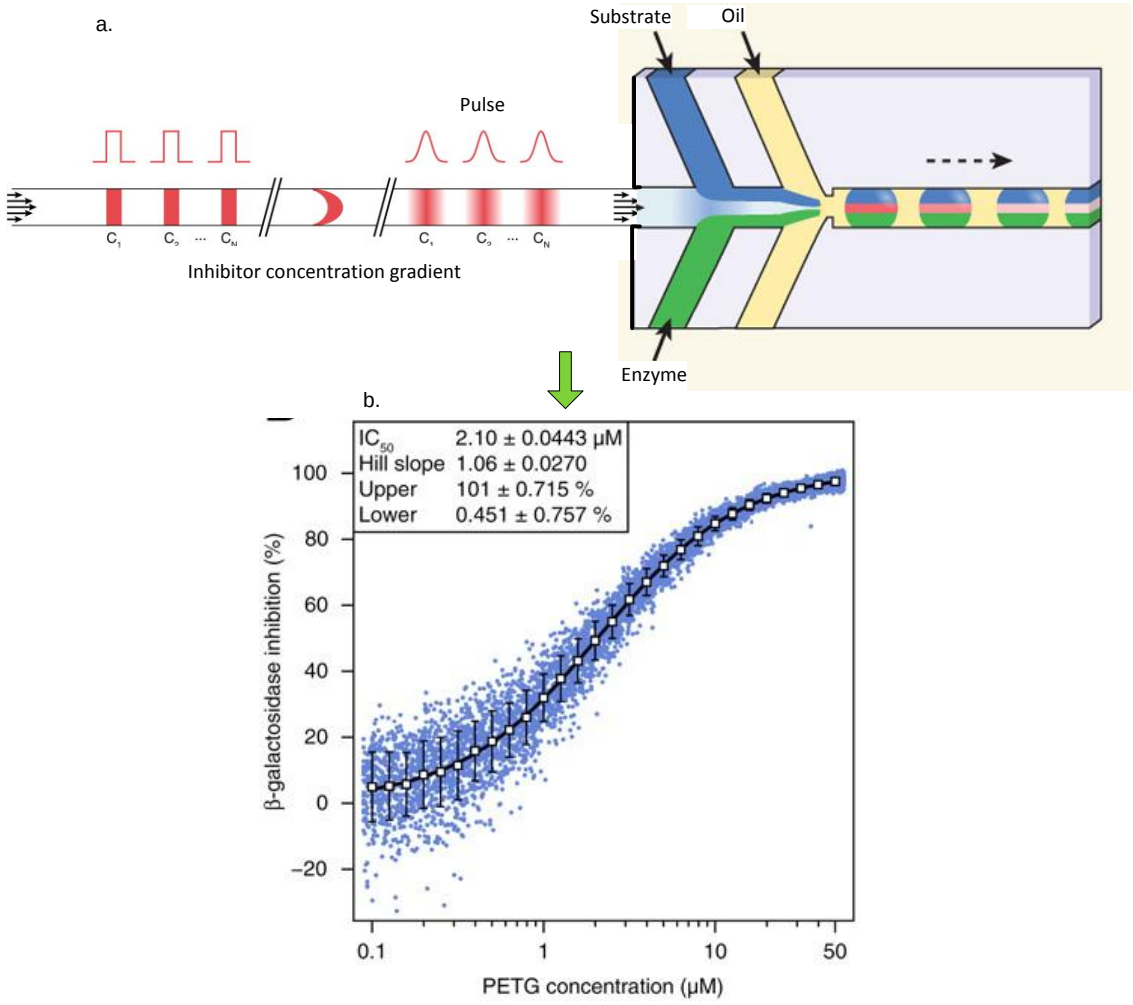

Figure 2.6 | (a)HPLC-based microfluidic droplet screening platform for constructing dose response profile, (b) dose response plot generated from 11,113 droplets (blue dots). {Miller, 2012 #212;Wootton, 2012 #278}

Chapter 3

DETERMINATION K_M AND K_{cat} FROM LINEAR CONCENTRATION GRADIENTS

3.1 Introduction

To determine the kinetic parameters of an enzyme reaction, the initial reaction rate changes at different substrate concentrations are required. Conventionally, reagents have been titrated, agitated, and analyzed in flasks or test tubes to reveal the effect of each reaction condition. In some cases, a pilot plant has been used. To obtain reliable experimental data, experienced operators must control the reactions. Moreover, it is difficult to test numerous different reaction conditions in parallel. In addition, the conventional methods require at least a few milliliters of sample for a single experiment, and this hinders the study of precious samples with limited availability. To overcome these limitations, exploiting the benefits of a microfluidic apparatus, including small sample consumption, short response times, and integration into real-time monitoring systems, is necessary {Manz, 1992 #45}.

3.2 Objective

Here, we demonstrate a multi-step experiment on a chip with eleven parallel microfluidic processors. We borrowed the design strategy from the previous work{Hong, 2004 #55;Marcus, 2006 #54} and extended the parallel architecture from three and four to eleven to determine the key parameters of an enzyme reaction with a single experiment without a significant increase in the number of control valves. Our chip has a

metering unit and a microreactor that has mixing and incubation functionalities. To demonstrate the functionality of the present microfluidic system, we used β-galactosidase and its substrate, resorufin-β-D-galactopyranoside, as the model system. From a single experiment on a chip, we obtained the key parameters for the enzyme kinetics, K_M and k_{cat}.

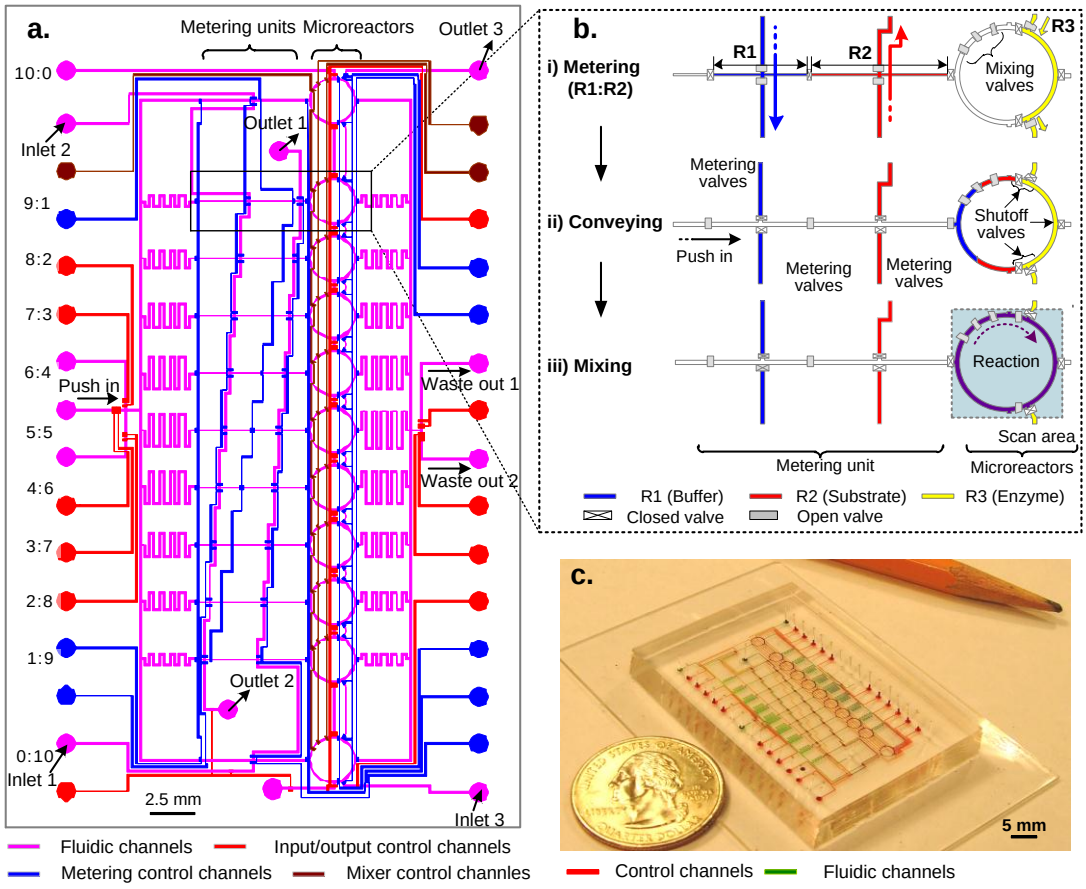

Figure 3.1 | Integrated microfluidic system for parallel processing. (a) a configuration of the microfluidic chip. (b) schematic process flow of i) metering, ii) conveying, and iii) mixing. (c) a photograph of the microfabricated microfluidic device. By using the chip, eleven different reaction conditions are tested at one time.

3.3 Materials and Methods

Chip design

The microfluidic chip has eleven parallel processors, as shown in **Figure 3.1a**. The number of parallel reactions has been expanded from the previous chip design architecture.{Marcus, 2006 #54;Hong, 2004 #55} The mixing ratio of the two reagents is determined by the ratio of the lengths of the metering channel. **Figure 3.1b** shows schematically the configuration of the single microfluidic processor and the process flow in the processor. Each processor has its own microreactor where reagents are mixed and incubated. Each microreactor has three mixing valves generating fluid flow in the microreactor and is connected with a reagent outlet port and three functional microchannels: one is a metering channel, and the others are single-reagent inlet/outlet channels which were used to simultaneously introduce a constant concentration of reagent into the eleven microreactors. The metering channel consists of two microchannels connected in a series, and each microchannel can be separated flexibly by closing and opening a metering valve. The lengths of the metering channels were determined by the positions of the metering valves. Each channel is crossed with its respective reagent inlet and outlet channels. Therefore, we can simultaneously fill each of the 11 metering channels with a reagent. The reagents introduced into the metering channel and the single reagent inlet/outlet channel can be varied according to the purposes of analysis, as described in the Results and Discussion. In **Figure A1a, b** in the Appendix A, a photo of the fabricated microfluidic chip with better resolution and the reagent filling scheme is shown. The flow channels are 100 μm wide and 10 ± 0.5 μm high. The width of the control

channels is 50 μm except for the valve area. For the shutoff valves and mixing valves, the width is typically 200 μm. The inner diameter of each microreactor is 2.4 mm and 100 μm wide and 10 μm high, and the volume is 7.3 nL. The volume of the metered reagent is 60% of the microreactors; 40% is filled simultaneously through single-reagent inlet/outlet channels, which are connected to the eleven microreactors in series.

Chip fabrication

We prepared mask designs by using AutoCAD software (AutoDesk Inc., San Rafael, CA) and printed them on a transparent film at 20,000 dpi (CAD/Art Services, Inc., Bandon, OR). By using photoresist-based photolithographic techniques, we fabricated molds for the two layers. At first, the positive photoresist (AZ P4620) was spin-coated onto a 4-inch silicon wafer. This was followed by UV exposure and development. For reliable opening and closing of the valves, we rounded the cross-sectional shape of the flow channels by heating the mold at 130 °C for 2 min. We made the top thick fluidic layer of the chip by pouring uncured polydimethylsiloxane (PDMS, GE RTV615; elastomer:crosslinker = 10:1) onto the fluidic layer mold to achieve a thickness of 5 mm. We made the bottom control layer of the chip by spin-coating uncured PDMS (elastomer:crosslinker = 20:1) onto the control layer mold at 2800 rpm for 1 min. The resultant thickness of the control layer membrane was 10 ± 0.5 μm. The two layers were cured for 1 h (fluidic layer) and 45 min (control layer) at 80 °C, respectively. We peeled the fluidic layer off from the mold, and punched holes for inlet/outlet ports to the flow channels through the thick layer with a 19-gauge punch (Technical Innovations, Inc, Brazoria, TX). The fluidic layer was aligned over the control layer. We bonded the two layers by baking at 80 °C for 45 min. We peeled the bonded layers off from the control

layer mold, and punched holes for inlet ports to the control channels. Finally, we placed the PDMS chip on a pre-cleaned glass slide (Fisher Scientific Pittsburgh, PA) and kept it in an oven at 80 ^{o}C for 18 h to advance curing.

Device operation

We fabricated a microfluidic chip (**Figure 3.1c**) by using a multilayer soft lithography technique{Hong, 2004 #55;Unger, 2000 #26}. The microfluidic device was composed of two layers as shown in **Figure A3a** in the Supporting Information. The microfluidic device was composed of two layers. When a control channel passed below a flow channel, the thin membrane between the two channels functioned as a valve. By pressurizing the control channel, the membrane was deflected and blocked the fluidic channel. By reducing the pressure, the membrane was returned to its original shape, and the fluidic channel was re-opened. By using this operation principle, we controlled all the valves on a chip.

The microfluidic processors on the fabricated chip go through three major steps, in parallel, for a single experiment composed of eleven enzyme reactions. **Figure 3.1b** shows the step-by-step operation process in a single microfluidic processor. In addition, more detailed operation processes, including the step-by-step valve operation, are shown in **Figure A2** in the Appendix A. First, we infused two reagents into their respective metering channels (inlet channel 1 and 2), which are connected to the metering unit and generate the concentration gradient, and simultaneously filled the third reagent in 40% of the volume of eleven microreactors by the pressure-driven flow through the single reagent in/out channel (inlet channel 3). In this step, we precisely controlled the pressure by using a digital flow controller as described in the

pneumatic control section. Second, we conveyed the two reagents in the metering channel to the microreactor. In this step, the two reagents were separated from the third reagent in the microreactors using two shutoff valves to prevent unwanted initiation of the enzyme reaction. Then, we closed all the shutoff valves around the microreactor and opened the two shutoff valves separating the reagents. In this step, the sequential motion of the three mixing valves circulated and mixed the three reagents in the microreactor. After a reaction was terminated, we washed out the reaction product by introducing a washing buffer from a push-in port to the waste-out ports. In addition, selection of the inlet port for each reagent introduction was varied according to the experimental purpose. For instance, to investigate the effect of enzyme concentration on the reaction rate, we introduced an enzyme solution and an assay solution into reagent inlet channel 1 and inlet channel 2, respectively, to generate the enzyme concentration gradient. We also introduced a constant concentration of the substrate into inlet channel 3. Alternatively, to obtain the reaction rates, we switched the inlet channels for the enzyme and the substrate to inlet channel 3 and inlet channel 1, respectively.

Pneumatic control

We operated the chip by pneumatic control. Since PDMS is permeable to gases, we filled the tubing connecting the pressure source to the shutoff valves with water to avoid bubble formation inside the flow channels. To introduce reagents into the flow channels quickly, we applied pressure, which was precisely controlled by using a flow meter (Alicat Scientific Inc., Tucson, AZ), to the backside of the reagents. The pneumatic control setup consisted of three sets of eight-channel manifolds (Fluidigm Co., San Francisco, CA) controlled by a BOB3 control board (Fluidigm Co., San Francisco, CA).

A digital I/O card (National Instruments Co., Austin, TX) mounted in the computer controlled the switching of each channel of the manifolds through the BOB3 control board. We used a custom-built LabVIEW (National Instruments Co., Austin, TX) program for automatic control of the individual valves.

Enzyme reaction

We prepared stock solutions of 261.8 mg/L of *β*-galactosidase (*Escherichia coli,* 465 kDa) in a reaction buffer (100 mM Tris, 2.0 mM KCl, 0.1 mM $MgCl_2$, 0.1% BSA, and 0.05% Tween 20 at pH 7.8) and 33.3 mM of resorufin-*β*-D-galactopyranoside (Invitrogen Inc., Carlsbad, CA) in dimethyl sulfoxide (DMSO) and stored them at -20 °C. Immediately before use, we diluted the thawed stock solutions with the reaction buffer solution. We purchased all chemicals except for resorufin-*β*-D-galactopyranoside in analytical grade from Sigma Co. (St. Louis, MO) and dissolved them in filtered Barnstead Nanopure water. To conduct the on-chip enzyme reaction, we introduced the enzyme, assay buffer, substrate, and inhibitors into each microchannel. We metered, mixed, and incubated all introduced reagents following the procedures described in the device operation section. To verify the results of the on-chip experiments, we conducted off-chip comparison experiments by using a spectrofluorometer (Perkin-Elmer L55, LAS, Boston, MA). All the conditions were the same except that milliliter volumes of cuvettes were used for the conventional experiments for the present work.

Image acquisition and data processing

We used a modified biochip scanner (arrayWoRx®, Applied Precision, WA) to acquire the images of the on-chip enzyme reaction (**Figure A4** in the Appendix A). We conducted multiple scans of the microfluidic chip during the course of the enzyme

reactions. All the acquired images were 16-bit grayscale, the resolution was 7,800 pixels per inch (PPI), and the pixel size was 3.25 μm. To ensure enough reactor areas for data acquisition, we scanned a complete region of the eleven microreactors (38.3 mm × 3.6 mm) as shown in **Figure 3.1b**. To acquire a rectangular image (38.3 mm × 3.6 mm), we scanned a square image

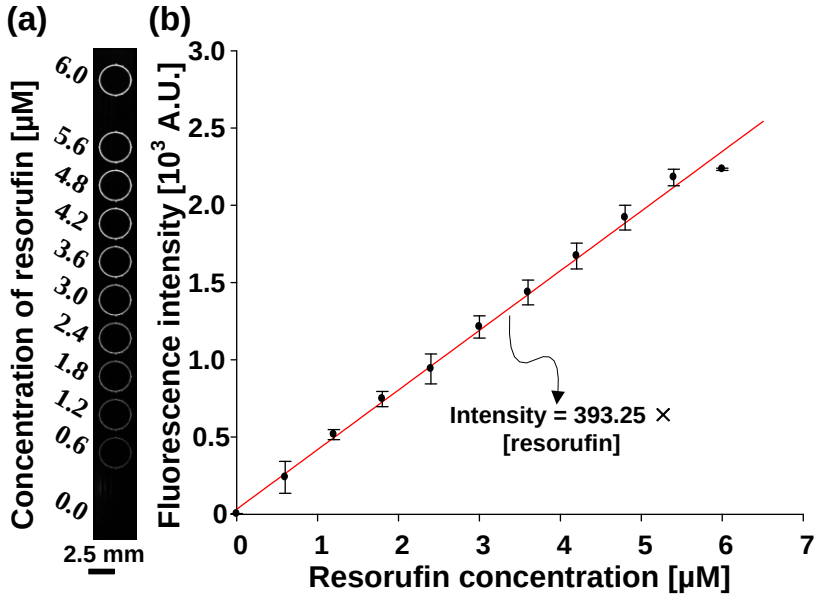

Figure 3.2 | The relationship between the resorufin concentration and the fluorescent intensity. (a) a scanned image of the eleven microreactors showing different concentrations of the fluorescent product, resorufin. Full area of the micro-reactor was scanned. (b) a standard curve showing the fluorescent intensity according to the resorufin concentration increase.

(1.47 mm × 1.47 mm; minimum scanning area of the scanner used in this research) 65 times (0.69 s/scan). Software (arrayWoRx 2.5 Software Suit, Applied Precision, WA) automatically converted the images to the integrated image. The total scanning time of the integrated image (38.3 mm × 3.6 mm) was approximately 45 s, as shown in Figure

A5 in the Appendix A. Within an integrated image, there is a time delay. However, by using the integrated images, when we compared specific points or regions, there was no time delay. We used the time series analyzer of ImageJ software (http://rsb.info.nih.gov/ij/) to analyze and digitize all the fluorescence images. To evaluate the photobleaching rate of resorufin on the chip and correct the digitized data, we measured the changes in the fluorescent intensity over multiple scanning processes. We introduced resorufin (10 μM) into the eleven microreactors, and measured the fluorescent intensities by collecting fluorescence signals through excitation. We observed that 0.7% of the fluorescent intensity was decreased with excitation of each scan up to eighteen times (Figure A6 in the Appendix A). The loss of fluorescent intensities was compensated by using a similar method that was developed to compensate for the photobleaching effect on a multiple scanned confocal image.{McGrath, 1998 #55}

3.4 Results and Discussion

Chip functionality test and standard curve

To demonstrate the gradient forming functionality of the fabricated chip, we formed a gradient of resorufin on the chip by introducing 10 μM of fluorescent resorufin into reagent inlet port 1 and an assay buffer into reagent inlet ports 2 and 3 (**Figure 3.1** and **Figure A1** in the Appendix A). Eleven different reagent concentrations can be generated on a chip with a complete parallel metering process. We transferred the metered reagents of resorufin and the reaction buffer and filled to 60% of the volume of each microreactor, as shown in **Figure 3.1b**. We filled the remaining 40% with the assay buffer. Next, we mixed the three reagents, and, consequently, different fluorescent

intensities according to the different mixing ratios of the reagents appeared in each microreactor. We used the resultant resorufin gradient as a fluorescence standard curve

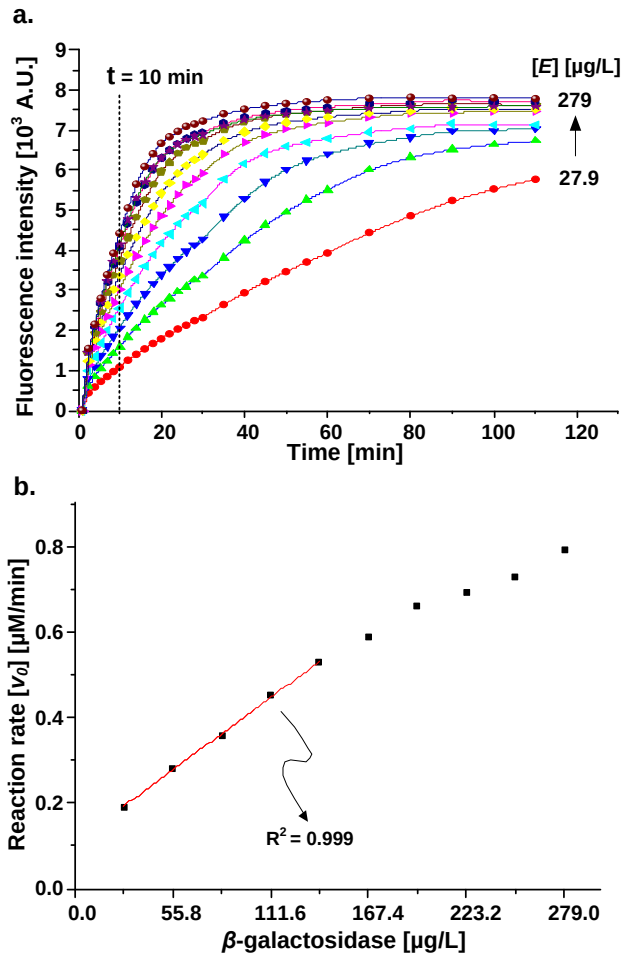

Figure 3.3 | The relationship between the enzyme concentration and the reaction rate. (a) time courses of the enzyme reactions. The concentrations of β-galactosidase ranged from 27.9μg/L to 279 μg/L with an increment of 27.9 μg/L. (b) the reaction rate versus the enzyme concentration.

for product monitoring. The product, resorufin, emits fluorescent light at 585 nm, whereas the precursor molecule resorufin-*β*-D-galactopyranoside does not. Thus, the increase in the fluorescent intensity can be used to monitor the rate of the product yield

catalyzed by *β*-galactosidase when resorufin-*β*-D-galactopyranoside is used as a substrate. **Figure 3.2a** shows a scanned image of eleven microreactors containing different concentrations of the fluorescent resorufin, where its concentration was varied linearly from 0 to 6 μM with an increment of 0.6 μM. We digitized the quantitative information about the different concentrations of resorufin in the image and plotted the information as a standard curve, as shown in **Figure 3.2b**. We used a standard curve to quantify the concentration of product in the experiments presented hereafter. Through the on-chip parallel metering and mixing process, we demonstrated that it was possible to form a series of reagent concentrations with reagent volumes ranging from 440 pL to 4.4 nL. Compared to conventional methods,{Huang, 2008 #56} the microfluidic process reduces the reaction volume by five orders of magnitude.

The adhesion of chemical reagents and proteins on the PDMS is well-known.{Toepke, 2006 #57} We also observed the adhesion of the fluorescent resorufin and the reduced linearity on the resultant standard curve. To prevent the adsorption of resorufin on the channel walls, we added 0.05% of Tween 20 and 0.1% of BSA, which are widely used as blocking reagents {Arenkov, 2000 #58} in the buffer solution. By using the blocking reagents, we observed a linear standard curve and enhanced consistency and reproducibility throughout the experiments.

The micromixer in each microreactor was pneumatically operated as described in the section on chip operation and showed peristalsis similar to the movement of the gut (**Figure A3b** in the Appendix A). When we operated the three consecutive valves of the micromixer in sequence, we created a unidirectional flow. By using pneumatic control, when all the valves located around each microreactor were closed, we mixed the liquid

inside the microreactor. To evaluate the mixing efficiency of the micromixer, we mixed a food dye and water to visualize the mixing phenomena (**Figure A3** in the Appendix A). We captured and digitized the mixing phenomena. When the mixing was completed, the digitized value reached a constant value. The percentage of the mixing performance was increased according to the time increase. We observed 95% and 99.9% mixing performance in 13.8 s and 24.6 s, respectively, under the conditions of our experiments. The average speed was 1.4 ± 0.1 mm/s, and the number of circulation for achieving 99.9% mixing performance was 4.4 ± 0.4.

Optimization of enzyme concentration

The kinetic study of an enzyme starts to determine the length of a linear region in a product formation as a function of time.[2] When the product is over-accumulated, the relationship between the enzyme concentration, [*E*], and initial rate, v_0, becomes nonlinear. Consequently, the rate of product formation is too fast, and the range of linearity is short. Then, it is difficult to obtain a sufficient number of data points to calculate v_0. Therefore, [*E*] of the enzyme reaction needs to be adjusted to control the rate of the product formation and to obtain sufficiently long linearity. To adjust the enzyme concentrations, we formed the concentration gradient of *β*-galactosidase ranging from 27.9 μg/L to 279 μg/L, with an increment of 27.9 μg/L by introducing 465 μg/L of *β*-galactosidase and assay buffer into reagent inlet ports 1 and 2, respectively. 333.3 μM of substrate was also introduced into the reagent inlet port 3 to supply 133.3 μM of substrate to each reaction. **Figure 3.3a** shows the full progress curve of the product formation with the increase in enzyme concentration. The changes in v_0 as a function of [*E*] are also plotted in **Figure 3.3b.** We observed that the enzyme reactions with [*E*] up to 139.5 μg/L

did not reach a plateau in 110 min of reaction time. Hence, we used [*E*] of less than 139.5 μg/L and data points up to 600 s in the experiments presented hereafter.

Determination of reaction kinetic parameters

To determine K_m and k_{cat} on a chip, we measured v_0 with a series of substrate concentration changes, 20−200 μM of resorufin-β-D-galactopyranoside, which was produced by introducing 333.3 μM of substrate and assay buffer into reagent inlet ports 1 and 2, respectively. We used 83.7 μg/L of *β*-galactosidase in the final concentration for each reaction. **Figure 3.4a** shows the time courses of the product formation, in which we observed that the enzyme reactions did not reach a plateau in 130 min of reaction time. The fluorescent intensity increased as the substrate concentration increased. We plotted the initial rate on the Lineweaver-Burk reciprocal plot, *i.e.*, a plot of $1/v_0$ as a function of $1/[S]$, and used linear regression analysis to find the y-intercept ($1/V_{max}$) and the slope (K_m/V_{max}){Cornish-Bowden, 1995 #61}, as shown in **Figure 3.4b**. The average K_m in three independent on-chip experiments was 335 ± 65 μM, and the turnover number, k_{cat}, was 39 ± 5/s. The values of K_m and k_{cat} obtained from our conventional off-chip experiments were 336 ± 75 μM for K_m and 49 ± 9/s for k_{cat}. We compared the on-chip results to the off-chip results and found that the deviation was less than 0.3% for K_m and 20.4% for k_{cat}. Since we carry out the experiments with an enzyme that is a biological sample having variable properties, those deviations can never be entirely eliminated.{Cornish-Bowden, 1995 #61} When we consider these points, the deviations between our on-chip and off-chip experiments were small enough to show the consistency in our experiments. Those small deviations were the most important evidence to verify that the presented microfluidic device can be used

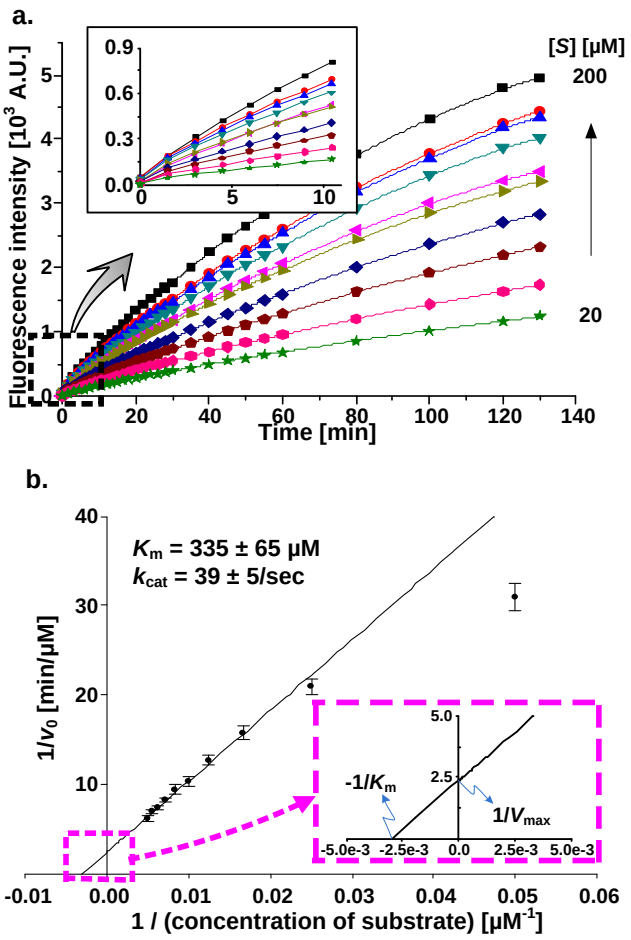

Figure 3.4 | Parallel reactions with a series of substrate concentrations from 20 μM to 200 μM with an increment of 20 μM. (a) Fluorescent intensity of the product according to the increase of the substrate concentration of β-galactosidase. (b) Lineweaver-Burk reciprocal plot; K_m and k_{cat} were found to be 335 ± 65 μM and 39 ± 5/s, respectively.

to determine the enzyme kinetic parameters in a reliable manner. We also compared the previously reported off-chip results of 550 ± 200 μM for K_m and 70 ± 30/s for k_{cat} and on-chip results of 450 ± 200 μM for K_m and 54 ± 20/s for k_{cat} {Hadd, 1997 #148}to our on-chip results. We then found the deviations between our result and the reported values of K_m and k_{cat}: 25.5% and 27.8% for the on-chip experiment and 39% and 30% for the off-

chip experiment, respectively. The deviation of our results and the published results mentioned above may be attributed to the use of different substrate and the different measurement method. We used the same substrate of resorufin-β-D-galactopyranoside for on-chip and off-chip experiments. However, Hadd *et al.* {Hadd, 1997 #148} adopted different substrate of o-nitrophenyl-β-D-galactopyranoside for their off-chip experiments. Their K_m and k_{cat} values of conventional experiments were derived from absorbance based measurements. In our case, we used the same substrate, resorufin-β-D-galactopyranoside and the fluorescence based measurement method, for both on-chip and off-chip experiments resulting in less than 0.3 and 20.4 percent deviations in K_m and k_{cat} respectively. The difference in the results also might be due to our inclusion 0.1% of BSA and 0.05% Tween 20 in the buffer system. However, the values from our experiment and the literature are valid because our results were located in the range of the standard deviations of the reported results. Practically, several factors, such as weighing, degree of freedom, etc., in the course of statistical analysis influenced the resultant values of the kinetic parameters. For example, when a researcher analyzed identical data sets with different weighing methods, the deviations of 13% for K_m and 24% for k_{cat} were reported.{Wilkinson, 1961 #62;Cornish-Bowden, 1995 #61} Unfortunately, because most researchers did not report on the detailed parameters used in the statistical analysis, it is not easy to quantitatively compare the results obtained from different groups. Through the presented research, we proved the reliability and versatility of our microfluidic system. Therefore, we believe this system could be used to determine the kinetic parameters of newly discovered enzymes and to evaluate the potency of inhibitor.

Effects of inhibitors

The response of the enzyme activity to total inhibitor concentration, [*I*], is important for understanding the regulation mechanism.{Segel, 1993 #59;Copeland, 2005 #60} We evaluated the effect of [*I*] on v_0 with a single experiment on a chip. For this experiment, we used phenylethyl *β*-D-thiogalactoside (PETG) and lactose as competitive inhibitors of *β*-galactosidase. To produce a series of reaction conditions,

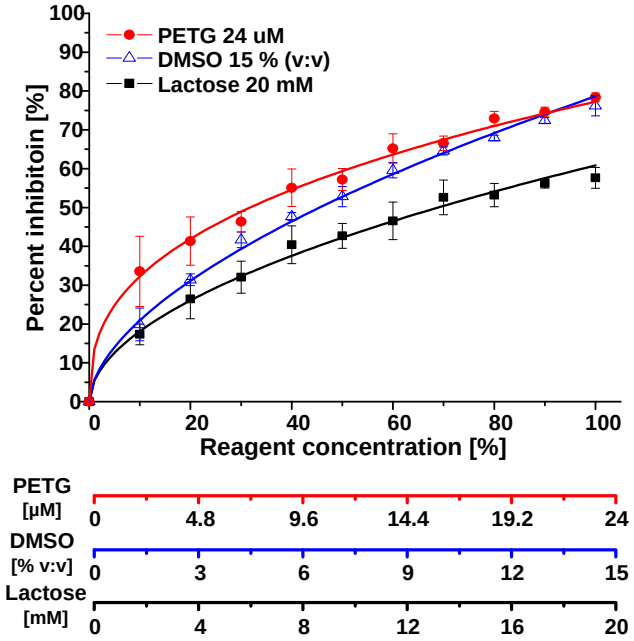

Figure 3.5 | Effect of the inhibitor concentration on enzyme activity. 0~24 μM of PETG, 20 mM of lactose, and 0 ~ 15% of DMSO (v:v) were used. For this reaction, a constant concentration of the substrate and the enzyme, 133 μM of resorufin-β-D-galactopyranoside and 83.7 μg/L of β-galactosidase, was used.

we introduced 40 μM of PETG and 33.3 mM of lactose in assay buffer containing 139.5 μg/L of *β*-galactosidase into reagent inlet port 1 and introduced assay buffer containing 139.5 μg/L of *β*-galactosidase into reagent inlet port 2. We introduced 333

μM of substrate into reagent inlet port 3 to supply a constant concentration of substrate. The resultant concentration ranges of the inhibitors were 2.4 μM to 24 μM for PETG and 2 mM to 20 mM for lactose. We used the enzyme concentration (83.7 μg/L) and the substrate concentration (133.3 μM) as the final concentrations for the experiments. **Figure 3.5** shows the variations in enzyme activity as the inhibitor concentrations increased. We determined the inhibitor concentration showed 50% inhibition, IC_{50}, for each inhibitor. We obtained half-maximal inhibitory concentrations of PETG and lactose through fitting the concentration response by using modified Michaelis-Menten equations (1). The IC_{50} of PETG and lactose obtained from our on-chip experiment was 10 ± 1.3 μM and 5.3 ± 0.7 mM, respectively. These values compared well with the value of 7.2 μM and 4.2 mM reported in literature, which were determined by using a simple channel network and an electrokinetic flow as a driving force.{Hadd, 1997 #46} DMSO is a common solvent used to prepare a concentrated stock solution for high concentrations of inhibitors and substrates. DMSO, however, reduces enzyme stability in high concentrations and decreases the reaction rate.{Copeland, 2005 #60} Hence, we evaluated the effect of DMSO on enzyme activity. For this, a concentration gradient of DMSO ranging from 1.5% to 15% (v:v) in enzyme reaction mixture was formed on a chip. We confirmed that 6 ± 0.6% (v:v) of DMSO reduced 50% of enzyme activity from the concentration response curve.

3.5 Conclusions

We have demonstrated that enzyme kinetic parameters can be obtained by using a microfluidic system that has eleven parallel multi-step processors. Each processor has

individual metering, mixing, and incubating components. We used nanoliters of β-galactosidase and its substrate, resorufin-β-D-galactopyranoside, as the model system for enzyme-catalyzed reactions. By changing the reactant concentrations, we observed the change in the reaction rates and determined the key parameters for the enzyme kinetics, K_m and k_{cat}. There are several potential uses for the presented microfluidic system. The chip could be useful for fast and accurate evaluation of the effects of pH, cofactors, ionic strengths, and ratio of reactants on reactions, etc. The present system could also be applied in enzyme engineering to develop engineered biocatalysts. In addition, by combining several detection techniques, such as electrochemical methods,{Garcia, 2003 #63} UV/Vis spectrometry,{Salimi-Moosavi, 2000 #64} or mass spectrometry,{Schilling, 2004 #65} for on-chip quantitative monitoring, we could increase the sample-in and answer-out capability of the microfluidic system to determine the reaction kinetics with various chemical samples, including non-fluorogenic substrates. The microfluidic system is a useful tool in revealing reaction kinetics and can be applied to many screening processes in biotechnology and other "omic" disciplines.

Chapter 4

EVALUATION OF DOSE RESPONSE FROM LOG-SCALE CONCENTRATION GRADIENTS

4.1 Introduction

In the process of drug discovery, quantitative characterization of inhibitory potencies of all the potential drug candidates is necessary to figure out the best candidate{Copeland, 2005 #66}. For comparing potential drug candidates an outcome of curvefitting of a sigmoidal curve to the dose response data or the value of half maximal inhibitory concentration, IC_{50} is used{Motulsky, 2004 #43;Copeland, 2003 #67;Motulsky, 2004 #43;Cortes, 2001 #68}. Inhibitors are small molecular weight molecules that impede the substrate molecules from reaching or binding to the enzyme active sites{Copeland, 2000 #35} and half of today's drugs are inhibitors{Copeland, 2005 #66}. In dose response analysis the use of a wide concentration range is important because the dose response is represented by a Malthusian-type differential equation whose solution is logarithmic type{Rozman, 1996 #69}. Recently, the importance of a log scale for drug response analysis, based on thermodynamical basis, has been reiterated {Waddell, 2008 #70}. The drug response is directly proportional to the log of the drug concentration expressed as $\mu = RT\ln[a]$ {Atkins, 2009 #71}, where μ is chemical potential or response of the drug and 'a' is activity or concentration of the drug. Hence, care has to be taken to select drug concentrations that are equally spaced using a logarithmic scale instead of a linear scale.

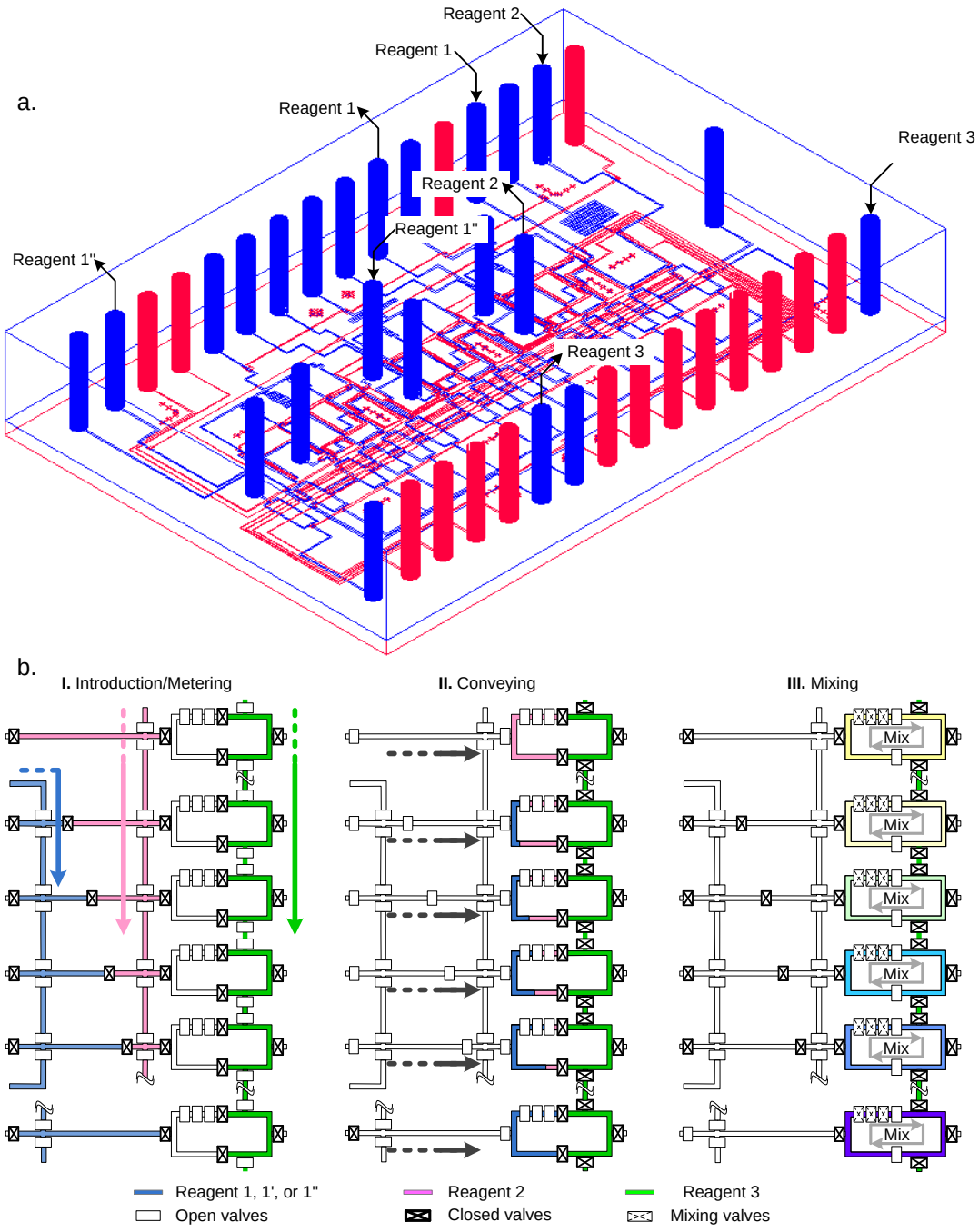

Figure 4.1 | (a) design of the microfluidic device. (b) step-by-step working of the device.

4.2 Objetive

We present a new approach for dose response analysis of enzyme inhibitors by using an integrated microfluidic system that has the capability of realizing a wide range

of accurate dilutions in a logarithmic way through semi-direct dilution of samples inside a chip. To demonstrate the function of the present system, we measured dose response curves and determined IC_{50} values of three inhibitors, marimastat, batimastat and CP471474 for matrix metalloproteases-9 (MMP-9) and MMP substrate III by conducting a series of dose response reactions in logarithmic concentration gradients with nanoliters of drug or inhibitor samples.

4.3 Materials and Methods

Materials

The substrate QXL^{TM}520-Pro-Leu-Gly-Cys-(Me)-His-Ala-D-Arg-Lys-(5-carboxy-fluorescein)-NH_2 (AnaSpec Inc.), internally quenched peptide matrix of matrix metalloproteinases-9 (MMP-9) was used for the enzyme reaction. This substrate releases fluorescent signals through dissociation of the quencher (QXLTM520) and carboxyfluorescein (FAM), fluorophore, via proteolytic cleavage by enzymatic reaction. MMP-9 is known to directly or indirectly influences human diseases, such as infiltration and metastasis of cancer cell, arthritis, etc., hence, MMP-9 is one of the major targets for development of anticancer drugs{Hooper, 1996 #82;Baguley, 2002 #83}. For establishing a standard curve, we used reference dye, FAM-Pro-Leu-OH. The excitation and emission wavelengths for FAM are 480 nm and 520 nm, respectively. According to the enzyme reaction types, 50nM, 10 nM, and 5 nM of MMP-9 were separately dissolved into the reaction buffer (TCNBT; 50 mM Tris, 10 mM $CaCl_2$, 150 mM NaCl, 0.05% Brij-35, 0.05 % Tween-20 and 0.1% BSA at pH 7.5). For the substrate of MMP, a stock solution was prepared as 100 μM in TCNBT buffer. Inhibitors of MMP-9, marimastat and batimastat (Tocric bioscience), were dissolved into DMSO in 10 mM of stock

solution. Prepared reagents were stored at -20 °C until dilution with TCNBT buffer for experiment.

Device operation

As shown in **Figure 4.1a** and **Figure B1** in the Appendix B, 3 gradient formers (GF) with 14 parallel processes are on a single chip. Each GF is composed of 4 microfluidic processors, respectively. Two extra processors are added for a positive control and a negative control on the present chip. A step-by-step operation of the device is depicted in **Figure 4.1b**. The step-by-step operation includes loading and metering of the reagents (substrate, buffer, inhibitor, and an enzyme), mixing of the metered reagents, and the scanning of the reactions. We introduced reagent 1 (substrate, FAM, or inhibitor) and 2 (dilution buffer) into their respective inlet channels by applying the pressure from nitrogen gas. The inlet channels were connected to the metering channel for generating the concentration gradients. The third reagent, in this case enzyme, was filled into the enzyme part of the mixer through the reagent 3 inlet channel. The metered reagents 1 and 2 are introduced into the mixer. Now, we have all the three reagents, dilution buffer, substrate, and the enzyme solution in the mixer together. In this step, the two reagents were separated from the third reagent in the microreactors by two separation valves to avoid undesirable initiation of the enzyme reactions. We closed all the separation valves around the microreactor and then opened the two separation valves between the enzyme solution (right side) and the diluted substrate (left side). The three reagents were mixed in the microreactor with sequential operation of the microvalves for peristalsis.

Image Acquisition and Data Processing

We used a modified biochip scanner (arrayWoRx, Applied Precision, WA) to acquire the images of the on-chip dose response reaction. We conducted multiple scans of the part of the chip during the progress of the enzyme reactions. All the acquired images were 16-bit grayscale, the resolution was 7 800 pixels per inch (PPI), and the pixel size was 3.25 μm. To reduce scanning time and ensure enough chip areas for data acquisition, we scanned a partial region of the 14 microreactors (30.5 mm × 1.5 mm) as shown in **Figure 4.2**, bottom. Image acquisition software (arrayWoRx 2.5 Software Suit, Applied Precision, WA) generated the integrated scan image. The total scanning time of the integrated image (30.5 mm × 1.5 mm) was approximately 45 s. Time series analyzer module of ImageJ software (http://rsb.info.nih.gov/ij/) was used to analyze and digitize all the fluorescence images. We measured the changes in the fluorescent intensity over multiple scanning processes for evaluating the photobleaching rate of FAM on the chip and corrected the digitized data. The loss of fluorescent intensities was compensated by using a similar method used for the photobleaching effect on a multiple scanned confocal image{Jambovane, 2009 #11}.

Statistical analysis

To determine the kinetic parameters, K_M and k_{cat}, the initial velocities of the individual reactions were curve-fitted with the Michaelis-Menten equation{Copeland, 2000 #35} using the enzyme kinetics module of Sigmaplot software (Systat software Inc.). For IC_{50} values, with standard error and 95% confidence interval, we curve-fitted the four parameter nonlinear-logistic-regression model available to the inhibition data. The four parameter model is of the form{Motulsky, 2004 #43} as shown below.

$$\%I = \%I_{\min} + \frac{\%I_{\max} - \%I_{\min}}{1 + 10^{\left(Log\left(IC_{50}\right) - [I]\right) \cdot h}} \quad (4.1)$$

Where, IC_{50} refers to median point of the concentration-response plot; [I] represents the concentration of inhibitor; h is the Hill coefficient or Hill slope, which means the steepness of dose-response plot; %I designates percentage inhibiting potency, including minimum and maximum.

4.4 Results and Discussion

Logarithmic gradient formation

In the present device, each GF has two separate inlets for inhibitor (reagent 1) and buffer (reagent 2). The three identical GFs allow conducting three repetitive experiments with fixed concentration range if we feed an inhibitor and reagent with the same concentrations. For example, if we introduce 10× inhibitor (reagent 1) and 1× working buffer (reagent 2), we can create final inhibitor concentrations of 1×, 2.5×, 5× and 7.5×. We can also derive a wider concentration range from the device by feeding different concentrations of inhibitor (reagent 1) in the three GFs, and by keeping the same concentration of working buffer. If we feed 10× inhibitor to the first GF1, 100× to the GF2, then 1000× to the GF3, the effective concentrations in each GF will respectively be 1, 2.5, 5, 7.5×, for GF1; 10, 25, 50, 75×, for GF2; 100, 250, 500, 750×, for GF3. Here the negative and positive control processors generate 0 and 1000× concentrations. Therefore, by introducing the three concentrations of inhibitor and buffer, meaningful logarithmic concentrations for dose response are generated such as 0, 1, 2.5, 5, 7.5, 10, 25, 50, 75, 100, 250, 500, 750 and 1000× by the present device in semi-direct dilution. However, the concentration range could easily be increased by changing the input concentration of inhibitor while keeping

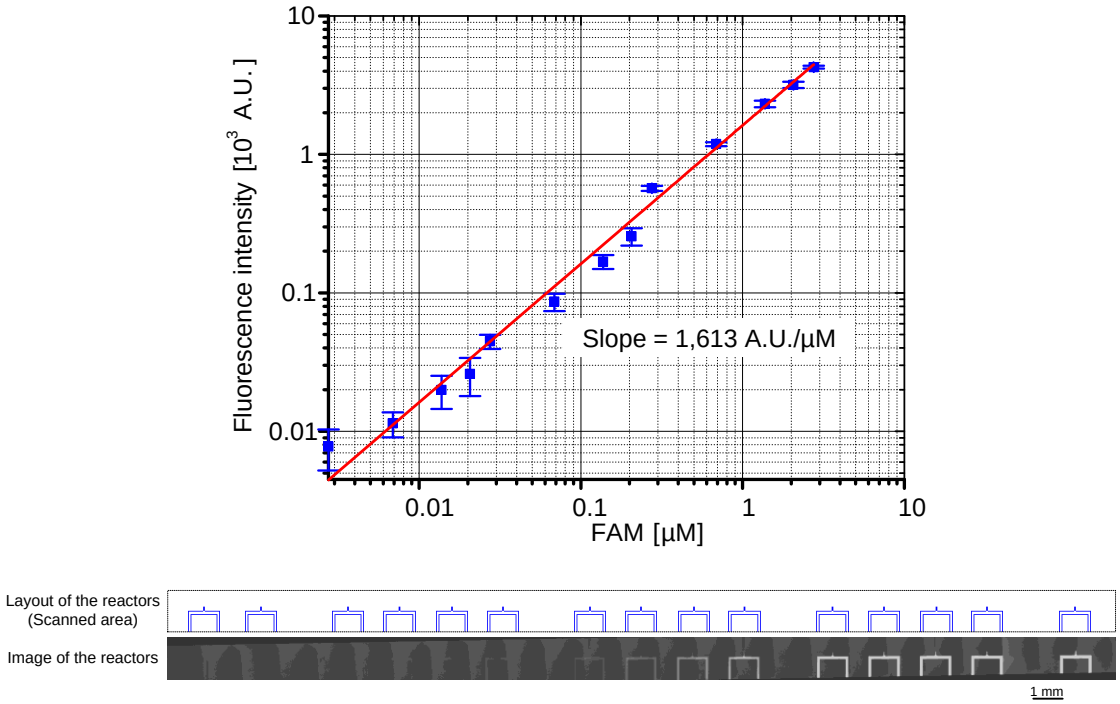

Figure 4.2 | Log-log scale standard curve for FAM with the scanned image of FAM concentration gradients.

buffer the same. In our experiments we have created a concentration range from 1× to 4000× by using 10×, 200× and 4000× of inhibitors for the three GFs. Note that the individual microfluidic processors has nano-liters scale volume. Hence large amount of samples could be saved during dose response analysis in comparison to the large amount of reagent volumes used in conventional methods{Olechno, 2006 #87;Harris, 2010 #88;Quintero, 2007 #78;Hüser, 2006 #73;Lee, 2010 #89;Lee, 2010 #89}.

To confirm the generation of a logarithmic gradient using present microfluidic chip, we generated the concentration gradient of carboxyfluorescein (FAM) in the ratio of 1:1,000. To generate this concentration gradient, we introduced FAM with three concentrations, 0.05 μM, 0.5 μM, and 5 μM, into the reagent input

Table 4.1 | Compositions and concentrations of reagents introduced into an integrated microfluidic chip to produce a logarithmic gradient.

	GFs	Reagents introduced into metering channels		Constant reagent	Final concentrations of metered reagents			Relative concentration ranges[b]
		Reagent 1	Reagent 2	Reagent 3				
[FAM] gradient [nM]	GF1	5000	buffer	buffer	2,500.00	~	250.0	1 - 1,000
	GF2	500			187.50	~	25.00	
	GF3	50			18.75	~	2.50	
[E] gradient [nM]	GF1	20.0		50 μM substrate in buffer	10.00	~	1.00	1 - 100
	GF2	2.0			0.75	~	0.1	
	GF3	buffer				0		
[S] gradient [μM]	GF1	100.0		5 nM MMP-9 in buffer	50.00	~	5.00	
	GF2	10.0			3.75	~	0.50	
	GF3	buffer				0		
[Marima-stat] [nM]	GF1	500.00[a]	44.3 μM substrate in buffer	10 nM MMP-9 in buffer	250	~	25	1 - 4,000
	GF2	25.00[a]			9.375	~	1.250	
	GF3	1.25[a]			0.469	~	0.063	
[CP 417474] [nM]	GF1	2,000.00[a]			1,000	~	100	
	GF2	100.00[a]			37.5	~	5	
	GF3	5.00[a]			1.875	~	0.25	
[Batimas-tat] [nM]	GF1	500.00[a]			250	~	25	
	GF2	25.00[a]			9.375	~	1.250	
	GF3	1.25[a]			0.469	~	0.063	

[a]Inhibitor solutions included 44.3 μM substrate

Ranges and concentrations were calculated with 13 microfluidic processors excluding a negative control

ports of GF1, GF2, and GF3, respectively. The reaction buffer with a fixed concentration was also introduced to dilution buffer input ports of GF1, GF2 and GF3 (**Figure 4.1** and **Figure B1** in the Appendix B). Therefore, a concentration gradient range of 0.0025 μM to 2.5 μM was generated in the 13 microfluidic processors. **Figure 4.2** shows the standard curve for FAM established from 3 independent experiments conducted with logarithmic gradients on a chip. In the standard curve, we observed a linear relationship, with a slope of 1,631 AU/μM, between concentration of FAM and the corresponding fluorescence intensity.

Determination of kinetic parameters of enzyme reactions

The half maximal inhibitory concentration, IC_{50} can be influenced by analysis conditions, such as pH, ionic strength, substrate concentration, etc.{Copeland, 2005 #66}. Among these factors the most dominant factor influencing IC_{50} value is the $[S]/K_M$ ratio{Copeland, 2003 #67}. For the determination of IC_{50} value from a logistic-dose response curve the selection of substrate concentration equal to the value of K_M is recommended{Copeland, 2005 #66}. Therefore, we first determined the K_M value for matrix metalloproteinase-9 (MMP-9) before measurement of the inhibiting potency of the inhibitors.

For the determination of reliable values of IC_{50} and K_M, selecting the concentration of enzyme that shows linear reaction progress is critical. To decide the enzyme concentration only part of the microfluidic chip was used. We introduced enzyme solutions of 2 nM and 20 nM to GF1 and GF2 to form an enzyme concentration gradient in the range of 0.1 nM ~ 10 nM (1:100) (**Figure B2b** in the Appendix B). (We did not use the group GF3 because concentration of enzyme over 10 nM was not

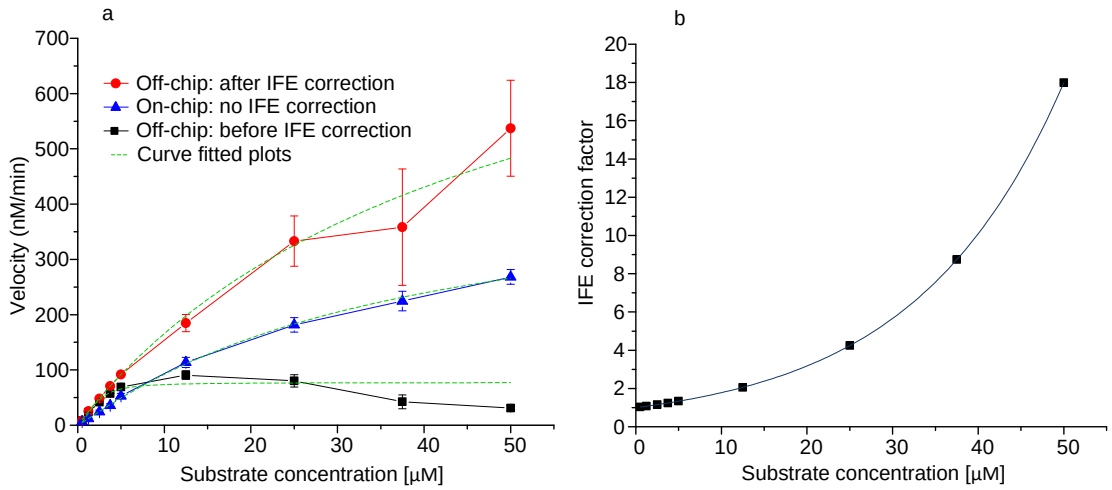

Figure 4.3 | Determination of enzyme kinetic parameters, K_M and k_{cat}. (a) comparison of on-chip and off-chip results indicates no need of inner filter effect correction factor for on-chip data. The off-chip velocities, after applying correction factor, shows marked improvement in the velocities at each substrate concentration. The error bar is obtained from three individual experiments. The exponential nature of corrector factor increases the magnitude of error bar, especially at higher substrate concentrations in corrected off-chip velocity data. (b) the inner filter effect correction factor increases exponentially with substrate concentration.

required.) When 50 μM of MMP substrate III was used, it was observed that even with a measuring time of 120 minutes, the kinetic reaction did not reach the plateau for enzyme concentrations as high as 10 nM (**Figure B3a** in the Appendix B). Therefore, 10 nM of enzyme concentration was chosen to determine reaction velocities for further kinetic analysis.

To determine the kinetic parameters, K_M and k_{cat}, of MMP-9, we introduced 100 μM substrate for GF1 and 10 μM for GF2, respectively, along with the dilution buffer and 20 nM MMP-9 enzyme (**Figure B2c** in the Appendix B). We did not use the GF3 for

generating concentration gradient. As a result, 1 μM ~ 100 μM (1:100) of substrate concentration gradient was formed on the chip in the metering channels. After mixing the metered substrate and enzyme into the reactor mixer, the substrate concentration gradient becomes 0.5 μM ~ 50 μM in 9 processors (GF1, GF2 and positive control). **Figure B3b** in the Supporting Information shows the results of 9 independent reactions. From this plot, it is observed that the rate of reaction increased with the increase of substrate concentration. The reaction rates were linear up to 10 min (see **Figure B3b**, box in the Appendix B). Therefore, the initial reaction velocity was calculated from these linear parts of the progress curves. A Michaelis–Menten plot was prepared from the initial velocity data of three repetitive experiments (**Figure 4.3a**). Applying nonlinear curve-fitting to the plot, we determined K_M and k_{cat} from the on-chip experiments and the respective values were 53.4 ± 5.2 μM and 55.8 ± 4.1 /min.

For comparison, we conducted three off-chip experiments and the values of K_M and k_{cat} are 41.2 ± 4.7 μM and 84.9 ± 0.9/min. The deviation between on-chip and off-chip K_M values was 25.8 % whereas k_{cat} was 41.3 %. This discrepancy could be attributed to the characteristics of fluorescence detection that is relevant especially at higher substrate concentration with large optical path length {Lakowicz, 2006 #90;Copeland, 2000 #35;MacDonald, 1997 #91;Liu, 1999 #92;Kubista, 1994 #93;Fanget, 2003 #94}. Unlike absorbance based measurement the fluorescence detection experiences significant loss of fluorescence intensity at higher substrate concentrations, known as the inner filter effect (IFE){Copeland, 2000 #35;Lakowicz, 2008 #95}. The correction factors are used to compensate for the loss of florescence intensity.

Effect of Inner filter effect correction factor on K_M and k_{cat}

However, the correction factors exponentially increase with the increase of substrate concentrations {Gu, 2008 #96;MacDonald, 1997 #91;Kubista, 1994 #97}. On the other hand, in our on chip experiments, we observed negligible saturation of fluorescence intensity under the same substrate concentration range (**Figure 4.3a**). We assume that these differences are due to different length of optical path for on-chip, ~ 10 μm, and off-chip, ~ 5 mm, experiments. In addition to the fact that an enzyme is an biological sample with variable properties{Cornish-Bowden, 1995 #7}. In the case dilute solution or clean water the ideal fluorescence intensity, F_{ideal} at the excitation wavelength, λ_{ex} and emission wavelength, λ_{em} is given as{MacDonald, 1997 #91},

$$F_{ideal}(\lambda_{ex},\lambda_{em}) = k(\lambda_{ex},\lambda_{em})\cdot\Phi(\lambda_{em})\cdot I_0(\lambda_{ex})\cdot 2.3\cdot\varepsilon(\lambda_{ex},\lambda_{em})\cdot\Delta x\cdot c \qquad (4.2)$$

Where, $k(\lambda_{ex},\lambda_{em})$ is an instrument constant, function of λ_{ex} and λ_{em}, depicting geometric and optical factors; $\Phi(\lambda_{em})$ is quantum yield of fluorescence; $I_0(\lambda_{ex})$ is the intensity of incident beam reaching the sample; $\varepsilon(\lambda_{ex})$ is extinction coefficient of fluorophore at λ_{ex}; Δx is the path length traveled by the excitation beam; and c is the concentration of fluorophore sample under investigation.

However, this ideal condition never exists in practice. The sample always absorbs some light, both at λ_{ex} and λ_{em}, and reduces the fluorescence intensity. So the relationship between fluorescence intensity and concentration of sample becomes nonlinear. This effect is called as inner filter effect{Lakowicz, 2008 #95}. Absorption of light at λ_{ex} is known as primary inner filter effect (pIFE) while absorption at λ_{em} is called as secondary

inner filter effect (sIFE){Fanget, 2003 #94}. Out of these two, sIFE could never be avoided because fluorophore molecules need to absorb some light for their excitation. This absorption becomes significant at higher concentration of substrates making the determination kinetic parameters difficult.

To overcome the impact of inner filter effect, many scientists use the following correction factors. Hence the observed fluorescence intensity can be converted to ideal fluorescence value by applying the correction factors{Christmann, 1981 #3;Fanget, 2003 #94}.

$$F_{ideal}\left(\lambda_{ex},\lambda_{em}\right)=F_{observed}\left(\lambda_{ex},\lambda_{ex}\right)\cdot C_P^{ex}\left(\lambda_{ex}\right)\cdot C_S^{em}\left(\lambda_{em}\right) \tag{4.3}$$

Where $C_P^{ex}\left(\lambda_{ex}\right)$ represents the correction factor for pIFE and $C_S^{ex}\left(\lambda_{ex}\right)$ is for sIFE and combined correction factor becomes{Christmann, 1981 #2;, 2006 #3}

$$C_P^{ex}\left(\lambda_{ex}\right)\cdot C_P^{em}\left(\lambda_{em}\right)=10^{\left(\varepsilon\left(\lambda_{ex}\right)+\varepsilon\left(\lambda_{em}\right)\right)\cdot c\cdot\Delta x} \tag{4.4}$$

From equation (4.4), it can be concluded that this is the oversimplified version of the original equation (4.2). Here the correction factor cannot completely compensate for the inner filter effect. The effect of these correction factors are more pronounced at higher concentrations (**Figure 4.3b**). Therefore, for the determination of kinetic parameters the curvefitting of Michelis-Menten equation to $C_P^{ex}\left(\lambda_{ex}\right)\cdot C_S^{em}\left(\lambda_{em}\right)$ corrected data becomes incorrect. In the case of our on-chip experiments the inner filter effect is negligible due to nanoliter scale sample volume with very small path length, Δx ~10 μm of the microchannel. In between, conventional off-chip experiments for our comparative experiments we had to use a fluorophotometer with a cuvette that has ~5 mm of optical path length. Therefore, the deviations of our on-chip values of K_M and k_{cat} compared to our off-chip experiments are unavoidable. This has been confirmed with our on-chip and

off-chip velocity data. In our on-chip velocity values did not reach the plateau region till 50 μM of substrate concentration. However, the off-chip data showed reduced velocity trend after 7.5 μM. Because of which we could not determine the kinetic parameters from our off-chip velocity plot due to reduced velocity trend. To overcome this reduced velocity trend of off-chip experiments, we applied inner filter effect. Although after the use of inner filter effect correction, the values off-chip velocities increased making it suitable for the determination of kinetic parameters, this correction process, however, lead to the upto 41.3% deviations (as explained in the previous section) in the off-chip kinetic parameters.

Assessment of inhibition potencies

To show the ability of our device to generate a logarithmic concentration gradient and the functionality of our device to conduct logistic dose response studies, we determined the IC_{50} values of three inhibitors, marimastat, batimastat and CP417474, of the MMP-9 enzyme from their corresponding logistic dose response plots. An inhibitor concentration range of 0.063 nM ~ 250 nM (1:4000) was created on the chip in the 14 reactors. Note that, all the 14 reactors were used considering the requirement of a wider concentration range of inhibitors (**Figure 4.1** and **Figures B1** and **B2** in the Appendix B); 22.15 μM of substrate and 5 nM of enzyme was used, respectively. **Figure 4.4** shows dose response plots for the 3 inhibitors, marimastat, batimastat and CP417474. From these plots, the IC_{50} values for marimastat, batimastat and CP417474 are 3.2 ± 0.2 nM, 4.1 ± 0.2 nM and 11.9 ± 1.0 nM, respectively. The respective IC_{50} values from our off-chip experiment are 3.1 ± 0.1 nM (marimastat), 3.5 ± 0.3 nM (batimasat) and 14.9 ± 0.9 nM (CP417474). From the literature, the reported IC_{50} values for marimastat and

batimastat are 3 nM{Brown, 2000 #98;Rao, 2005 #99} and 3-4 nM{Asahi, 2000 #100;Rasmussen, 1997 #101} respectively. Through the comparison of the results from on-chip experiment and off-chip experiment,

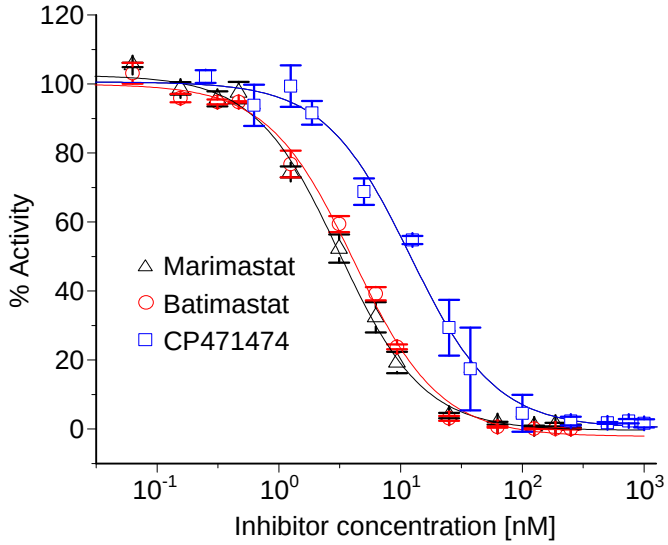

Figure 4.4 | The logistics dose response plots for three inhibitors, marimastat, batimastat and CP471474, of MMP-9 enzyme. The dose-response plot for each inhibitor was obtained from three on-chip experiments. The IC_{50} values for each inhibitor were calculated by curvefitting the four parameter model to the inhibitory activity data.

we observed the deviation of 3.2 %, 17 % and 20 % in the IC_{50} values of marimastat, batimastat, and CP417474 inhibiters, respectively. These deviations in the values of IC_{50} are acceptable, considering enzyme as a biological sample with variable properties{Cornish-Bowden, 1995 #7;Cornish-Bowden, 1995 #7;Cornish-Bowden, 1995 #7;Cornish-Bowden, 1995 #7;Cornish-Bowden, 1995 #7;Cornish-Bowden, 1995 #7;Cornish-Bowden, 1995 #7}. Therefore, the present microfluidic chip can provide reliable determination of IC_{50} values of inhibitors with the automation of sample preparation, gradient generation, mixing, incubation and optical

detection. The present device can be used for the concentration-response analysis of reagents where a logarithmic scale concentration gradient is required. Our device could be used for various applications where log-scale gradient with flexibility of concentration range is required. The present system for example could be used for the evaluation of EC_{50}, LD_{50} and LC_{50} by using microbial cells or animal cells or for conducting cell cytotoxicity assays. These dose-response or cytotoxicity experiments could be conducted by feeding the cells to the constant volume part of the mixer and forming the gradient of inhibitors or reagent, for which the toxicity limit is to be determined, in group of reactors.

4.5 Conclusion

In summary, we demonstrated a new approach of logarithmic concentration gradient generation with an integrated microfluidic chip that has semi-direct dilution capability of reagents in addition to metering and mixing of reagents with 14 parallel microprocessors. We showed that the concentration range from 1:0 to 1:4000 of two reagents is easily realized on the present system. We successfully determined IC_{50} values of three inhibitors of marimastat, batimastat and CP417474 for MMP-9 enzyme from the corresponding logistic dose response plots of each inhibitor with a single on chip experiment. We also confirmed that with our present system we successfully avoided inner filter effect that is common with high substrate concentrations with conventional cuvettes. We believe that the new device would be a useful tool for pharmaceutical sciences especially for the evaluation of IC_{50} of various compounds through systematic handling of reagents in nanoliter scale.

Chapter 5

DEVELOPMENT AND MODELING OF DROPLET SYSTEM FOR FLEXIBLE CONCENTRATION GRADIENT

5.1 Introduction

Micro- or nanometer-sized droplets have come into the spotlight due to their great potential to provide new breakthroughs for scientists in the field of nanoparticle synthesis, diagnostic testing, and parallel reaction control{Hung, 2007 #102;Dendukuri, 2006 #103;Huebner, 2008 #104}. Since the droplet interface acts as a membrane confining the contents, droplets can work as microreactors, which are individually transported, mixed, and analyzed. Various reagents or cells can be put into the microreactors and, to satisfy diverse demand, flexibility in both the droplet size and the generation timing could be crucial for future droplet-based microfluidic systems.

5.2 Objective

In the present work, we depict the process of droplet formation through the mechanical cutting in a T-shaped microchannel. In addition, by using novel fluidic circuit based impedance method, we propose a predictive model for droplet size determination through an experimental parametric study by varying the flow channel height, the pressure driving liquids in the flow channel, and the viscosity of the dispensed phase. The droplet model could be used to predict droplet volumes required for the generation of concentration gradient for biochemical assays.

5.3 Materials and Methods

Chip design

Independent of the recent work of other research groups, we designed and fabricated a micro droplet generator chip that mechanically breaks off the dispensed phase into droplets in a microchannel T-junction (**Figure 5.1a)**

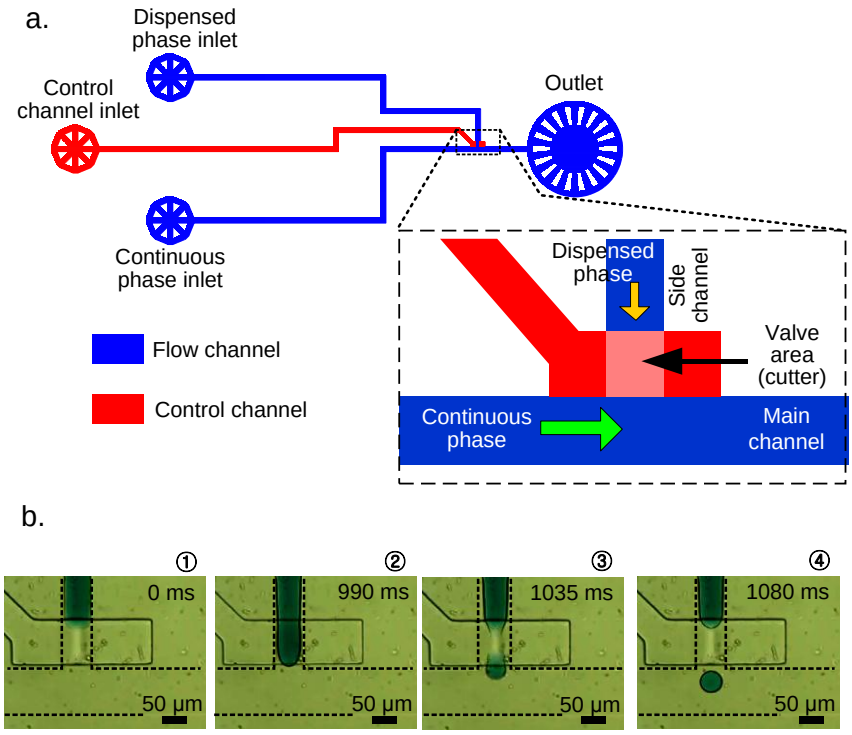

Figure 5.1 | (a) layout of microfluidic chip, (b) working principle and demonstration of micro droplet generation through mechanical cutting in microchannel T-junction.

The chip is made of two layers: the top fluidic layer and the bottom control layer. The control channel passes underneath the side flow channel. The thin membrane between the control channel and the flow channel functions as a cutter. When the pressure in the control channel is increased, the membrane is deflected and cuts the dispensed phase into a droplet. When the pressure is released, the membrane is restored to its original shape

and the dispensed phase flow is resumed. **Table 5.1** shows the dimensions of the flow channels and the cutter and pressure. The chip was fabricated and tested a polydimethylsiloxane (PDMS) microfluidic chip based on multilayer soft lithography {Unger, 2000 #26}.

As shown in **Figure 5.1a**, main flow channel forms a T-junction with the other side flow channel. A continuous phase flows along the main channel and a dispensed phase flows into the main channel via the side channel. We controlled the dispensed phase flow by using a mechanical valve. We formed droplets by completely closing the side channel filled with the dispensed phase. With this method, we can finely tune the droplet size by adjusting the dispensing time of the valve. Moreover, we can control the droplet generation timing independently of the size control by regulating the opening timing of the mechanical valve.

Droplet measurement

We used an optical microscope (Zeiss Axiovert 40 CFL) to observe the droplet generation inside the microchannels and captured images by using a high speed digital camera (Vision Research Micro 4). We determined the droplet volume based on the planar dimensions of the droplet. The planar dimensions of the droplet can be obtained from the captured image showing the generated droplet. When the droplet diameter is larger than the flow channel height, the droplet was assumed to have elliptical and elongated shape, and the droplet volume was estimated by using the planar dimensions of the droplet and the channel height. Otherwise, the droplet was assumed to be spherical, and the droplet volume was calculated by using the droplet diameter and the volume formula for spheres (For details of droplet volume calculation refer Appendix C).

Chip operation

We applied pressure to the backside of the liquids to drive them inside the flow channel. We operated the cutter at 103.4 kPa. We filled the control channel connected to the cutter with water to avoid bubble formation inside the flow channel. The pneumatic control setup consisted of two sets of eight-channel manifolds (Fluidigm Corporation) controlled through a BOB3 control board (Fluidigm Corporation). A digital I/O card (National Instruments, PCI-6533) ,mounted in the computer, digitally controlled the switching of each channel of manifolds through the BOB3 control board. We used a custom-built LabVIEW (National Instruments) program for automatic control of the microfluidic chip.

Table 5.1 | Dimensions of microchannels and cutter valve, and the experimental condition.

	Width (μm)	***Length (mm)***	***Channel height (μm)***			***Flow driving pressure (kPa)***		
			1	**2**	**3**	**1**	**2**	**3**
Main channel	90.0	7.5	11.5	13.6	15.3	10.3	13.8	17.2
Side channel	50.0	7.5						
Cutter valve channel	50.0	90.0				103.4		

A 10.0% (v/v) pigment solution (ESCO Foods Inc.) and 0.1 and 0.5% (w/w) sodium alginate solutions were used for the dispensed phase. Mineral oil (Sigma) was used for

Table 5.2 | Viscosity of tested liquids.

	Dispensed phase			**Continuous phase**
	10% (v/v) pigment solution	0.1% (w/w) sodium alginate solution	0.5% (w/w) sodium alginate solution	
Viscosity (mPa-s)	1.00	3.27	10.14	32.80

the continuous phase. The viscosity of the tested liquids is listed in **Table 5.2**. It was measured with a viscometer (Galvanic Applied Science USA, Inc., VL200) at 21.6℃.

5.4 Results and Discussion

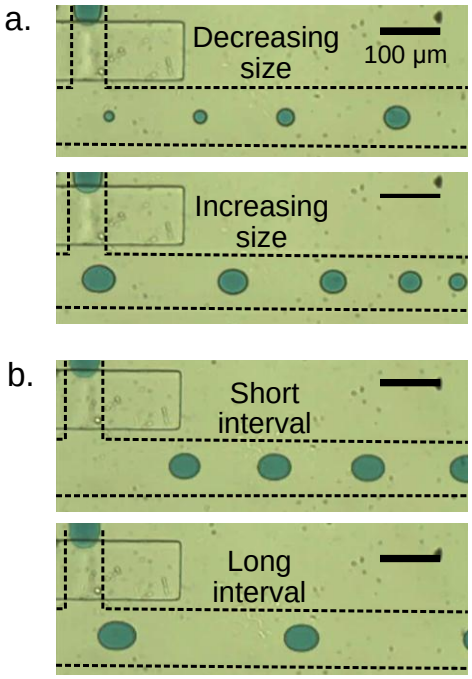

Figure 5.2 | Flexible micro droplet generation. (a) size control, (b) temporal control.

Flexibility of droplet generation

Figure 5.1b shows the droplet generation demonstrated by the tested microfluidic device. When the side channel is opened, the dispensed phase starts to flow into the main channel. As soon as the cutter is actuated to close the side channel, a neck of the dispensed phase is formed. As the neck becomes narrow, the interfacial tension force supporting the neck is decreased. Finally, when the cutter closes the side channel, the dispensed phase is cut and a droplet is formed. **Figure 5.2** shows examples of the flexible micro droplet generation. We consecutively decreased or increased the droplet size by changing the dispensing time continuously, and, for the same dispensing time, we varied the interval between droplet generations. We believe that the droplet generation method

presented here clearly shows the possibility of the generation and manipulation of droplets with great flexibility. When the dispensed phase is cut into droplets by the

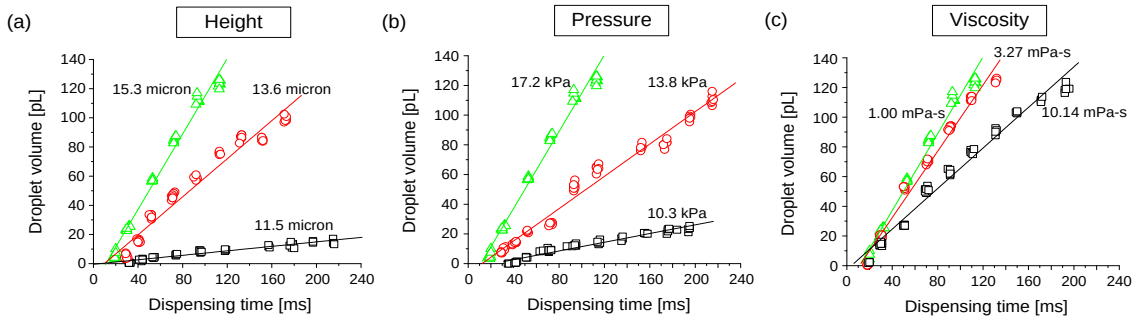

Figure 5.3 | Effect of (a) flow channel height, (b) pressure driving liquids in flow channel, and (c) dispensed phase viscosity on droplet size change according to dispensing time. Symbols are experimental data and solid lines represent curve fits.

continuous phase flow, the droplet size is determined by the balance between the drag force and the surface tension force. However, when the droplets are generated through mechanical cutting, droplets are formed as soon as the dispensed phase is mechanically cut by the membrane. For this case, droplet size is governed by the dispensing time and the flow rate of the dispensed phase.

Table 5.3 | Effect of dispensing time on droplet size (pressure: 103 kPa, channel height:15.3 μm).

Measured Valve open time (ms)	35	42	58	74	94	115	135	156
Average droplet diameter (μm)	3.0	11.5	22.6	26.0	28.8	30.1	31.6	33.9
Standard deviation (μm)	0.0	2.1	3.2	1.2	0.4	0.7	0.7	0.2
Average droplet volume (pL)	0.014	0.8	6.4	9.2	12.5	14.3	16.6	20.4

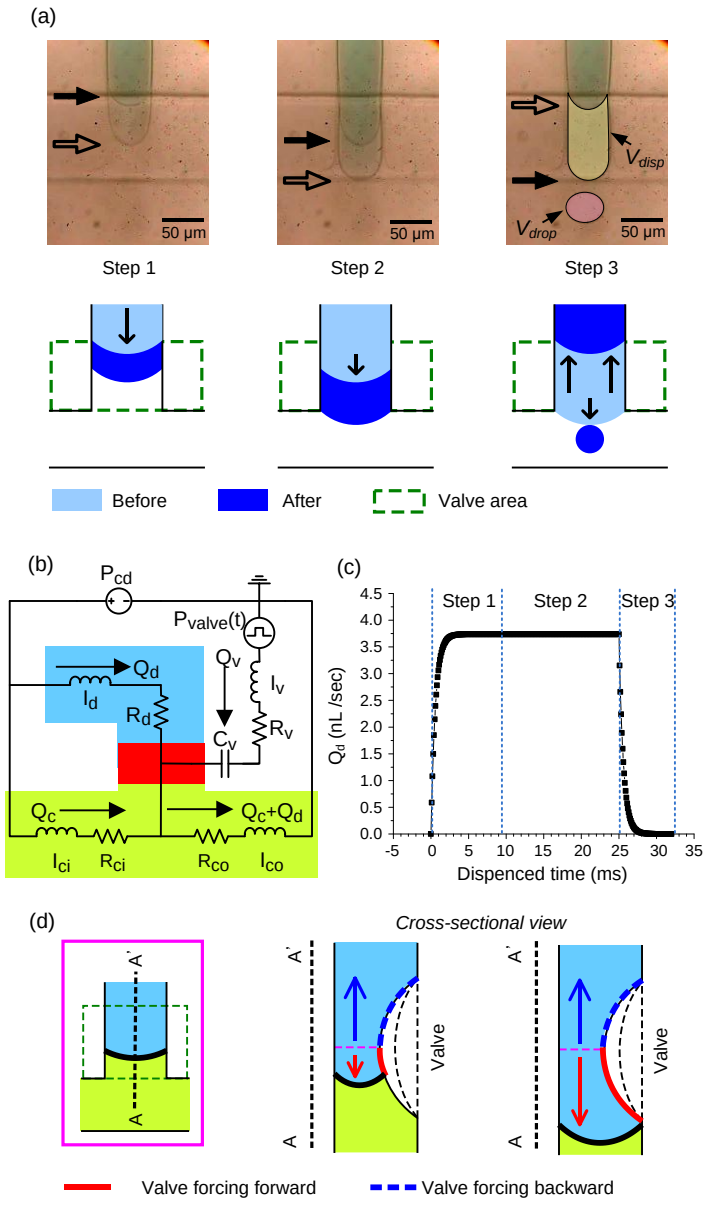

Figure 5.4 | (a) Droplet formation process, (b) fluidic circuit model of droplet formation, (c) predicted droplet formation cycle from fluidic circuit model and (d) dispensed phase back-flow.

We controlled the dispensing time by using a custom-built LabVIEW program. To control the flow rate of the dispensed phase, we varied the flow channel height, the pressure driving liquids in the flow channel, and the viscosity of the dispensed phase.

Figure 5.3 shows the droplet size change according to the dispensing time. The volume of the generated droplets ranges from 14 fL to 126 pL. The equivalent droplet diameter ranges from 3 μm to 62.2 μm. The droplet size increases as the dispensing time increases. For the same dispensing time, the droplet volume increases with the flow channel height increase, the pressure increase, and the dispensed phase viscosity decrease. This can be ascribed to an increase in the flow rate of the dispensed phase, which is closely related to the droplet growth. For large dispensing times (typically more than 50 ms), the droplet volume increases with the dispensing time almost linearly. On the other hand, for smaller dispensing times, the droplet volume increase according to the dispensing time increase decreases as the dispensing time increases. This atypical behavior of droplet generation, below the 40ms dispensing time, could be attributed to the poor mechanical response of the cutter (valve). And, when the dispensing time is less than about 20 ms, the droplet is not generated due to the limit in the mechanical response of the system to the electrical control signal. **Table 5.3** shows the effect of the dispensing time on the droplet size. The standard deviation is less than 4 μm of average value.

Fluidic circuit model

To clearly describe the droplet formation, we developed a descriptive model based on our observations, as shown in **Figure 5.4a**. There are three steps in droplet growth and detachment. During step 1, the side channel is opened, and the vacant space over the valve area is rapidly filled with the dispensed phase and the continuous phase. The flow rate of the dispensed phase decreases as the vacant space is filled with the immiscible fluids. When the dispensed phase comes in contact with the continuous phase, the flow rate of the dispensed phase reaches a steady state value. During step 2, the side

channel is kept opened, and the dispensed phase flows toward the main channel at a constant flow rate. During step 3, the valve closes the side channel. When the valve is activated, the dispensed phase above the valve area tends to flow backward and this reduces the final droplet volume. Finally, the valve cuts the dispensed phase into a droplet.

The volume dispensed during step 1 does not add to the droplet volume because the volume is pushed backward when the dispensed phase is cut by the cutter. Hence, the droplet volume is determined by the volume movement during steps 2 and 3. To estimate the dispensed volume during step 2, the flow rate of the dispensed phase should be obtained. To clarify important parameters affecting the flow rate of the dispensed phase, we modeled the flow channels as a network of flow impedance by using the analogy between the fluid flow and the flow of electricity (**Figure 5.4b**). The flow rate and the pressure drop across a flow channel are analogous to the electric current and the electric potential difference across an electric resistance, respectively. With descriptive circuit model we tried to predict the droplet formation cycle as shown in **Figure 5.4c.** The cycle could explain all the three steps described, as per the experimental observations, depicted in **Figure 5.4a**. Therefore it establishes the predictiveness of the circuit based model.

We solved the following three equations based on Kirchhoff's circuit laws to obtain the flow rate of the dispensed phase:

$$Q_c Z_{ci} - Q_d Z_d = 0 \tag{5.1}$$

$$Q_d Z_d + \left(Q_c + Q_d\right) Z_{co} = P_{cd} \tag{5.2}$$

$$Q_v Z_v + \left(Q_c + Q_d\right) Z_{co} = P_{valve}(t) \tag{5.3}$$

The solution to the simultaneous equations is as follows:

$$Q_d = \left[\frac{Z_{ci}}{Z_d Z_{ci} + Z_{co} Z_{ci} + Z_d Z_{co}} \right] P_{cd}$$

$$V_{disp} = Q_d \times t = \left[\left(\frac{Z_{ci}}{Z_d Z_{ci} + Z_{co} Z_{ci} + Z_d Z_{co}} \right) P_{cd} \right] \times t \qquad (5.4)$$

To check the validity of the theoretical model, we divided the dispensed volume by the simplified solution for the volume of the dispensed phase, equation 5.4, as shown in equation 5.5. **Figure 5.5a** shows that all the experimental data converges into a single curve, represented by equation 5.5, and this indicates that the theoretical model predicts the effect of parameters on the volume of the dispensed phase well.

$$\frac{V_{disp}}{V_{theo}} = \frac{V_{disp}}{\left[\left(\frac{Z_{ci}}{Z_d Z_{ci} + Z_{co} Z_{ci} + Z_d Z_{co}} \right) P_{cd} \right] \times t} = \left(0.19 + 0.84 \exp\left[\frac{-t}{119} \right] \right) \qquad (5.5)$$

Figure 5.4b shows that the back flow rate of the dispensed phase during step 3 is dominated by the dispensed phase volume dispensed during steps 1 and 2. The V_{disp} was measured from the captured image as shown in **Figure 5.4a**. As shown in the cross-sectional view, when the dispensed phase is dispensed a little beyond the centerline of the valve area, the dispensed phase is mainly forced backward because the valve area forcing backward is larger than that forcing forward. On the other hand, when the dispensed phase is dispensed sufficiently beyond the centerline, the dispensed phase above the valve area is forced bi-directionally and the ratio of volume moved backward is decreased. **Figure 5.5b** shows that the ratio of the dispensed phase volume moved backward can be curve fitted by equation 5.6.

$$\frac{V_{back}}{V_{disp}} = 0.16 + 1.91\exp\left(\left(-3.1\times10^{-2}\right)V_{disp}\right) \tag{5.6}$$

Where V_{back} represents the dispensed phase volume moved backward while the mechanical valve is closing the side channel. From equations 5.4 and 5.6, the droplet volume can be obtained as follows

$$V_{drop} = V_{disp} - V_{back} = V_{disp}\left(0.84 + 1.91\exp\left(-3.1\times10^{-2}V_{disp}\right)\right)$$

$$V_{drop} = V_{disp} - V_{back} = \left(0.19 + 0.84\exp\left[\frac{-t}{119}\right]\right)\left[\left(\frac{Z_{ci}}{Z_d Z_{ci} + Z_{co}Z_{ci} + Z_d Z_{co}}\right)P_{cd}t\right]$$

$$\times\left[0.84 + 1.91\exp\left(\left(-0.031\right)\left(0.19 + 0.84\exp\left[\frac{-t}{119}\right]\right)\left(\frac{Z_{ci}}{Z_d Z_{ci} + Z_{co}Z_{ci} + Z_d Z_{co}}\right)P_{cd}t\right)\right]$$

(5.7)

where V_{drop} is the droplet volume. **Figure 5.5c** shows the summary of all the steps described above. For step 1, the dispensed phase rapidly fills the vacant space above the valve area, and the flow rate of the dispensed phase decreases until the dispensed phase meets the continuous phase. For step 2, the flow rate of the dispensed phase is kept constant. For step 3, part of the dispensed volume of the dispensed phase moves backward. It is worth mentioning that equations 5.4-5.7, based on the theoretical model, predict the volumetric movement of the dispensed phase during the droplet formation well, as shown in **Figure 5.5c.**

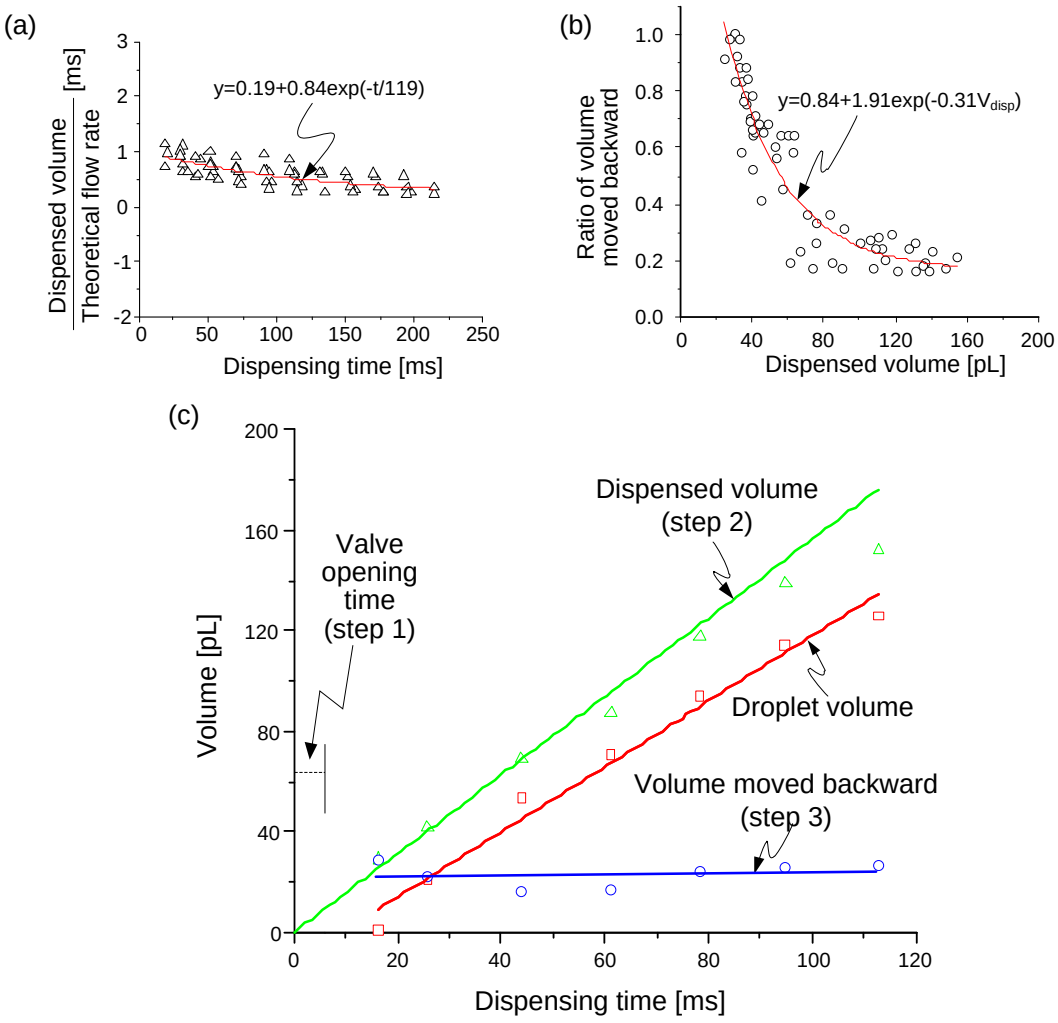

Figure 5.5 | Volumetric movements of dispensed phase (a) during steps 1 and 2, and (b) during step 3. All the experimental data were processed to obtain the curve fits. (c) Summary of volume movement (channel height: 15.3 μm, pressure: 17.2 kPa, dispensed phase viscosity: 3.27 mPa·s). Symbols are experimental data and solid lines represent theoretical results.

5.5 Conclusion

We have built a descriptive and quantitative model on droplet formation through mechanical cutting in a microchannel with a T-junction configuration. To clarify the

parameters of importance and their effects on droplet generation, we did an experimental parametric study varying the flow channel height, the pressure driving the liquids in the flow channel, and the dispensed phase viscosity. The droplet formation process by using the theoretical model is composed of three steps. For step 1, the dispensed phase rapidly fills the vacant space above the valve area, and the flow rate of the dispensed phase decreases until the dispensed phase meets the continuous phase. For step 2, the flow rate of the dispensed phase is kept constant. For step 3, part of the dispensed volume of the dispensed phase moves backward. The droplet generation process by using mechanical cutting is clearly explained with the predictive model proposed in the present work. This study could be applied for advanced designs for highly flexible droplet-based microfluidic systems.

Chapter 6

DETERMINATION OF CATALYTIC COMPETENCE FROM FLEXIBLE CONCENTRATION GRADIENTS

6.1 Introduction

Chemical and biochemical reactions in pico/nanoliter-sized droplets have been studied intensively during the past decade{Brouzes, 2009 #119;Huebner, 2008 #120;Teh, 2008 #106;Song, 2003 #121}. The droplet-based reactions offer a number of advantages over conventional microliter or milliliter scale reactions. The reduction in droplet volume enables rapid reactions due to extremely small heat capacity and shorter diffusion distances{Tabeling, 2005 #3}. The ability to conduct a large number of parallel reactions with droplets is another advantage{Prakash, 2007 #122;Hong, 2009 #123;Teh, 2008 #124} in addition to confinement of reagents with distinct reaction conditions, and isolation of droplets to avoid nonspecific binding of biomolecules to the channel wall{Song, 2006 #125;Teh, 2008 #106}. To explore these advantages, different droplet formation methods have been reported to achieve control over size, shape, and mono-dispersity of droplets {Huebner, 2008 #120;Teh, 2008 #106;Song, 2006 #125}.

6.2 Objective

Here, we demonstrate a new way to realize a stepwise concentration gradient in consecutive microdroplets through generation of different sizes of droplets and subsequent injection and merger of the droplets. To show the potential of the present

system, a stepwise concentration gradient of a substrate in ten picoliter droplets was generated for the evaluation of the catalytic competence of two enzymes, MMP-2 and MMP-9 in a single experiment.

6.3 Materials and Methods

Materials

Matrix metalloproteinases-2 (MMP-2), matrix metalloproteinases-9 (MMP-9) and MMP substrate III, (QXL^{TM}520-Pro-Leu-Gly-Cys-(Me)-His-Ala-D-Arg-Lys-(5-carboxyfluorescein)-NH_2) were used, as a model system. MMP-2 and MMP-9 are considered to play an important role in metastasis and are targets for drug development.{Egeblad, 2002 #135;Yoneda, 1998 #136;Yoneda, 1998 #136;Egeblad, 2002 #135} MMP-2 and MMP-9 were purchased from R&D Systems, Inc., and we used the MMP substrate III was from AnaSpec Inc. The MMP substrate III used for the present work is a specially designed and commercially available peptide substrate. The substrate has an attached fluorophore, 5-carboxy-fluoresein-Pro-Leu-OH (FAM), on one end of the peptide substrate and a quencher, QXL520, on the other end. Upon enzymatic cleavage of the peptide substrate, the fluorescence of FAM is emitted, and the fluorescence signals are observed as an indicator of enzymatic reaction (**Figure D1** in Appendix D). Stock solutions of 200 nM of MMP-2 and 9 in a reaction buffer (50 mM Tris, 10 mM $CaCl_2$, 150 mM NaCl, 0.05% Brij-35, and 0.1% BSA at pH 7.5) were prepared. Immediately before use, the thawed stock solutions were diluted with the reaction buffer solution. All the experiments were conducted at room temperature (25 ± 1.5 °C). During the on-chip experiments, mineral oil (Sigma Inc., product number M5904) was used as a continuous phase and no surfactant was used in the microchannels.

Chip fabrication

The mask was designed using AutoCAD software (AutoDesk Inc., San Rafael, CA) and printed on a transparent film at 20,000 dpi (CAD/Art Services, Inc., Bandon, OR). The molds for the two layers, fluidic and control, were fabricated by a photolithographic technique. At first, the positive photoresist (AZ P4620, AZ electronic materials) was spin-coated onto a 4-inch silicon wafer. This was followed by UV exposure and development. For reliable opening and closing of the valves, the photoresists for fluidic layer was rounded by heating the mold at 130 °C for 2 min.

The top thick fluidic layer of the chip was prepared by pouring uncured polydimethylsiloxane (PDMS, GE RTV615; elastomer:crosslinker = 10:1) onto the fluidic layer mold to achieve a thickness of 5 mm. The bottom control layer of the chip was fabricated by spin-coating uncured PDMS (elastomer:crosslinker = 20:1) onto the control layer mold at 3000 rpm for 1 min. The two layers were cured for 1 h (fluidic layer) and 45 min (control layer) at 80 °C, respectively. The fluidic layer was peeled off from the mold, and holes were punched for inlet/outlet ports to the flow channels through the thick layer with a 19-gauge punch (Technical Innovations, Inc, Brazoria, TX). The fluidic layer was aligned over the control layer. The two layers were bonded by baking at 80 °C for 45 min. The bonded layers were peeled off from the control layer mold, and holes were punched for inlet ports to the control channels. Finally, the PDMS chip were placed on a pre-cleaned glass slide (Fisher Scientific Pittsburgh, PA) and kept it in an oven at 80 ^{o}C for 18 h to advanced curing.

Labview based pneumatic control.

The pneumatic control setup consisting of four sets of eight-channel manifolds (Fluidigm Corporation) was controlled through a BOB3 control board (Fluidigm Corporation). We mounted a digital I/O card (NI PCI-6533 (DIO-32HS), National Instruments) in the computer to digitally control the switching of each channel of the manifold. For the accurate control of the droplet generation process, a custom-built LabVIEW (National Instruments) program was developed. We used this LabVIEW program for sending the appropriate signal with predetermined dispensing time and the corresponding droplet volume calculated from our predictive model published before{Lee, 2009 #86;Lee, 2009 #86;Lee, 2009 #86;Lee, 2009 #86}. Based on the model results, at the start of the actual experiment, preliminary experiments were conducted to establish the relation between the dispensing time and the corresponding droplet volumes (**Figure 6.2a**).

Image acquisition and processing.

A series of fluorescence images of the enzyme reactions were acquired with a modified biochip reader (arrayWoRx®, Applied Precision, WA). All fluorescence images shown in **Figure 6.3a** and **b** were digitized and analysed by using the time series analyser of ImageJ software (NIH, USA). 5-FAM (5-carboxyfluorescein) droplets were generated of concentration range, 0.3 μM to 1.5 μM with the increment of 0.3 μM, and measured the fluorescent intensities by collecting fluorescence images. During the measurement, it was observed that 0.7% of the fluorescent intensity was decreased due to photobleaching of the fluorescent molecule during each fluorescence scan (**Figure D7** in Appendix D). The loss of fluorescent intensities was compensated for accurate kinetic analysis{McGrath, 1998 #55}.

6.4 Results and Discussion

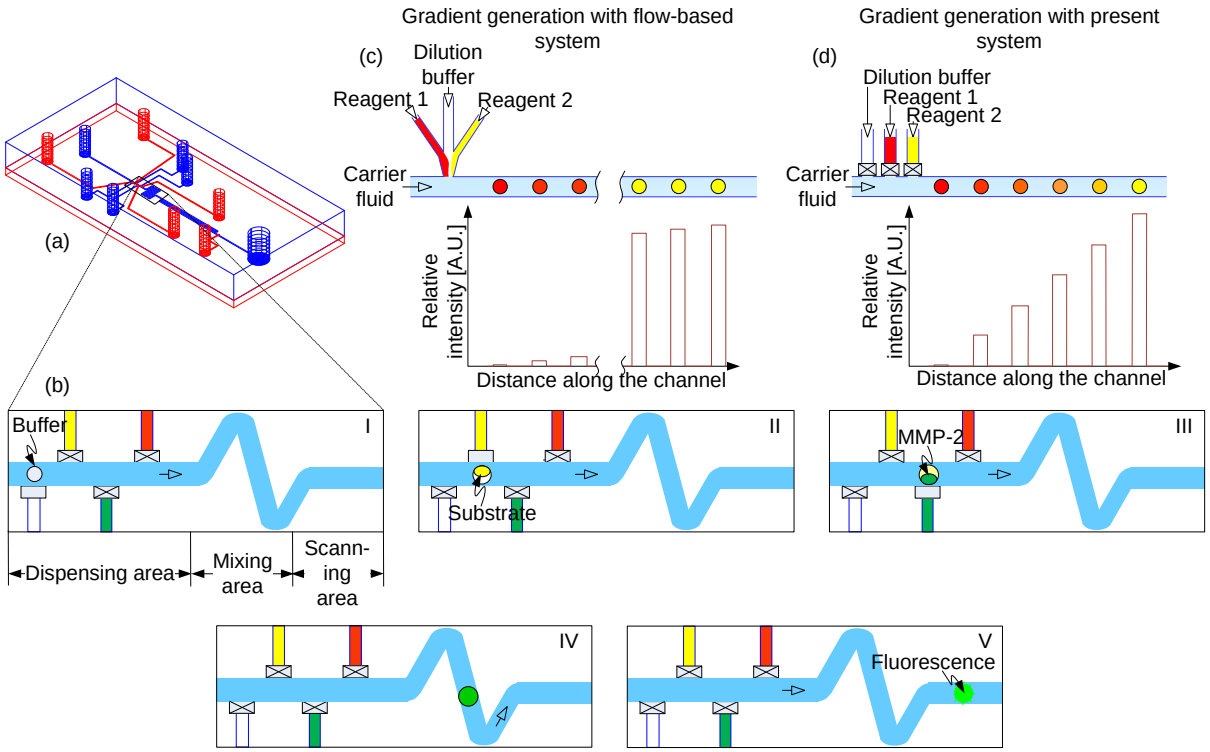

Figure 6.1 | Concentration gradients in droplet reactors. (a) design of the microfluidic system. Blue and red colors indicate fluidic channels and control channels, respectively. (b) step-by-step generation of droplets with different compositions (See text for explanation). (c) Gradient generation with flow-based system. (d) gradient generation with present system. Dilution buffer, MMP substrate III, MMP-2 and MMP-9 were fed in the form of droplets through the vertical dispensing channels.

Device operation

The system to generate picoliter-scale droplets consists of a continuous phase channel that is running left to right and dispensing channels which are perpendicular to the continuous phase channel (**Figure 6.1a, b**). The distinct difference between the present system and other analog or low concentration gradient droplet systems{Song,

2003 #121} is the inclusion of a mechanical valve as shown in **Figure 6.1c, d**. We positioned a set of microvalves at the end of the four dispensing channels as shown in **Figure 6.1b**. Based on the functionality, the continuous phase channel can be divided into three parts: dispensing area, mixing area and incubation area. In the dispensing area, the picoliter scale droplets were generated by the opening and closing of the valves and the generated droplets were moved through the continuous phase channel, mineral oil channel. For instance, by the operation of the valve of the first dispensing channel, we can generate a droplet of buffer. This droplet moves forward due to the flow of continuous phase. When the buffer droplet approaches the second dispensing channel, the second droplet of a substrate is ejected and merged to the buffer droplet. A schematic explanation of the processes of conducting enzymatic reactions with generating and merging picoliter droplets is depicted in **Figures 6.1b-I to V**. The enzymatic reactions consist of MMP-2 and MMP-9 enzymes, and MMP substrate III. For the sake of simplicity, we have explained only one reaction with MMP-2 and MMP substrate III. Firstly, the buffer droplet was ejected from the buffer dispensing channel (**Figure 6.1b-I**). When the buffer droplet approached the substrate dispensing channel, as a second step, the substrate droplet was ejected to form a merged buffer-substrate droplet (**Figure 6.1b-II**). In third step, the merged buffer-substrate droplet was combined with the third droplet of enzyme after its ejection from the MMP-2 dispensing channel (**Figure 6.1b-III**). The reagents inside the individual merged droplets were mixed when flowing through the winding channel (**Figure 6.1b-IV**), known as the mixing area, through the process of chaotic advection{Bringer, 2004 #127}. Due to mixing of enzyme and substrate in the merged droplet, fluorescence from the droplet was intensified

continuously (**Figure 6.1b-V**). Finally, this increasing fluorescence intensity was detected by using the biochip reader at a 60-second interval. In parallel, the reaction for the MMP-9 enzyme and MMP substrate III was conducted by using the same procedure of five steps on the same chip. We charted the relationship between droplet volumes from 30 pL to 150 pL and their corresponding dispensing time that is equivalent to the valve opening time as shown in **Figure 6.2a**. This linear relationship between the valve opening time and the droplet volume was confirmed for three sets of experiments with a standard deviation of 1.6% in the droplet volume. These results confirm the accuracy and reproducibility of the present droplet system.

Table 6.1 | Compositional changes of droplet reactors.

Substrate dispensing volume [pL]	Dilution buffer dispensing volume [pL]	Enzyme dispensing volume [pL]	Concentration of substrate [μM]	Concentration of MMP-2 enzyme [nM]	Concentration of MMP-9 enzyme [nM]
30 ± 1.4	147.3 ± 3.0	180 ± 3.2	3.0	2.5	4.0
60.7 ± 3.0	120.1 ± 1.3	180 ± 3.0	6.0		
90.5 ± 3.4	90.5 ± 3.4	180 ± 2.7	9.0		
120.1 ± 1.3	60.7 ± 3.0	180 ± 2.4	12.0		
147.3 ± 3.0	30 ± 1.4	180 ± 2.1	15.0		

Standard curve

To calibrate the velocity characterization of enzymatic reactions of MMP-2 and MMP-9 with MMP substrate III, we generated a series of droplets having different concentrations of fluorescent molecules, 5-carboxy-fluoresein-Pro-Leu-OH (FAM) on a chip and plotted a standard curve (**Figure 6.2b).** The FAM emits fluorescent light at 520 nm, which is identical to the wavelength of fluorescence emitted by the product of MMP-2 and 9 when MMP substrate III is used. Internally quenched MMP substrate III does not emit any fluorescent signal without enzymatic reaction. Thus, the increase in the

fluorescence intensity can be used to monitor the rate of catalytic reactions of MMP-2 and 9 when MMP substrate III is used as a substrate.

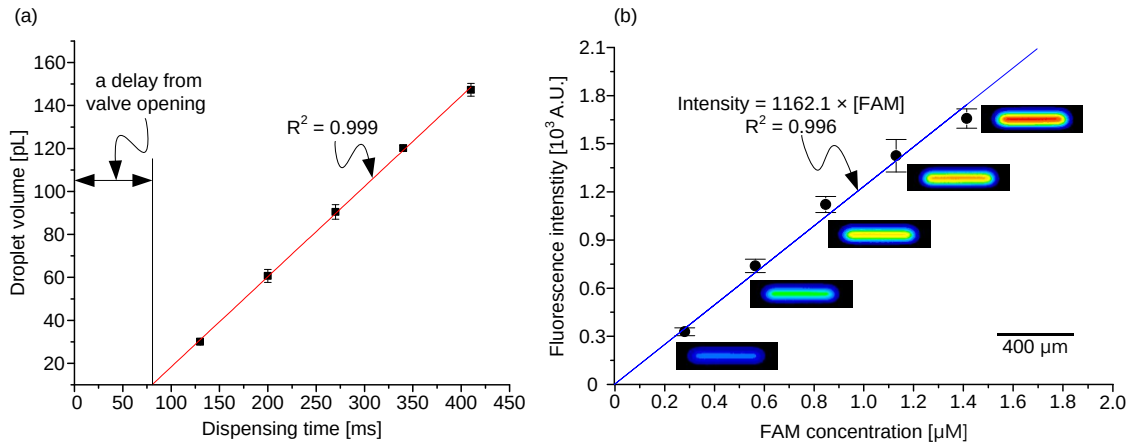

Figure 6.2 | Relationship between the 5-FAM concentration and the fluorescent intensity. (a) dispensing time versus volume of scale droplets. (b) a standard curve of the fluorescent intensity vs. FAM concentration. Scanned images of the micro-droplets show different concentrations of FAM.

Figure 6.2b shows the scanned images of the five droplet microreactors containing different concentrations of FAM. The concentration was varied linearly from 0 to 1.5 μM with an increment of 0.3 μM. The changes in colors of the droplets indicate the increasing fluorescence intensity of the droplets. We measured the intensity of the whole area of each droplet to calculate the velocity of the enzyme reactions and we observed that the intensities at the center of the droplets were higher compared to those of the edge of droplets. We attribute this intensity variation in the droplet to the rounded shape of the fluidic channel (**Figure D2** in Appendix D). To prevent the non-specific binding of proteins and chemicals on the channel walls{Toepke, 2006 #137}, we added 0.1% of bovine serum albumin (BSA) which is widely used as a blocking reagent{Jambovane,

2009 #11;Arenkov, 2000 #33} to the buffer. We also generated a standard curve of FAM for conventional enzyme experiments by using a spectrophotometer (**Figure D3** in Appendix D).

Determination of kinetic parameters

The accuracy of kinetic parameters such as K_M and k_{cat} is affected by the enzyme concentration{Segel, 1993 #138;Copeland, 2000 #35} and its linear response to a range of substrate concentrations{Copeland, 2000 #35}. To determine the enzyme concentration suitable for the experiments, the substrate concentration needs to be maintained high in order to avoid substrate depletion{Bisswanger, 2004 #139} and to help an enzyme to reach its saturation limit without falling short of substrate molecules{Copeland, 2000 #35}. We varied the enzyme concentrations using conventional methods from 0.5 to 35 nM for both MMP-2 and MMP-9 by keeping the MMP substrate III concentration high, 30 μM. We traced the reaction velocities for 120 min. For MMP-2, with the substrate concentration at 30 μM, we observed linear velocity responses up to 11 min with 0.5 and 2.5 nM concentrations of the enzymes. At higher concentrations, above 2.5 nM of the enzyme, we witnessed nonlinear responses. Consequently, we used 2.5 nM of MMP-2 for the rest of the experiments. For MMP-9, linear velocity was observed up to 11 min at 0.5 nM and 4 nM of the enzyme concentration. Hence, we used 4 nM of MMP-9 for the rest of the experiments. (**Figure D4** in Appendix D). We used these enzyme concentrations hereafter. The difference in the enzyme concentrations for MMP-2 and MMP-9 is due to different upper limit of linear velocity responses{Hutzler, 1975 #140;O'Sullivan, 2002 #141;Eisenthal, 2002 #142;Diamondstone, 1966 #143}.

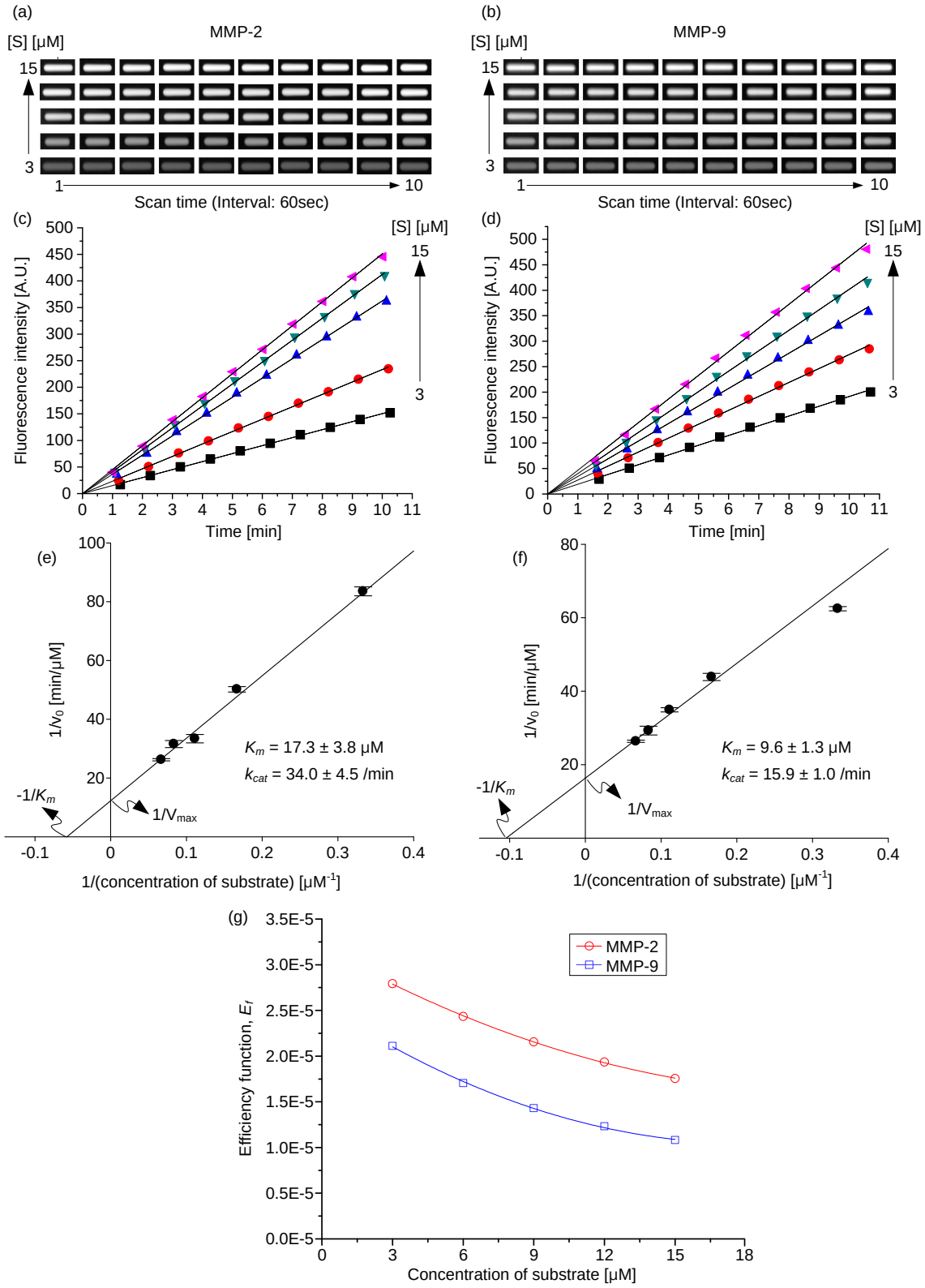
(a)
MMP-2
[S] [μM]
15
3
1
10
Scan time (Interval: 60sec)
(b)
MMP-9
[S] [μM]
15
3
1
10
Scan time (Interval: 60sec)
(c)
Fluorescence intensity [A.U.]
Time [min]
[S] [μM]
15
3
(d)
Fluorescence intensity [A.U.]
Time [min]
[S] [μM]
15
3
(e)
1/V0 [min/μM]
Km = 17.3 ± 3.8 μM
kcat = 34.0 ± 4.5 /min
-1/Km
1/Vmax
1/(concentration of substrate) [μM-1]
(f)
1/V0 [min/μM]
Km = 9.6 ± 1.3 μM
kcat = 15.9 ± 1.0 /min
-1/Km
1/Vmax
1/(concentration of substrate) [μM-1]
(g)
MMP-2
MMP-9
Efficiency function, Ef
Concentration of substrate [μM]

Figure 6.3 | Series of scanned images of the droplet microreactors for the enzymatic reactions of MMP-2 (a) and 9 (b). MMP substrate III gradient from 3 μM to 15 μM was used. It can be observed that the fluorescent signals increase with the substrate concentration (bottom to top) and the reaction time (left to right). The fluorescent intensity of each droplet reactor was digitized and plotted for MMP-2 (c) and MMP-9 (d). Lineweaver-Burk plots of MMP-2 (e) and 9 (f) under different substrate concentrations. (g) Variation of the efficiency function (E_f) for MMP-2 and MMP-9.

For enzymatic reaction reactions inside the droplets on a chip, we generated two sets of substrate concentration gradient from 3 to 15 μM by adjusting volume of the buffer droplet and the substrate droplet. Then, 2.5 nM of MMP-2 was introduced for the first set of the five droplets and 4.0 nM of MMP-9 for the next five droplets.

Detailed information on volume of each component of the merged droplets is found in **Table 6.1**. The fluorescent signals resulting from the enzymatic reaction of MMP-2 and MMP-9 inside the droplet reactors were scanned for a period of 11 min using 1 min intervals (**Figure 6.3a** and **b).** These scanned images were digitized to obtain the fluorescence values of each droplet. The digitized intensity values that represent the progress of the reactions are plotted (**Figure 6.3c and d)**. Although each droplet is scanned at shifted time points, the scanning interval for each droplet is same (**Figure D5** in Appendix D). Hence, the initial velocity of reaction in each droplet reactor was calculated from respective reaction progress plots. In order to determine the kinetic parameters, the initial velocities and substrate concentrations were plotted with Lineweaver-Burk plots (**Figure 6.3e** and **f)**. In the curve fitting, the nonlinear regression analysis was used to find the Y-intercept ($1/V_{max}$) and the X-intercept ($-1/K_M$). The half

maximal activity, K_M of MMP-2 and 9 determined from three independent experiments were 17.3 ± 3.8 μM and 9.6 ± 1.3 μM, respectively. The calculated turnover number, k_{cat}, of MMP-2 and 9 were 34.0 ± 4.5 /min and 15.9 ± 1.0 /min, respectively. To validate our on-chip results, we also conducted conventional experiments (**Figure D6** in Appendix D). The K_M values of MMP-2 and 9 were 14.8 ± 1.8 μM and 8.1 ± 1.1 μM, respectively. The turnover number k_{cat}, from the conventional methods, of MMP-2 and 9 were 32.3 ± 2.3/min and 14.1 ± 0.9 /min. The deviations of K_M and k_{cat} from our droplet and conventional experiments were 16.9% and 5.3% for MMP-2 and 8.5% and 12.8% for MMP-9. The deviations are acceptable for enzymatic reactions because enzymes are biological samples with variable properties and the experimental errors involved in the kinetic measurements of enzymes could never be completely eliminated{Cornish-Bowden, 1995 #61}.

Evaluation of catalytic competence

The evaluation of catalytic competence of multiple enzymes consists of reactions with substrate concentration gradients under uniform experimental conditions{Benner, 1989 #144}. Ideally, for keeping the experimental conditions uniform, the reactions needs to be conducted in parallel under the same experimental conditions. The ability of the present system to generate substrate concentration gradient in parallel architecture makes it possible for the direct evaluation of catalytic competence. For this evaluation, the catalytic efficiency, k_{cat}/K_M is one of the commonly used second order rate constant{Eisenthal, 2007 #40}. From the on-chip experiments, the calculated values of k_{cat}/K_M for MMP-2 and 9 were 1.8 and 1.6 $\mu M^{-1}min^{-1}$ respectively. The values of k_{cat}/K_M using conventional methods were found to be 2.0 $\mu M^{-1}min^{-1}$ for MMP-2 and 1.6 μM^{-}

^{1}min^{-1} for MMP-9 (**Table 6.2**). The difference between on-chip values and conventional values of k_{cat}/K_M for MMP-2 and MMP-9 were 10.5 and 0.0%, respectively. Because the catalytic efficiency is the ratio of kinetic parameters, its variation depends on the variation of individual values of K_M and k_{cat}{Eisenthal, 2007 #40;Copeland, 2000 #35}. Therefore, the deviation in k_{cat}/K_M of MMP-2 enzyme could be attributed to the aforementioned large variation in K_M.

Table 6.2 | Comparison of kinetic parameters of MMP-2 and MMP-9 with MMP III substrate.

	On-chip	Off-chip	On-chip	Off-chip
K_M (μM)	17.3 ± 3.8	14.8 ± 1.8	9.6 ± 1.3	8.1 ± 1.1
k_{cat} (/min)	34.0 ± 4.5	32.3 ± 2.3	15.9 ± 1.0	14.1 ± 0.9
k_{cat}/K_M ($\mu M^{-1}min^{-1}$)	1.8	2.0	1.6	1.6

Throughout the literature of enzyme kinetics {Oyeyemi, 2010 #145;Cox, 1971 #146;Hubatsch, 1998 #147} scientists use k_{cat}/K_M for reporting the catalytic competence of an enzyme. However, it has been proven that the k_{cat}/K_M alone is an incomplete measure for the evaluation of catalytic competence because it is valid only for substrate concentration, [S], approaching zero{Albery, 1976 #41;Ceccarelli, 2008 #39}. To circumvent the limitation of k_{cat}/K_M, we have used another parameter known as efficiency function, E_f. The efficiency function is also known as practical catalytic efficiency as it takes into consideration the variation of catalytic efficiency with the change in substrate concentration{Ceccarelli, 2008 #39;Albery, 1976 #41;Albery, 1976 #41}. However, to use E_f as the parameter for the evaluation of catalytic competence, similar physiological experimental conditions, such as precise concentration gradient for multiple reagents, need to be maintained for all the reactions{Benner, 1989 #144;Albery, 1976 #41}. This is

quite difficult in conventional experiments. However, with the present system, parallel reactions under identical conditions can be realized by only changing the target enzymes. We determined the values of E_f for both MMP-2 and MMP-9 with variable substrate concentration. As show in **Figure 6.3g**, for the substrate concentrations ranging from 3 to 15 μM, higher values of E_f for MMP-2 were found in comparison to MMP-9. This indicates that, MMP-2 is more effective enzyme than MMP-9 when reacting with MMP substrate III under identical experimental conditions. The results were confirmed by performing off-chip experiments (**Figure D6** in Appendix D). Due to the capability of the simultaneous evaluation of competing enzymes, our microfluidic system would be a unique enzyme screening tool for pharmaceutical{Frase, 2009 #135;Smith, 1992 #136} and biotechnology{Wu, 2003 #137;Kamiya, 1997 #140} field.

Stepwise concentration gradient

The uniqueness of our system lies in its ability to generate multiple droplet reactors having different concentrations of reagents. The general formulation of concentration of a reagent in i^{th} droplet could be given as

$$C_i = \sum_{k=1}^{K} \frac{\left(V_i^k\right)}{\left(V_i^k + V_i^{k+1}\right)} C_i^k \; C_i = \sum_{k=1}^{K} \frac{\left(V_i^k\right)}{\left(V_i^k + V_i^{k+1}\right)} C_i^k , \qquad \text{where } i = 1, 2, \ldots I \text{ and } k = 1, 2, \ldots K \tag{6.1}$$

Here, i and k are identification numbers for the droplet and the required concentration gradient number, respectively; I, K indicate the corresponding total number of droplets and total number of concentration gradients required. In the present case, $I=5$ to accommodate five droplets with different concentration of substrate and $K=1$ because only concentration gradient of substrate was created. In the present system, the independent droplets of enzyme, substrate and buffer are designated as sub-droplets.

Here, the term V_i^k signifies that, we have a control over the volume of individual sub-droplet and, hence, can create concentration gradient in the consecutive droplets. Though, in the present system, we have generated the concentration gradient for MMP substrate III keeping the concentration of enzyme MMP-2 or MMP-9 constant, the concentration gradient could be created for more reagents by adding dispensing channels. Thus, we can conduct multiple, parallel, and combinatorial reactions that are difficult to conduct with existing channel-based{Hadd, 1997 #148;Jambovane, 2009 #11} or other droplet-based systems{Song, 2003 #121;Miller, 2008 #149}.

One exciting potential application opened up by the presented method is the possibility of determining target potency and selectivity{Terrett, 2010 #150}, using only a few pico-liter scale droplets in a single experiment. In addition, it could also open the window for generating the concentration-response plots of multiple proteins or drug candidates when the reactions under the same conditions are performed in parallel. In practice, the concentration-response experiments are commonly performed by inhibitor titration experiments using microwell plates{Copeland, 2005 #66} with millilitre scale drug samples. These experiments could be realized by adding dispensing channels to the present droplet system and by generating '*n*' pico-liter scale droplets for each drug candidate besides the two droplets for positive and negative control of the experiment. The '*n*' droplets for each drug are used for varying the concentration of inhibitor and to measure the velocity of the inhibited reaction. The droplet for positive control is without inhibitor while the droplet for negative control is with saturating concentration of inhibitor. The velocities obtained from '*n*' droplets are used for constructing

concentration-response plots and for determining the IC_{50} values of the target drug candidate.

Another potential application of the present system could be envisioned for the screening of whole cell assays. During the compartmentalization process either a single cells could be entrapped inside the droplet or a number of cells could be grown from single cell for the subsequent drug screening. Next the cell containing droplet is merged with the other droplets for generating the stepwise concentration gradients for example a drug candidate. The fate of the cells, live or dead, could be tracked by direct observation under a microscope or other optical or electrochemical detection methods. The unique advantage of our system includes its ability to conduct an almost unlimited number of reactions with many chemicals or proteins in parallel with a single cell resolution. To adopt this method for the realization of such high throughput screening for comparative assays, the number of parallel dispensing channels could be increased depending on the required number of reagents. Therefore, the present system could be an ideal platform for the drug screening research as mentioned above.

Two practical issues need to be tackled for improving the performance and the application range of the present system. First is the improvement of scan rate and resolution of continuous fluorescence scanning of the droplets. This issue could be addressed by integrating the present device with light emitting diode (LED) based illumination systems and complementary metal oxide semiconductor (CMOS) based diode array for detection. In addition, recently developed wide field lens-free-microscopes {Ozcan, 2008 #151;Coskun, 2010 #152;Ozcan, 2008 #151;Coskun, 2010 #152} could also be incorporated with the present droplet system for broadening the

application range. The second issue is the generation of femto or atto-liter scale droplets. Although we have reported a picoliter scale concentration gradient, the present droplet generation method could be used to generate volumes in femto-liter scale through redesign of the chip.

6.5 Conclusion

In summary, the uniqueness of our droplet system is the flexibility in generation and merging of multiple droplets allowing the creation of stepwise concentration gradients of reagents. Simultaneous enzymatic reactions of MMP-2 and MMP-9 with MMP substrate III were performed in droplet microreactors. Five droplets having different compositions of buffer and substrate were precisely generated with different ratio of 1:5, 2:4, 3:3, 4:2, 5:1, and 6:0 of the buffer and substrate. Although the volume of the buffer and substrate droplets was varied, the droplet volumes for MMP-2 and MMP-9 were not. Two parallel reactions with only five droplet reactors for each enzyme reaction were performed. Increase in the fluorescence of each droplet after merging the three components, buffer, substrate, and enzymes was observed. From the scanned images of the droplets, the kinetic parameters of K_M and k_{cat} of MMP-2 and MMP-9 were determined. The kinetic parameters were used to calculate efficiency function, E_f, and based on E_f values the catalytic competence of MMP-2 and MMP-9 was compared. Our system could be used for conducting kinetic analysis and catalytic competence evaluation of a vast number of other enzymes for academic research and industrial applications.

Chapter 7

Summary and Future Perspective

7.1 Summary

In this dissertation, we have designed and developed direct-dilution based microfluidic platforms for determining multiple enzyme-catalyzed parameters with single experiment and using nano/pico liter scale reagents. This dissertation discusses the invention of advanced and sophisticated devices for conducting investigation of enzyme-catalyzed reactions and dose response of drugs. The dissertation concludes with following contributions:

I. We developed fully integrated microfluidic device that includes sample metering, mixing, and incubation functionalities. The device generates a linear concentrations gradient of reagents in eleven parallel processors. The key parameters for the enzyme kinetics, K_m and k_{cat}, can be determined with a single experiment on the chip. The effect of inhibitor concentrations on the reaction rates was also evaluated by using the device.

II. We demonstrated the generation of log-scale concentration gradients of inhibitors on a single microfluidic device with a semi-direct dilution capability of reagents for the determination of the half-inhibitory concentration or IC_{50}. The log-scale device could be applied in the field of pharmaceutical industry especially for determining IC_{50} in drug discovery.

III. We developed new mechanical valve-based droplet generation method and optimized the microdroplet generation process through circuit-based mathematical modeling. This valve-based droplet generation system and modeling method could be used for complex design of highly flexible droplet-based microfluidic systems.

IV. We presented a device for generating a stepwise concentration gradient in a series of microdroplets by using mechanical micro valves. We demonstrated evaluation of catalytic competence of two enzymes by using just 12 picoliter-scale droplets. This droplet system and stepwise concentration gradient method are highly suitable for applications where the reagents or samples are limited and precious.

7.2 Future perspective

The present research has opened up several avenues for continuing the fundamental and development research in the field of enzyme kinetics due to various advantages described in this dissertation. Following applications may be further explored to extend the future scope of the devices presented in this dissertation.

One exciting potential application of the presented methods is the possibility of determining drug potency and selectivity in a single experiment. In addition, it could also be used for generating the dose-response plots of multiple drug candidates in parallel. In practice, the dose-response experiments are commonly performed by inhibitor titration experiments using microwell plates with millilitre-scale drug samples.

Another potential application of the present system could be envisioned for the screening of cell assays. During the compartmentalization process, a single cell could

also be entrapped inside the droplet or a number of cells could be grown from single cell inside the processors for the subsequent drug screening. Next, the cell containing droplet is merged with the other droplets for generating the stepwise concentration gradients for example a drug candidate. The fate of the cells, live or dead, could be tracked by direct observation under a microscope or other optical or electrochemical detection methods. The unique advantage of our system includes its ability to conduct an almost unlimited number of reactions with multiple chemicals or proteins in parallel with a single cell resolution. To adopt this method for the realization of such high throughput screening for comparative assays, the number of parallel dispensing channels or processors could be increased depending on the required number of reagents. Therefore, the present systems could be an ideal platform for high-throughput drug screening research as mentioned above.

References

Appendix-A

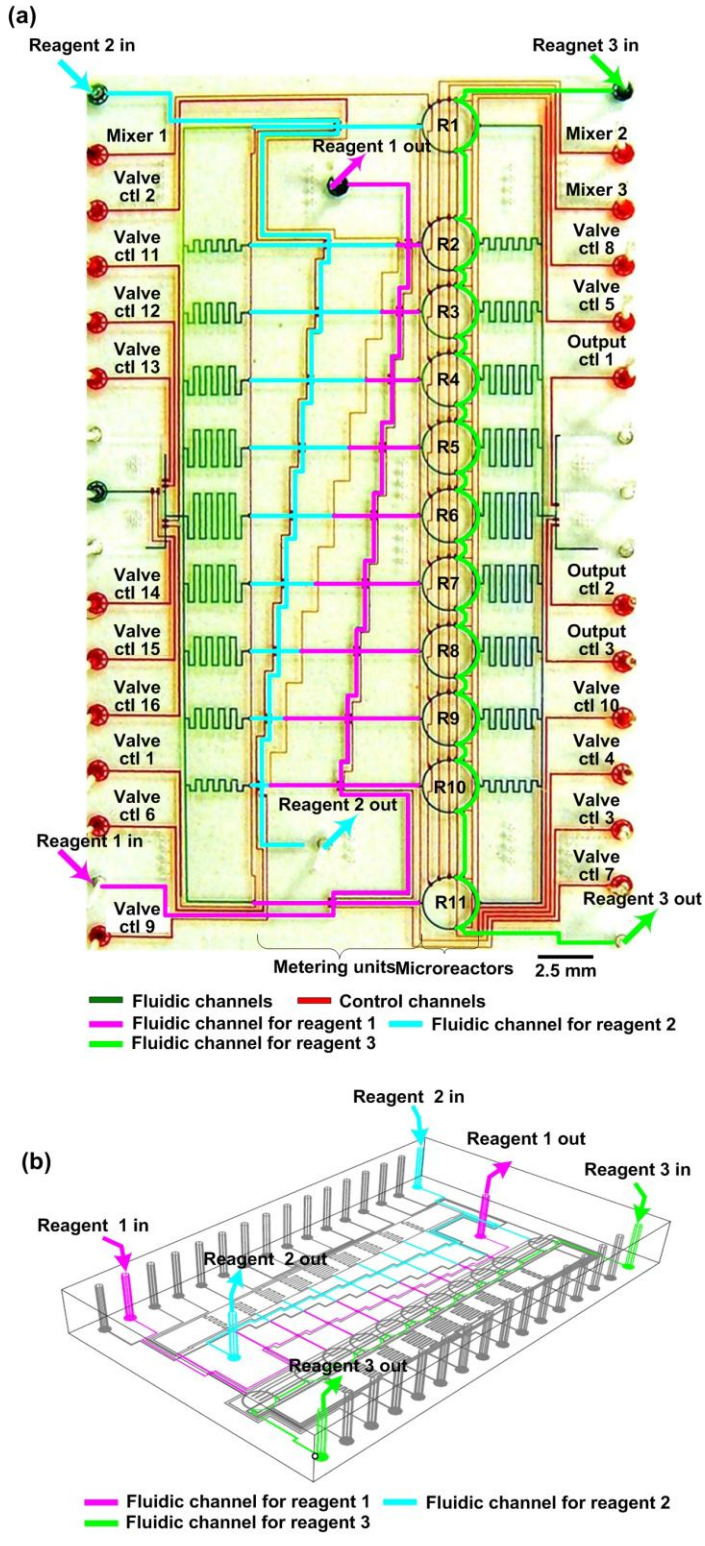

Figure A1. An enlarged photograph of the microfabricated enzyme kinetics chip (a) and schematic representation of the fluidic paths for three reagents (b); the microfluidic

channels of the aqua line, lime line, and magenta line in (b) represent the paths for reagents 1, 2, and 3, respectively. The microfluidic channels for reagents 1 and 2 were composed of a metering unit and were used to produce a series of reagent concentrations. A microfluidic channel for reagent 3 was connected to eleven microreactors in a series and introduced a constant concentration of the reagent into the microreactors.

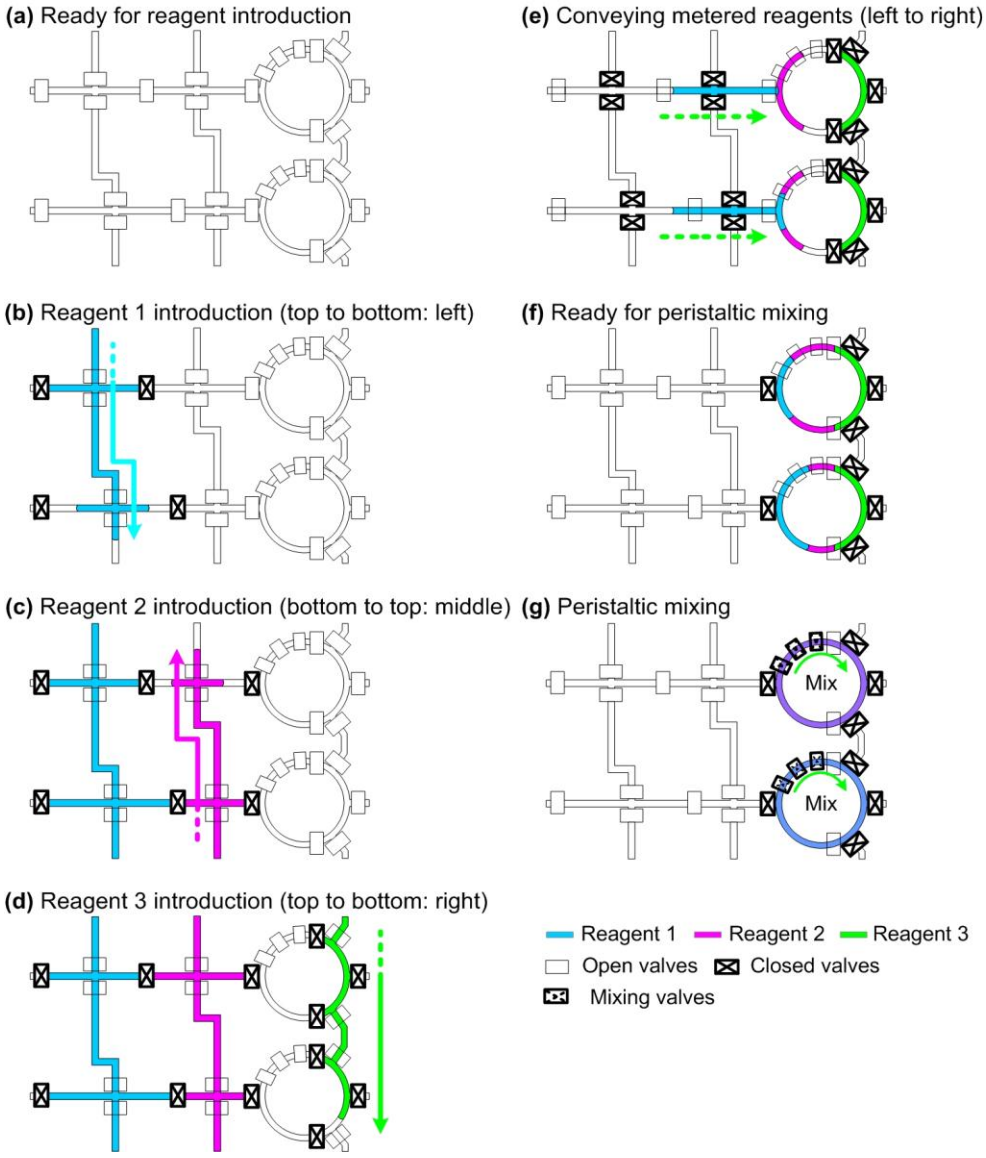

Figure A2. Schematic diagram of the step-by-step operation of the presented microfluidic system.

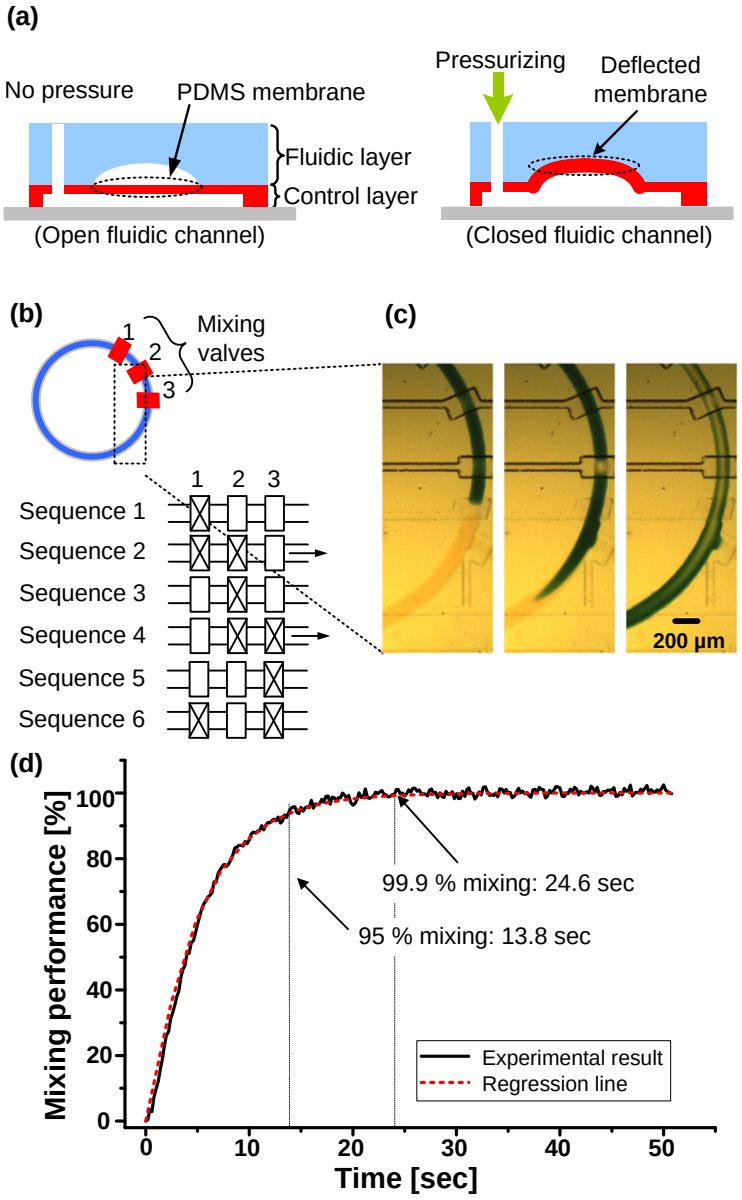

Figure A3. Operation principle of the peristaltic micromixer and mixing phenomena in the presented system. (a) Schematic diagrams of a pneumatically operated valve (left, open valve; right, closed valve). (b) Schematic diagrams of the peristaltic operation of three valves for mixing. (c) Active mixing by operation of three mixing valves. (d) Analysis of the mixing performance. The changes in the average gray value in a

microreactor according to time increases were measured and converted to a percentage of the mixing performance.

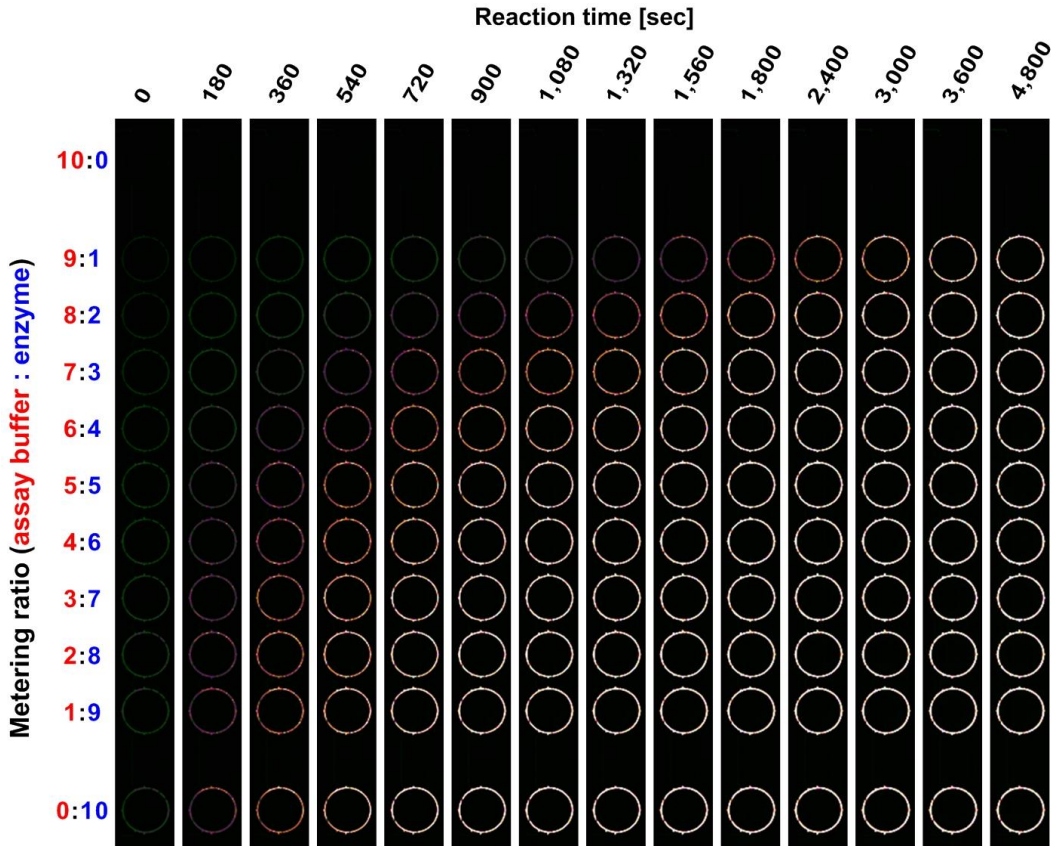

Figure A4. A series of scanned images of the parallel reactions in eleven microreactors. Half of the reactor region was captured to reduce the scanning time. Parallel reactions of a series of enzyme concentrations from 27.9 μg/L to 279 μg/L with an increment of 27.9 μg/L were carried out. The images show product yield increases with the enzyme concentration (top to bottom) and the reaction time increase (left to right).

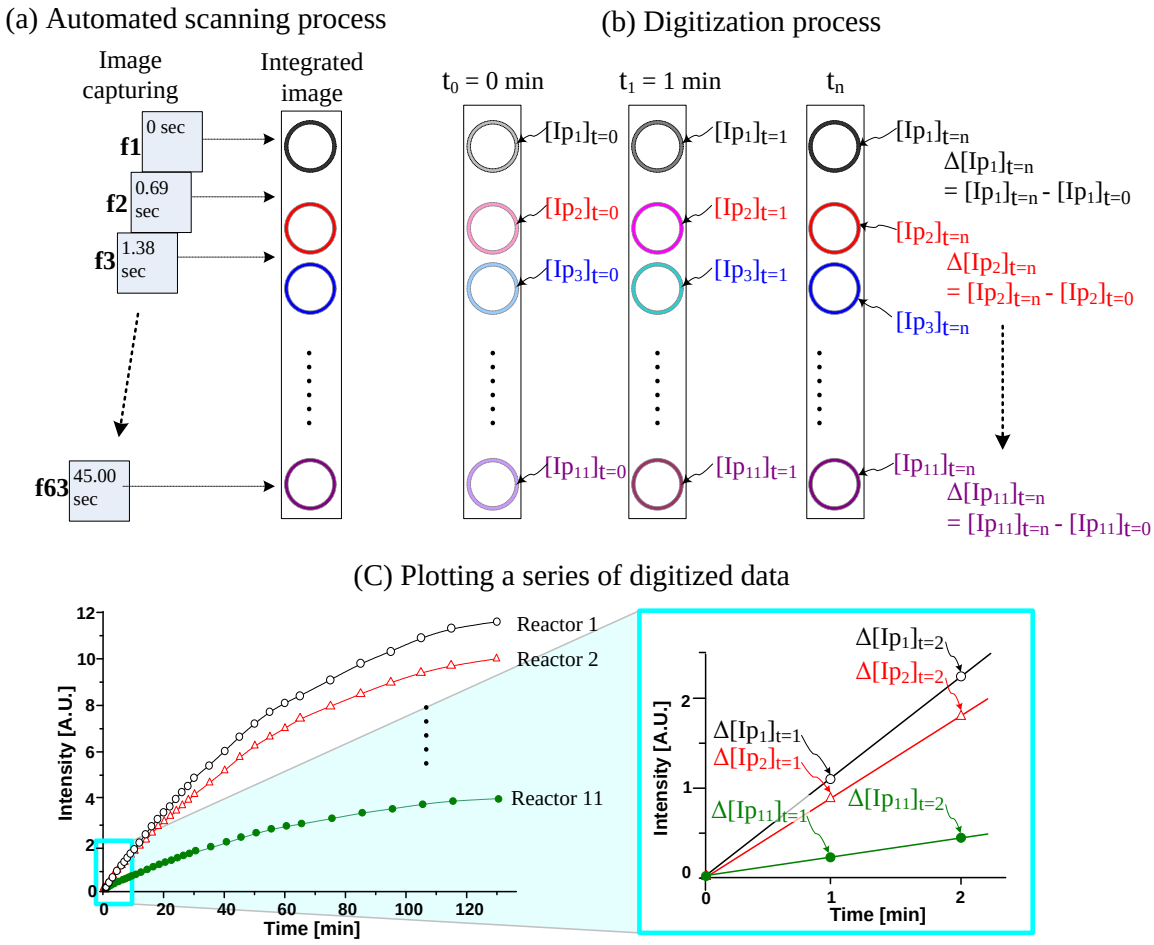

Figure A5. Schematic diagrams represent (a) the image acquisition process, (b) the digitization process, and (c) the plotting process with a set of digitized data.

We used a modified biochip scanner (arrayWoRx®, Applied Precision, WA) to acquire the images from a series of enzyme reactions. **Figure A5** shows the schematic diagrams of automated scanning, digitization of fluorescence intensities and plotting processes. To acquire an integrated image (3.6 mm × 38.3 mm), we captured a square image (1.47 mm × 1.47 mm; minimum scanning area of the scanner used in this research) sixty-three times (0.69 s/scan). Software (arrayWoRx 2.5 Software Suit, Applied Precision, WA) built into the workstation automatically converted the images to an integrated image. The

total scanning time of the integrated image (3.6 mm × 38.4 mm) was approximately 45 s. To digitize the results of the changes of fluorescence intensities as a function of time, we used the time series analyzer of ImageJ software (http://rsb.info.nih.gov/ij/). The time series analyzer allows us to analyze and quantify the intensity of a series of time-lapse images. In **Figure A5(b)**, $[Ip_1]_{t=n}$ represented the mean intensity of the microreactor 1 at a certain time. We subtracted a background intensity (e.g., $[Ip_1]_{t=0}$) from the obtained fluorescence intensity and plotted the time history of the fluorescence intensity change as shown in **Figure A5(c)**. From the data points within 630s (refer to the section on optimization of enzyme concentration), the initial rates of fluorescence changes were determined. By using the slope of standard curve, *Sc*, we determined the initial rate of product formation, v_0, with the following equation:

$$v_0 = \frac{\left(\frac{\Delta[Ip_n]}{\Delta t}\right)}{Sc}$$

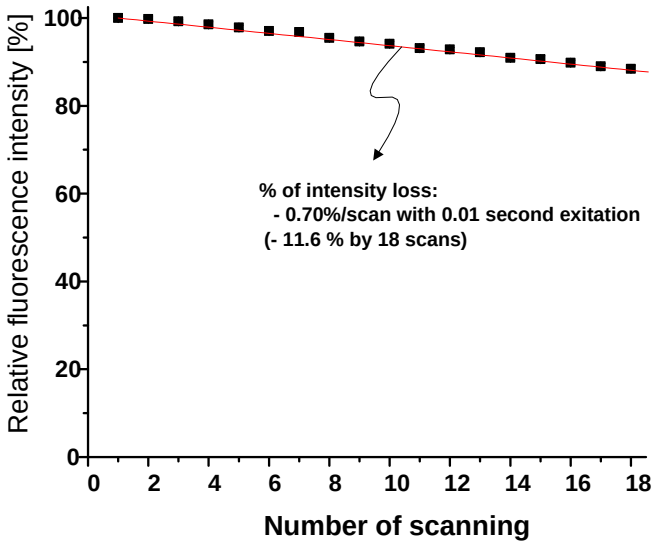

Figure A6. Effect of multiple scans on the photobleaching rate of resorufin. About 0.7 % of the fluorescent intensity was decreased with 0.01s excitation at 535 nm.

Appendix-B

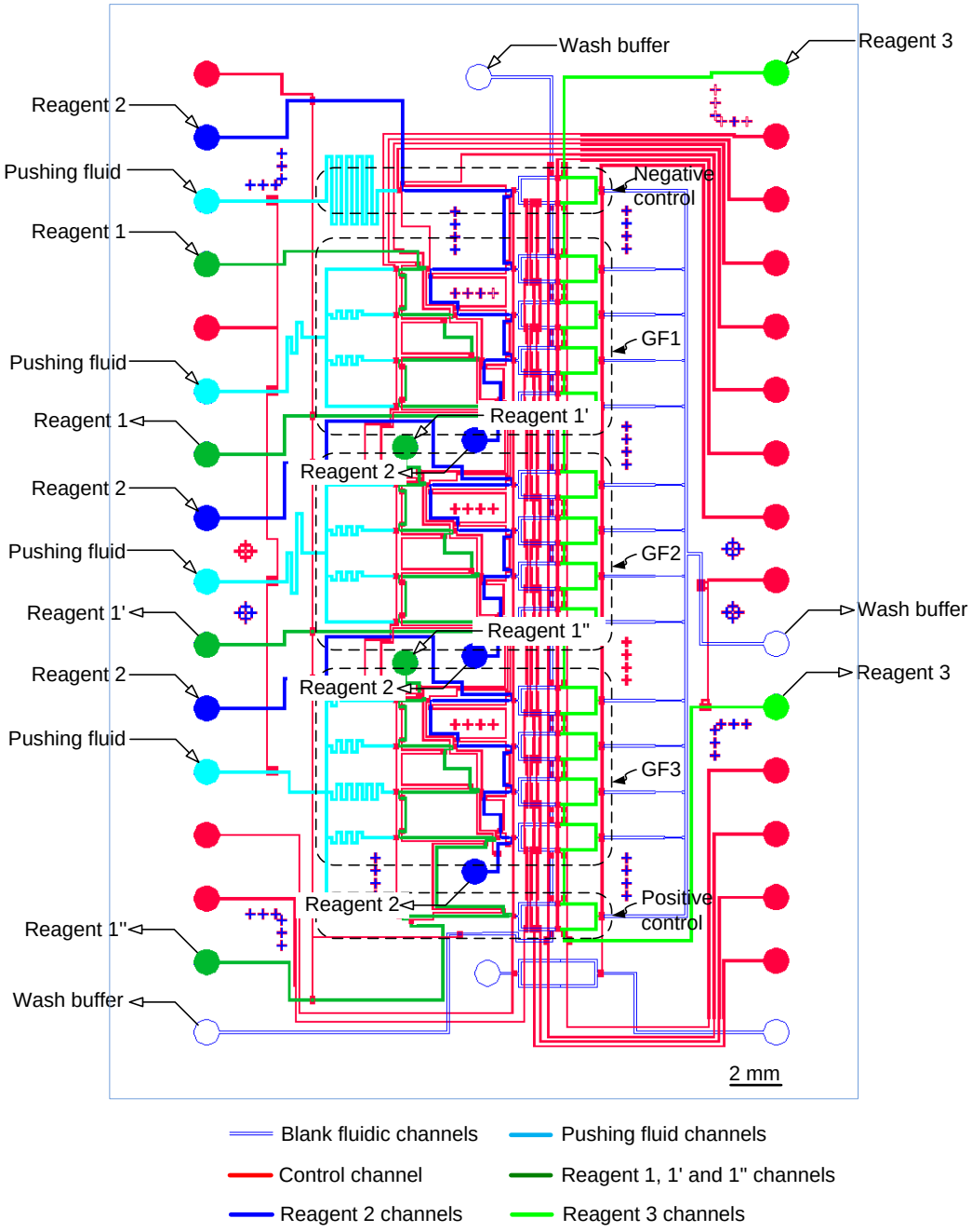

Figure B1. Device structure and channels network.

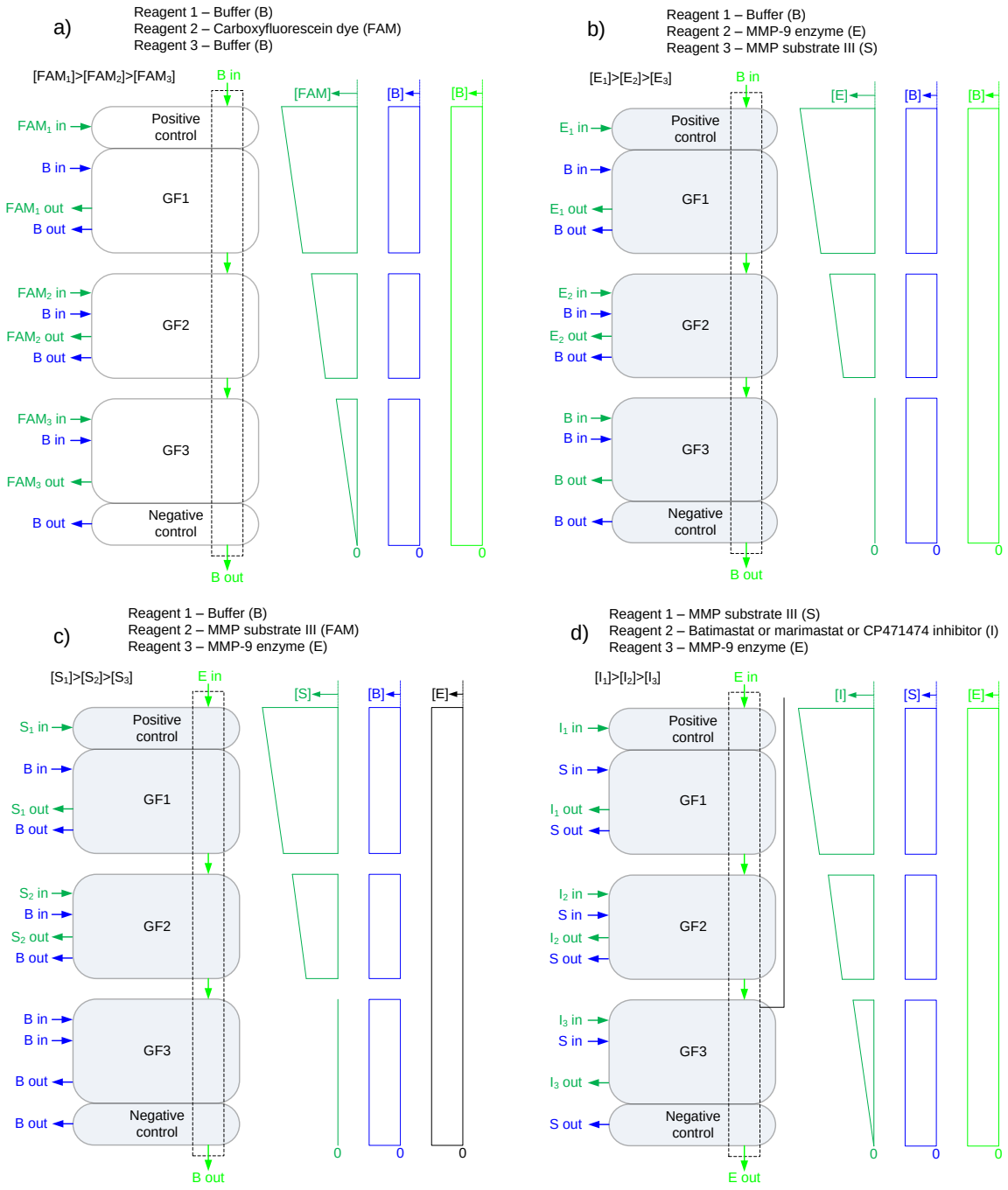

Figure B2. Reagent introduction to the chip for obtaining (a) standadrd curve of FAM, (b) Enzyme gradient, (c) Substrate gradient, and (d) Inhibitor dose response analysis

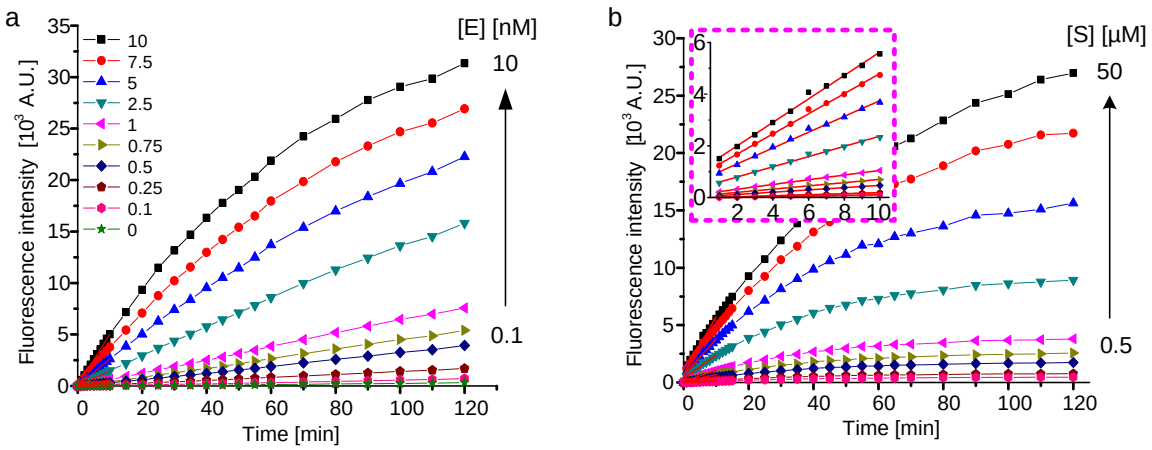

Figure B3. Traces using on-chip method for (a) Enzyme gradient, and (b) Substrate gradient

Appendix-C

Droplet volume calculation

C1. Spherical type droplet

Droplet volume was calculated by using measured droplet diameter from captured picture as shown in Figure C1.

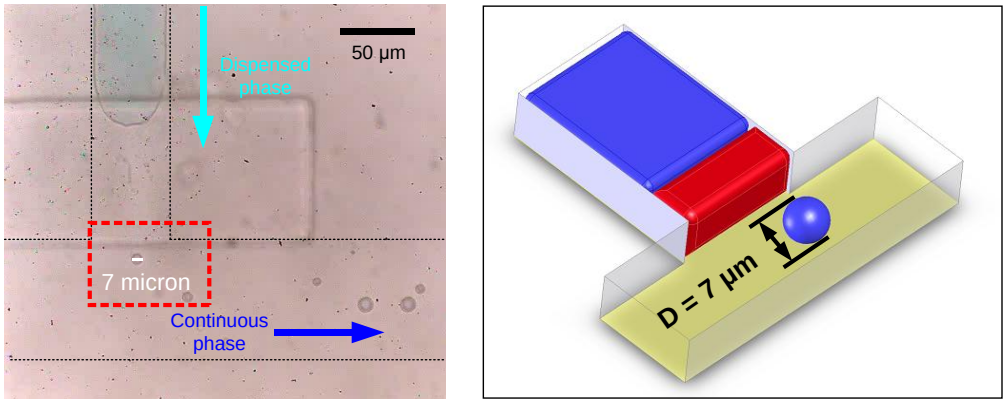

Figure C1. (a) Captured picture for analysis the droplet diameter. (b) Schematic picture for analysis the droplet volume (Channel height = 11.5 µm, Pressure = 17.2 kPa, Viscosity = 1.00 mPa·s, and Set dispensed time = 20 ms).

The followed equations show the calculation results of droplet volume (Channel height = 11.5 µm, Pressure = 17.2 kPa, Viscosity = 1.00 mPa·s, and Set dispensed time = 20 ms).

$$V_{spherical\_droplet} = \frac{4\pi}{3} \times \left(\frac{D_{drop}}{2} \right)^3$$

C2. Ellipsoidal type droplet

Droplet volume was calculated by using measured droplet area from captured picture as shown in Figure C2.

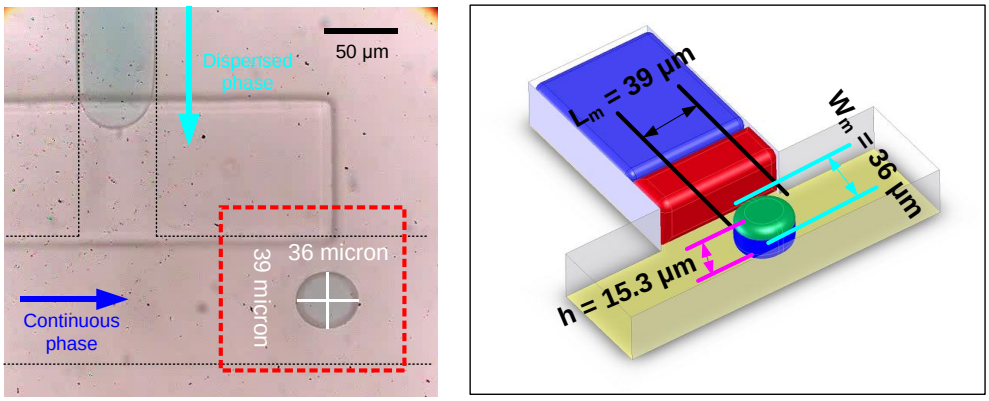

(a) (b)

Figure C2. (a) Captured picture for analysis the droplet area. (b) Schematic picture for analysis the droplet volume (Channel height = 15.3 µm, Pressure = 17.2 kPa, Viscosity = 1.00 mPa·s, and Set dispensed time = 10 ms).

The followed equations show the calculation results of droplet volume (Channel height = 11.5 µm, Pressure = 17.2 kPa, Viscosity = 1.00 mPa·s, and Set dispensed time = 60 ms).

$$V_{ellipsoidal\_droplet} = \frac{4}{3}\pi(r_l)(r_w)(r_h)$$

Droplet diameter was calculated as followed equation.

$$D_{drop} = (\frac{6 \times V_{drop}}{\pi})^{1/3}$$

C3. Elongated type droplet

Droplet volume was calculated by using measured droplet area from captured picture as shown in Figure C3.

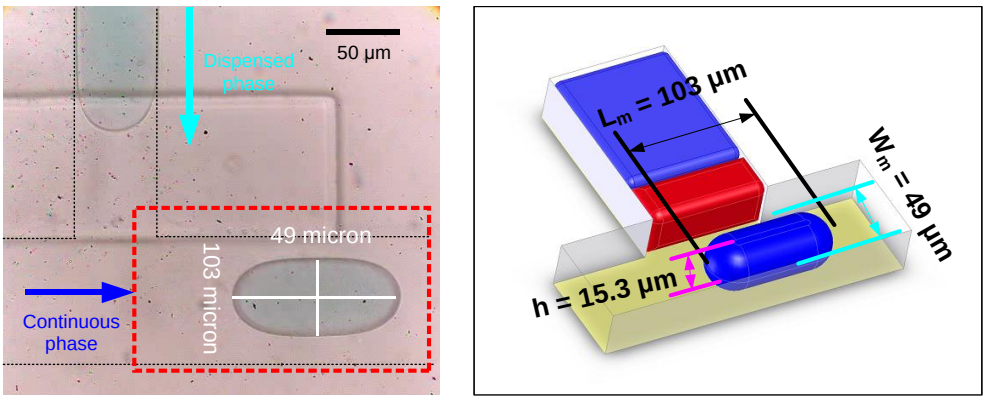

(a) (b)

Figure C3. (a) Captured picture for analysis the droplet area. (b) Schematic picture for analysis the droplet volume (Channel height = 15.3 μm, Pressure = 17.2 kPa, Viscosity = 1.00 mPa·s, and Set dispensed time = 40 ms).

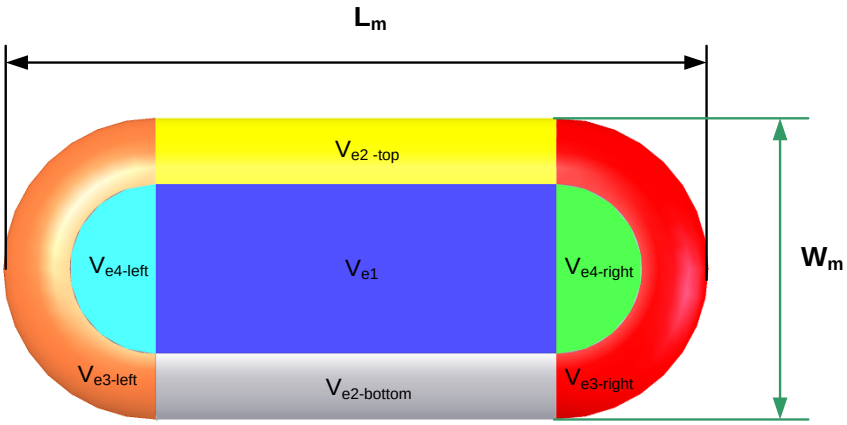

Figure C4. Schematic picture for analysis the elongated type droplet.

Elongated type droplet was divided in four parts as shown in **Figure C4**. We calculated the each part separately, Then the four volumes add to one volume.

- Volume part 1

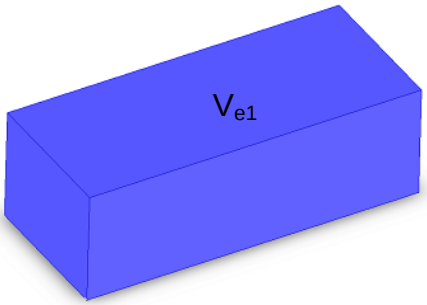

$$V_{e1} = (L_m - W_m)(W_m - h)(h)$$

- Volume part 2

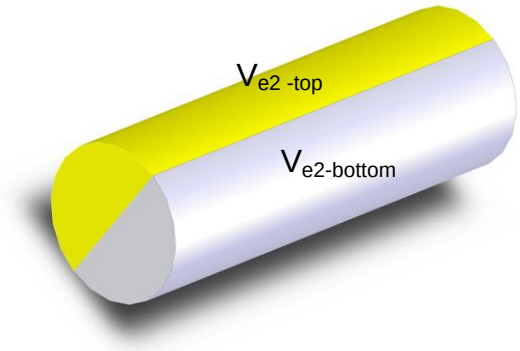

$$V_{e2} = \pi\left(\frac{h^2}{4}\right)(L_m - W_m)$$

- Volume part 3

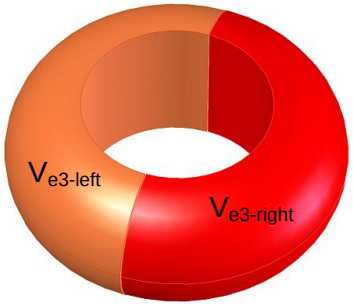

$$V_{e3} = 2\pi\left(\left(\frac{W_m - h}{2}\right) + \frac{4}{3\pi}\left(\frac{h}{2}\right)\right)\left(\frac{\pi}{2}\left(\frac{h}{2}\right)^2\right)$$

- Volume part 4

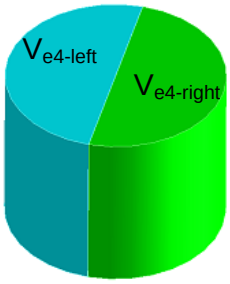

$$V_{e4} = \frac{\pi}{4} h\left(W_m - h\right)^2$$

- Total elongated type droplet

$$V_{elongated\_droplet} = V_{e1} + V_{e2} + V_{e3} + V_{e4}$$

Where

L_m = Maximum length of the droplet; W_m = Maximum width of the droplet;

h = Height of the droplet (channel); r_l = Radius of the droplet along the length;

r_w = Radius of the droplet along the width; $r_h = h$ = Radius of the droplet along the height;

2. Difference in the calculation of c/s area for the droplet in rectangular and rounded channel

2.1 For channel height =11.5 µm

Droplet volume

Maximum width of the droplet = 40 µm

Area of droplet in the rectangular channel = $11.5 \times 40 = 460$ μm^2

Area of droplet in the rounded channel

$$= \int_{-20}^{20} \left[11.36 - (3.84E-16) * w + (2.51E-3) * w^2 + (1.04E-18) * w^3 - (1.29E-5) * w^4 \right.$$

$$\left. -(9.07E-22) * w^5 + (1.36E-8) * w^6 + (2.14E-25) * w^7 - (4.51E-12) * w^8 \right] dw$$

$= 455.69$ μm^2

Where w = Width of the channel in μm

% Difference in the c/s area of the droplet = $\frac{460 - 455.69}{460} \times 100 = 0.94$ %

2.2 For channel height =13.6 μm

Droplet volume

Maximum width of the droplet = 50 μm

Area of droplet in the rectangular channel = $13.6 \times 50 = 680$ μm^2

Area of droplet in the rounded channel

$$= \int_{-25}^{25} \left[13.8 - (9.34E-17) * w - (9.14E-3) * w^2 + (6.78E-19) * w^3 + (1.3E-5) * w^4 \right.$$

$$\left. -(2.18E-21) * w^5 - (1.13E-8) * w^6 + 2.50E-24) * w^7 + (2.73E-12) * w^8 - 8.44E-28) * w^9 \right] dw$$

$= 629.74$ μm^2

Where w = Width of the channel in μm

% Difference in the c/s area of the droplet = $\frac{680 - 629.74}{680} \times 100 = 7.39$ %

2.3 For channel height =15.3 μm

Droplet volume

Maximum width of the droplet = 50 μm

Area of droplet in the rectangular channel = $15.3 \times 40 = 765\ \mu m^2$

Area of droplet in the rounded channel

$$= \int_{-25}^{25} \left[15.39 - (1.06E-16) * w - (4.43E-3) * w^2 + (5.16E-19) * w^3 - (1.35E-6) * x^4 \right.$$

$$\left. -(1.05E-21) * w^5 - (1.01E-9) * w^6 + (8.33E-25) * w^7 + (4.47E-13) * w^8 - (2.18E-28) * w^9 \right] dw$$

$= 717\ \mu m^2$

Where w = Width of the channel in μm

% Difference in the c/s area of the droplet = $\frac{765-717}{765} \times 100 = 6.27\ \%$

Appendix-D

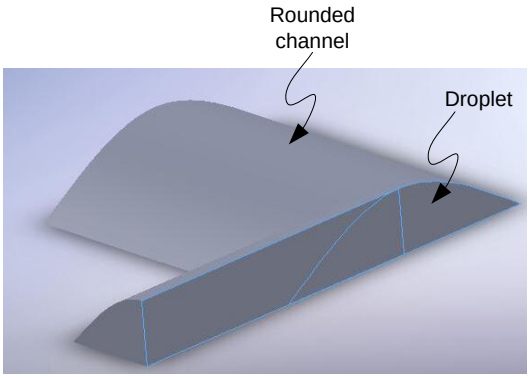

Figure D1. Variation of droplet height in the rounded channel.

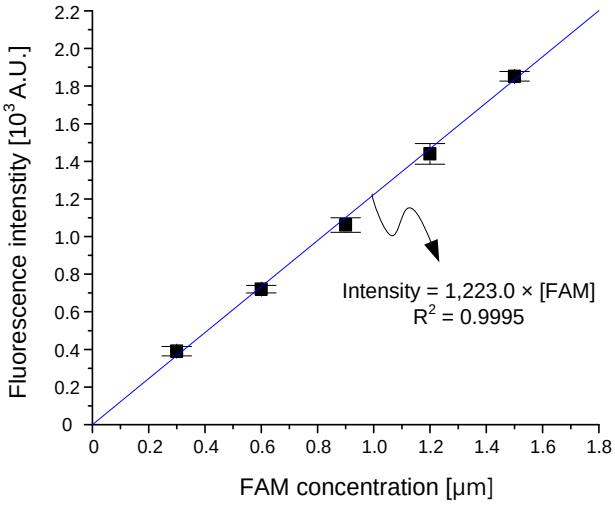

Figure D2. Fluorescence intensity vs. FAM concentration data was obtained using conventional, off-chip, methods.

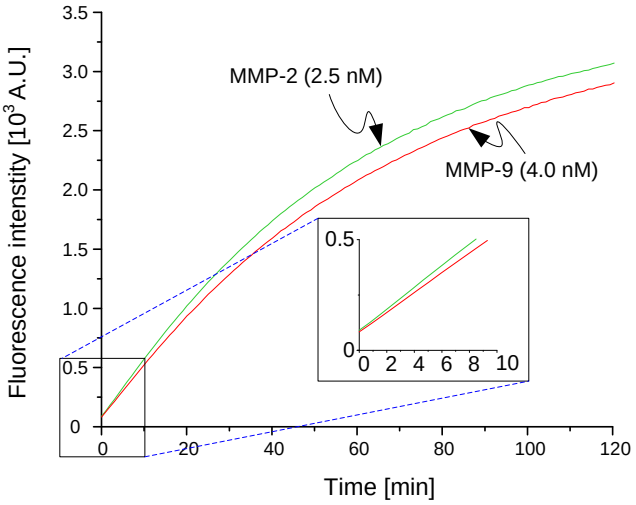

Figure D3. Traces for MMP-2 (2.5 nM) and MMP-9 (4.0 nM) with substrate concentration of 350 μM. The velocities of these two enzyme products did not reach a plateau within 120 min of reaction time. Hence, we used the above concentration of enzymes and data points down to 600 sec in the experiments presented hereafter.

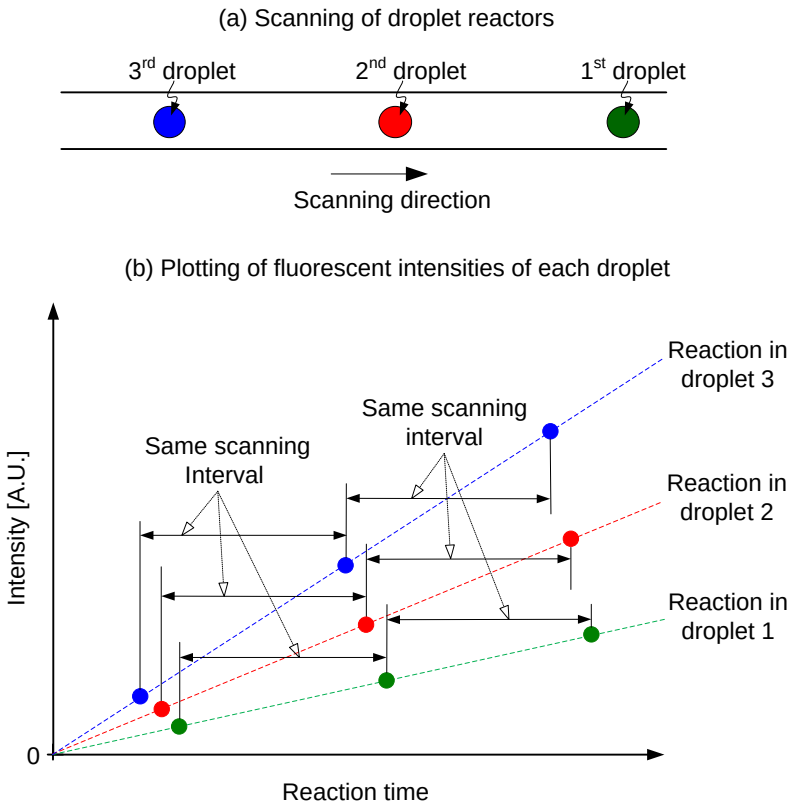

Figure D4. Schematic diagrams represent scanning and plotting of fluorescence intensities of each droplet.

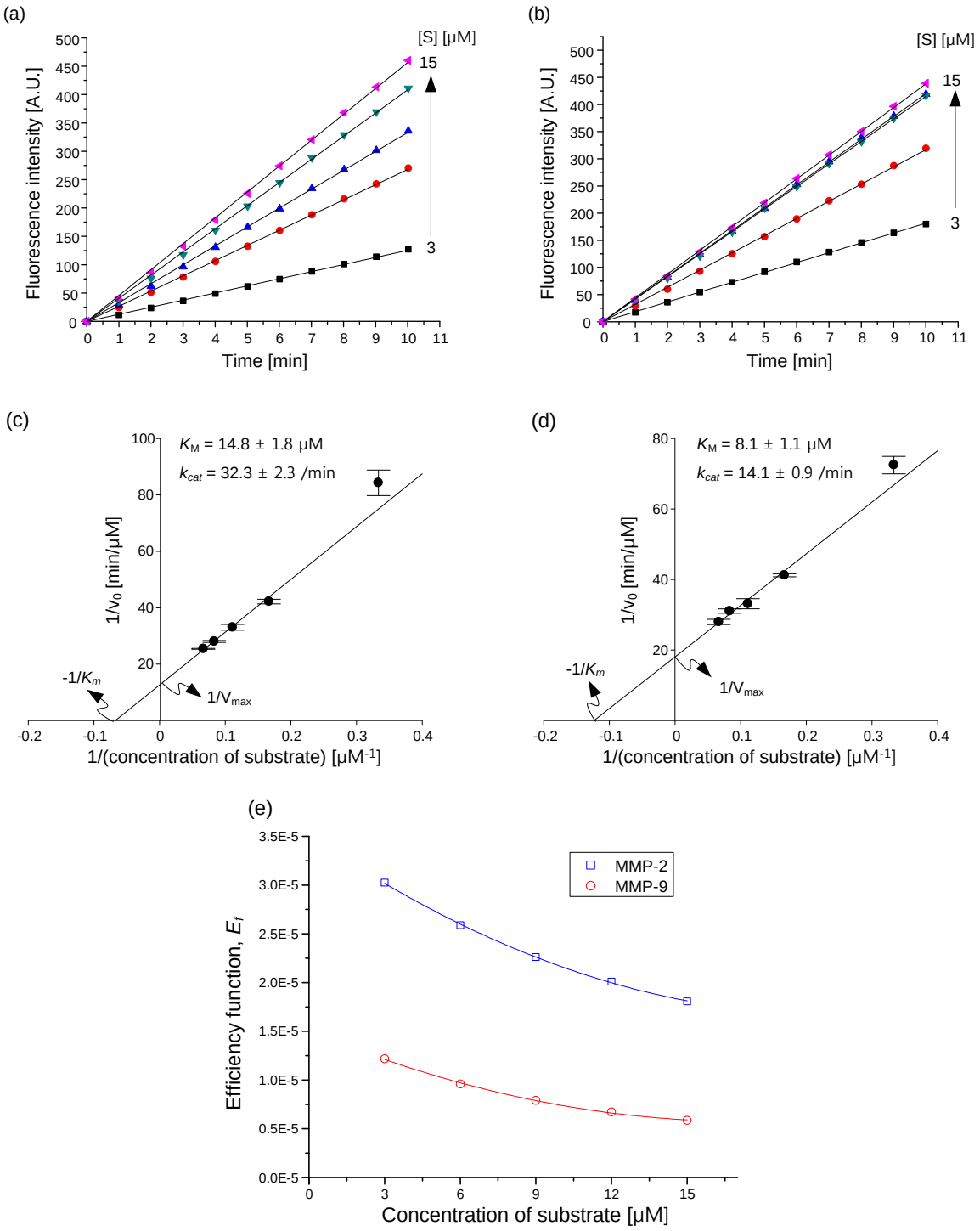

Figure D5. Determination of kinetic parameters using conventional, off-chip, methods, (a)The time scans of the MMP-2 and 9 enzymatic reactions with increasing substrate

concentration, (b) Linewaever-Burk kinetic plots, (c) Comparison of the efficiency function, E_f , of MMP-2 and MMP-9.

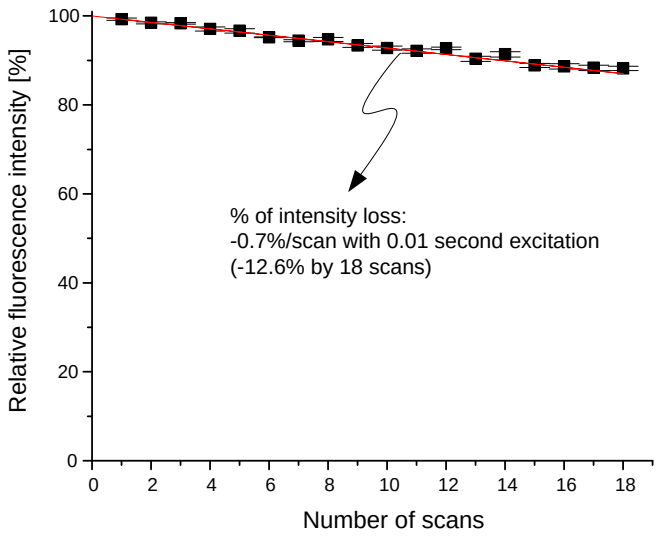

Figure D6. Effect of multiple scans on the photobleaching rate of FAM. About 0.7% of the fluorescent intensity of FAM was decreased with 0.01 s excitation at 490 nm.